NORTHWESTERN UNIVERSITY

Nonequilibrium Many-Body Physics with Photons in Circuit-QED Lattices

A DISSERTATION

SUBMITTED TO THE GRADUATE SCHOOL

IN PARTIAL FULFILLMENT OF THE REQUIREMENTS

for the degree

DOCTOR OF PHILOSOPHY

Field of Physics

By

Andy Cheong Yiu Li

EVANSTON, ILLINOIS

December 2016

ABSTRACT

Nonequilibrium Many-Body Physics with Photons in Circuit-QED Lattices

Andy Cheong Yiu Li

Lattice models of fermions, bosons, and spins have long served to elucidate the essential physics of quantum phase transitions in a variety of systems. Generalizing such models to incorporate driving and dissipation has opened new vistas to investigate nonequilibrium phenomena and dissipative phase transitions in interacting many-body systems. Circuit-QED lattices serve as an ideal platform to study the nonequilibrium many-body physics of microwave photons interacting with (artificial) atoms. In this thesis, I present three major research achievements. First, I introduce a perturbative approach including a resummation technique suitable for describing nonequilibrium states of interacting photons in circuit-QED devices. Second, I describe scanning defect microscopy which we developed in collaboration with Andrew Houck's group at Princeton. This technique allows a novel scanning-probe imaging of photon states in a circuit-QED lattice. Third, I present a theoretical analysis of the first observation of a dissipative phase transition in a circuit-QED chain.

Acknowledgements

This thesis would not be possible without the support and assistance of many people. I would like to first thank my advisor Jens Koch. He gave me the freedom to explore this wonderful world of quantum physics and provided the crucial guidance to keep me on track. He tolerated all of my crazy ideas and assisted me to dig out the useful parts from those ideas with his great patience. It is my honor to have him to be my advisor.

I would like to thank Francesco Petruccione, who helped me through the study of the abstract world of nonequilibrium physics. I am always amazed by his exceptional intuition and understanding of this complicated field. I would like to also express my gratitude to Andrew Houck, who assisted me to explore a much wider horizon. Most remarkably, he took the greatest risk in allowing me to step into his lab, while fully acknowledged what could go wrong with a theorist in a lab full of equipment.

Thank you also to Devin Underwood and Mattias Fitzpatrick, who taught me how to do experiments. (Unfortunately, I was a really bad student. Their efforts were never successful even with the best lectures and demonstrations.) With the assistance from Mattias, I could proudly announce the biggest achievement during my graduate study – my successful "operation" of a dilution fridge.

I want to thank Joshua Dempster, Guanyu Zhu, and Peter Groszkowski, who shared the office space with me. Their enthusiasm is the fuel for me to go forward during my

years in Northwestern. Together with all of my friends in TECH, they made my office (and the hallway outside) a really enjoyable place.

Most importantly, I thank my family for their encouragement and love. It would be impossible to go through this long journey without the endless support from my parents and other family members. I must thank Clare who has accompanied and supported me during these years. She taught me how to be a better scientist and a better man as well.

Table of Contents

List of Tables

List of Figures

CHAPTER 1

Introduction

Lattice models describe particles or spins residing on a set of sites, arranged in a regular fashion. Different types of interactions between particles or spins are possible and can be included in the formulation of the model. For this reason, lattice models can cover a large arena of physical systems and phenomena. Prominent examples are the fermionic Hubbard model [1–3], the Bose-Hubbard model [4, 5], and the Heisenberg model [6, 7].

Open quantum lattices extend the lattice-model concept. They include the effects of an environment and external driving fields coupled to the lattice. Such open lattices generally describe nonequilibrium phenomena and are of great interest in many subfields of physics – ranging from condensed matter [8–10] and AMO physics [11–17] to applications in quantum information [18–23]. Recently, many studies studying open quantum lattices have advanced our understanding of many-body systems under nonequilibrium conditions [14, 17, 24, 25]. Examples of phenomena predicted to emerge include nonequilibrium critical behavior [8, 11, 24–38], topological phases [15, 16, 39] and quantum chaos [17, 40]. Open quantum lattices, especially with engineered coupling to baths, also play an increasingly vital role in the development of quantum information technology such as quantum computing hardware [18–20, 23] and quantum networks [22].

The study of open quantum lattices, however, tends to be challenging. Analytical and numerical techniques for open lattices are still less developed than their counterparts for closed lattices. While for a large class of open quantum lattices the Lindblad master

equation provides an appropriate theoretical framework [41, 42], numerical methods for solving this master equation directly, such as exact diagonalization [43, 44], time evolution, or averaging of quantum trajectories [45], are computationally demanding and become quickly infeasible as lattice size or number of excitations increases. More sophisticated numerical techniques have been suggested and are further being developed, including matrix-product [46, 47], self-consistent projection operator [48] and variational [49, 50] methods . These methods can handle larger lattices to some degree, but come with their own specific drawbacks.

Photonic systems represent a particular interesting open-system complement to the well-established paradigm of ultracold-atom physics. Since photons do not possess a chemical potential[1], realistic photonic lattices typically include coherent driving and photon loss [52]. Such systems will thus be a particular useful tool to better understand, gain intuition, and ultimately devise tractable effective models for open quantum lattices of interest. Experiments with interacting photon lattices will shed light on both dynamical and steady-state phenomena by employing well-defined artificial lattice structures and systematically controlling parameters including drive strength, photon frequency, and strength of the mediated photon-photon interaction [53, 54]. Recent experiments with circuit-QED lattices [25, 55] have demonstrated the promising potential of exploring new phenomena in nonequilibrium many-body physics.

The structure of the present thesis is as follows. In chapter 2, I will review the basic building blocks of circuit-QED lattices. In chapter 3, I will discuss the effects of coupling between a circuit-QED system and an environment, and review the Lindblad

[1]However, see Ref. [51] for a proposal to engineer a chemical potential.

master equation suitable for describing the open quantum systems relevant to circuit-QED experiments. In chapters 4 to 6, I present the main results from my research. In chapter 4, I introduce a general perturbative approach including a resummation scheme suitable for open quantum lattices. Chapter 5 is devoted to scanning defect microscopy which allows imaging of photon states in a circuit-QED lattice. In chapter 6, I analyze the first observation of a dissipative phase transition in a circuit-QED chain using a quasi-classical mean-field approach.

CHAPTER 2

Circuit QED

Circuit quantum electrodynamics (circuit QED) is the field of studying systems built out of superconducting circuits with atom-light interaction. Many of its theoretical concepts are borrowed from cavity QED which studies atom-light interaction using atoms or ions inside optical cavities. Here, instead of using physical atoms, specifically designed superconducting circuits are employed to mimic atomic behavior. These artificial atoms allow the observation of many familiar phenomena in the context of circuit QED, e.g. vacuum Rabi oscillations [56, 57] and vacuum Rabi spiting [58]. Taking advantage of the highly sophisticated and advanced fabrication process for integrated circuits, artificial atoms can be made in parameter regimes which cannot be easily achieved with cavity QED. This opens up new possibilities, for example, to study ultra-strong coupling [59].

In this chapter, I will briefly review a few common circuit elements and their corresponding theoretical models. The purpose here is to provide necessary background for the remaining parts of the thesis. Interested readers may find a more comprehensive introduction to circuit QED in the thesis of D. Schuster [60] and the book chapter by S. M. Girvin [61].

2.1. Circuit quantization

To investigate quantum aspects of a superconducting circuit, we follow the conventional quantization strategy. We first have to determine the classical Lagrangian $\mathcal{L}(\phi_j, \dot{\phi}_j)$ in

terms of generalized coordinates ϕ_j and their time derivatives $\dot{\phi}_j$. For a circuit, it is convenient to choose the generalized coordinates to be fluxes ϕ_j at each node j, see fig. 2.1 for a simple example. The flux $\phi_j = \int_{t_0}^{t} \mathrm{d}t' V_j(t')$ is defined to be the time integral of the voltage V_j (relative to ground) at the node j. Voltages and fluxes play a role analogous to velocities and displacements in a mechanical system. Details on node variables and the general recipe for determining the Lagrangian of a circuit can be found in ref. [62].

Once the classical Lagrangian $\mathcal{L}$ is obtained, one acquires the conjugate momenta $q_j = \frac{\partial \mathcal{L}}{\partial \dot{\phi}_j}$. Next, the classical Hamiltonian is determined by the Legendre transformation, $\mathcal{H}(\phi_j, q_j) = \sum_j \dot{\phi}_j q_j - \mathcal{L}$. Ultimately, quantization is implemented by employing the generalized coordinate and momentum operators $\mathsf{\Phi}_j$ and q_j obeying the canonical commutation relation, $[\mathsf{\Phi}_j, \mathsf{q}_k] = i\delta_{jk}$. (I will distinguish operators from c-numbers by using sans-serif lettering.) In the following, I will briefly discuss the quantization of two types of circuit-QED oscillators – the LC oscillator and the modes of a transmission-line resonator.

2.2. LC oscillator

One of the simplest circuit elements is the LC oscillator shown in fig. 2.1. It has only one node and its classical Lagrangian is given by

$$\mathcal{L} = \frac{C}{2}\dot{\phi}^2 - \frac{1}{2L}\phi^2. \tag{2.1}$$

This is the Lagrangian of a simple harmonic oscillator with the kinetic energy $\frac{C}{2}\dot{\phi}^2$ and potential energy $\frac{1}{2L}\phi^2$. Here, the capacitance C and inverse inductance L^{-1} play the role

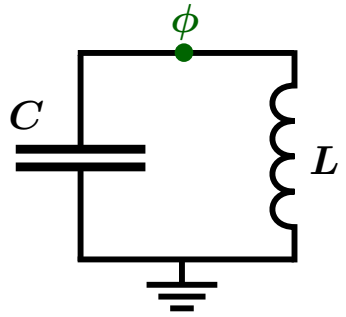

Figure 2.1. **Circuit diagram of a LC oscillator**. A capacitor with capacitance C is connected to an inductor with inductance L. The circuit is grounded at one end. For this simple circuit, there is only one degree of freedom – the node flux ϕ at the other end.

of the "mass" and "spring constant". The conjugate momentum is given by

$$q = \frac{\partial \mathcal{L}}{\partial \dot{\phi}} = C\dot{\phi}, \tag{2.2}$$

which is the charge on the capacitor.

Using a Legendre transformation, we obtain the classical Hamiltonian,

$$\mathcal{H} = \frac{1}{2C}q^2 + \frac{1}{2L}\phi^2, \tag{2.3}$$

and then quantize by replacing ϕ and q by the flux operator $\mathsf{\Phi}$ and the charge operator q. As usual, we employ bosonic annihilation and creation operators

$$\mathsf{a} = \frac{1}{\sqrt{2Z_0}}\left(\mathsf{\Phi} + iZ_0\mathsf{q}\right) \quad \text{and} \quad \mathsf{a}^\dagger = \frac{1}{\sqrt{2Z_0}}\left(\mathsf{\Phi} - iZ_0\mathsf{q}\right), \tag{2.4}$$

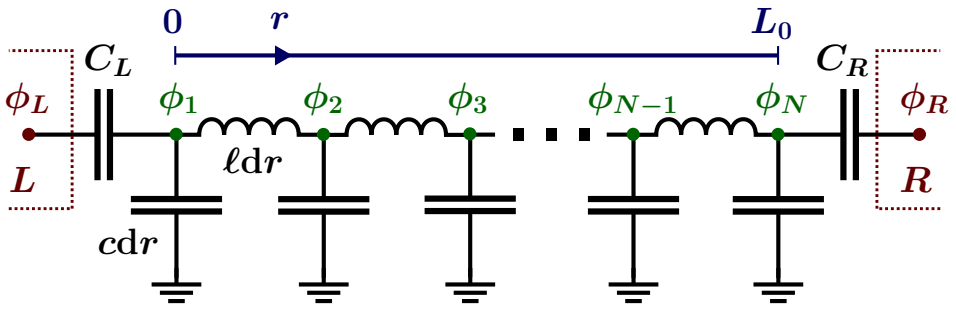

Figure 2.2. **Circuit diagram of a transmission-line resonator**. A transmission-line resonator (length L_0, capacitance per unit length c, and inductance per unit length ℓ) can be discretized into a chain of coupled LC oscillators, each with capacitance $c\,\mathrm{d}r$ and inductance $\ell\,\mathrm{d}r$. The coordinate r represents the position along the resonator and $\mathrm{d}r$ is an infinitesimal length along this coordinate. The transmission-line resonator is coupled to the degree of freedom ϕ_L (ϕ_R) of the circuit to the left (right) through a capacitor with a capacitance C_L (C_R.)

where a and $\mathsf{a}^\dagger$ satisfy the canonical commutation relation $[\mathsf{a}, \mathsf{a}^\dagger] = 1$, and $Z_0 = \sqrt{L/C}$. This gives us the standard Hamiltonian of a simple harmonic oscillator,

$$\mathsf{H} = \omega \left(\mathsf{a}^\dagger \mathsf{a} + \frac{1}{2} \right), \tag{2.5}$$

with the oscillator frequency $\omega = 1/\sqrt{LC}$.

2.3. Transmission-line resonator

I next review the topic of transmission-line resonators, mainly following the discussion in ref. [63]. A transmission-line resonator with capacitance c per unit length and inductance ℓ per unit length can be modeled as the continuum limit of coupled LC oscillators, see fig. 2.2. Here, I consider a general case in which the transmission-line resonator is capacitively coupled at the two ends to circuits L and R with coupling capacitances C_L and C_R, respectively.

2.3.1. Lagrangian

The full system Lagrangian is given by

(2.6)
$$\mathcal{L} = \mathcal{L}'_L + \mathcal{L}'_R + \frac{C_L}{2}\left(\dot{\phi}_1 - \dot{\phi}_L\right)^2 + \frac{C_R}{2}\left(\dot{\phi}_N - \dot{\phi}_R\right)^2 + \frac{c\,\mathrm{d}r}{2}\sum_{j=1}^{N}\dot{\phi}_j^2 - \frac{1}{2\ell\mathrm{d}r}\sum_{j=2}^{N}\left(\phi_j - \phi_{j-1}\right)^2,$$

where $\mathcal{L}'_L$ and $\mathcal{L}'_R$ are the Lagrangians of the circuits L and R. We divide the full system Lagrangian into four parts,

$$\mathcal{L} = \mathcal{L}_L + \mathcal{L}_R + \mathcal{L}_{\mathrm{int}} + \mathcal{L}_{\mathrm{tl}}, \tag{2.7}$$

where $\mathcal{L}_L = \mathcal{L}'_L + \frac{C_L}{2}\dot{\phi}_L^2$ and $\mathcal{L}_R = \mathcal{L}'_R + \frac{C_R}{2}\dot{\phi}_R^2$ describe the circuits on the left and right of the resonator, including an additional capacitive correction due to the coupling. The coupling between the transmission-line resonator and the circuits L and R is described by the term $\mathcal{L}_{\mathrm{int}} = -C_L\dot{\phi}_L\dot{\phi}_1 - C_R\dot{\phi}_N\dot{\phi}_R$. The last and most important term is the transmission-line-resonator Lagrangian $\mathcal{L}_{\mathrm{tl}}$,

$$\mathcal{L}_{\mathrm{tl}} = \frac{C_L}{2}\dot{\phi}_1^2 + \frac{C_R}{2}\dot{\phi}_N^2 + \frac{c\mathrm{d}r}{2}\sum_{j=1}^{N}\dot{\phi}_j^2 - \frac{1}{2\ell\mathrm{d}r}\sum_{j=2}^{N}\left(\phi_j - \phi_{j-1}\right)^2. \tag{2.8}$$

In the continuum limit, i.e. $N \to \infty$, $\mathrm{d}r \to 0$, $N\mathrm{d}r = L_0$, and $\phi_j(t) \to \phi(r,t)$, the sums turn into integrals,

$$\mathcal{L}_{\mathrm{tl}} = \frac{C_L}{2}\dot{\phi}^2(0,t) + \frac{C_R}{2}\dot{\phi}^2(L_0,t) + \frac{c}{2}\int_0^{L_0}\mathrm{d}r\dot{\phi}^2(r,t) - \frac{1}{2\ell}\int_0^{L_0}\mathrm{d}r\left(\frac{\partial\phi(r,t)}{\partial r}\right)^2. \tag{2.9}$$

To facilitate the quantization, we next express this Lagrangian in terms of the eigenmodes of the resonator.

2.3.2. Eigenmodes

We determine the eigenmodes by employing the Euler-Lagrange equation which here yields the wave equation

$$\frac{\partial^2 \phi\,(r,t)}{\partial r^2} = \ell\, c\, \frac{\partial^2 \phi\,(r,t)}{\partial t^2}, \tag{2.10}$$

with the boundary conditions

$$\frac{\partial \phi\,(r,t)}{\partial r}\Big|_{r=0} = \ell\, C_L \frac{\partial^2 \phi\,(r,t)}{\partial t^2}\Big|_{r=0} \quad \text{and} \quad -\frac{\partial \phi\,(r,t)}{\partial r}\Big|_{r=L_0} = \ell\, C_R \frac{\partial^2 \phi\,(r,t)}{\partial t^2}\Big|_{r=L_0}. \tag{2.11}$$

The eigenmodes must have the usual form,

$$\phi_\mu\,(r,t) = \varphi_\mu(r) e^{-i\omega_\mu t}, \tag{2.12}$$

where $\varphi_\mu(r)$ is the mode function and ω_μ the corresponding mode frequency. Plugging this into eqs. (2.10) and (2.11), one obtains the second-order differential equation

$$\frac{\mathrm{d}^2 \varphi_\mu(r)}{\mathrm{d}r^2} = -\ell\, c\, \omega_\mu^2 \varphi_\mu(r), \tag{2.13}$$

subject to the homogeneous boundary conditions

$$-\frac{\mathrm{d}\varphi_\mu(r)}{\mathrm{d}r}\Big|_{r=0} = \ell\, C_L \omega_\mu^2 \varphi_\mu(0) \quad \text{and} \quad \frac{\mathrm{d}\varphi_\mu(r)}{\mathrm{d}r}\Big|_{r=L_0} = \ell\, C_R \omega_\mu^2 \varphi_\mu(L_0). \tag{2.14}$$

Here, the orthonormality condition is given by

$$C_L \varphi_\mu(0)\varphi_\nu(0) + C_R \varphi_\mu(L_0)\varphi_\nu(L_0) + c\int_0^{L_0} \mathrm{d}r\, \varphi_\mu(r)\varphi_\nu(r) = \delta_{\mu\nu}. \tag{2.15}$$

Equations (2.13) to (2.15) fully define the mode functions $\varphi_\mu(r)$ and mode frequencies ω_μ. In particular, one can show that the mode frequencies ω_μ are the roots of the equation

$$\tan\left(\omega_\mu\sqrt{\ell c}\,L_0\right) = -\frac{\omega_\mu\sqrt{\ell/c}\,(C_L+C_R)}{1-\omega_\mu\sqrt{\ell/c}\,C_LC_R/(cL_0)}. \tag{2.16}$$

In the weak-coupling limit, i.e. $\frac{C_L}{cL_0} \ll 1$ and $\frac{C_R}{cL_0} \ll 1$, the mode frequencies are approximately given by $\omega_\mu = \frac{\mu\pi}{\sqrt{\ell c}L_0} = \mu\omega_1$, where $\mu = 1, 2, 3, \cdots$. (Here, $\mu = 1$ corresponds to the fundamental mode.)

We can now define new degrees of freedom $\zeta_\mu(t)$ using the mode functions $\varphi_\mu(r)$,

$$\phi\,(r,t) = \sum_\mu \zeta_\mu\,(t)\,\varphi_\mu(r), \tag{2.17}$$

Using eqs. (2.13) to (2.15) and (2.17), the resonator Lagrangian can be rewritten as

$$\mathcal{L}_{\text{tl}} = \frac{1}{2}\sum_\mu \left(\dot{\zeta_\mu}^{\,2} - \omega_\mu^2\zeta_\mu^2\right). \tag{2.18}$$

Similarly, the coupling term can be expressed as

$$\mathcal{L}_{\text{int}} = -C_L\dot{\phi}_L\sum_\mu \dot{\zeta}_\mu\varphi_\mu(0) - C_R\dot{\phi}_N\sum_\mu \dot{\zeta}_\mu\varphi_\mu(L_0). \tag{2.19}$$

2.3.3. Quantization

The resonator Lagrangian $\mathcal{L}_{\text{tl}}$ simply describes decoupled harmonic oscillators. Each harmonic oscillator can be quantized in the exactly same way as for the LC oscillator, see

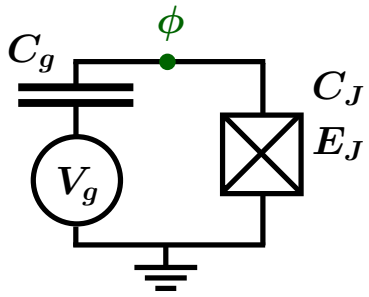

Figure 2.3. **Circuit diagram of a Cooper-pair box**. A Josephson junction with Josephson energy E_J and capacitance C_J is grounded at one end. At the other end, it is coupled to a gate voltage V_g through a capacitor with capacitance C_g. This circuit has one degree of freedom ϕ.

section 2.2. The Hamiltonian of the transmission-line resonator is thus given by

$$\mathsf{H}_{\mathrm{tl}} = \sum_{\mu} \omega_{\mu} \left(\mathsf{a}_{\mu}^{\dagger} \mathsf{a}_{\mu} + \frac{1}{2} \right), \tag{2.20}$$

where a_{μ} is the annihilation operator of the eigenmode μ with mode frequency ω_{μ}.

2.4. Superconducting qubits

The photons in resonators are non-interacting. To introduce nonlinearity, which is necessary for interesting many-body physics, one can couple the resonators to artificial atoms/qubits. There are several qubit designs used in circuit QED, including charge qubits [64, 65], flux qubits [66, 67], phase qubits [68], transmon qubits [69, 70] and fluxonium qubits [71, 72]. In this section, I will briefly discuss the charge qubit (Cooper-pair-box), and then the transmon qubit which is one of the most commonly used qubit designs today.

2.4.1. Cooper-pair-box Hamiltonian

The circuit diagram of a Cooper-pair box is shown in fig. 2.3. It is similar to that of the LC oscillator (fig. 2.1) except that the inductor is replaced by a Josephson junction

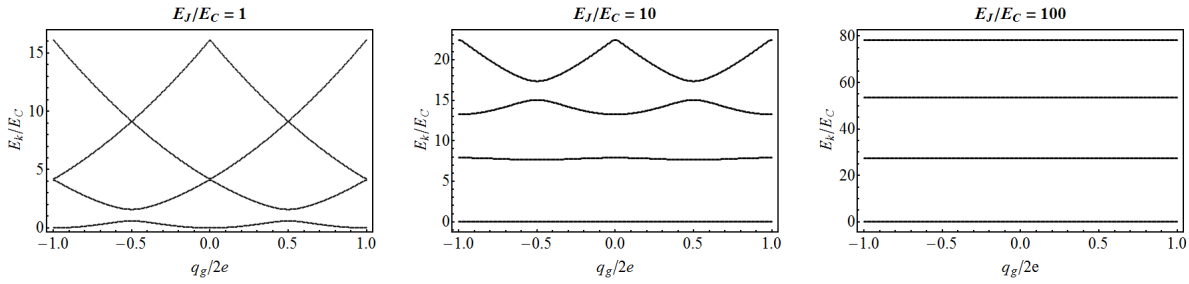

Figure 2.4. **Eigenenergies of the Cooper-pair box**. The lowest four eigenenergies E_k of the Cooper-pair box are shown. The eigenenergies become less sensitive to the offset charge q_g with increasing E_J/E_C. (The eigenenergies are offset by the ground state energy at $q_g = 0$ for each E_J/E_C.)

with capacitance C_J and Josephson energy E_J, and there is an additional gate voltage V_g capacitively coupled to the circuit. As shown in ref. [69], its Hamiltonian can be written as

$$\mathsf{H} = 4E_C \left(\frac{\mathsf{q}}{2e} - \frac{q_g}{2e} \right)^2 - E_J \cos\left(\frac{2e}{\hbar} \phi \right). \tag{2.21}$$

Here, $E_C = \frac{e^2}{2C}$ is the charging energy, $C = C_g + C_J$ is the effective capacitance and ϕ (q) is the flux (charge) operator as in the LC oscillator case. The offset charge $q_g = C_g V_g + Q_r$ is controlled by the gate voltage V_g, where Q_r represents the environment-induced offset charge. Note that the Hamiltonian is often written in terms of the phase operator $\varphi = \frac{2e}{\hbar}$ and it conjugate operator $\mathsf{n} = \frac{\mathsf{q}}{-2e}$ (number operator) in the literature.

2.4.2. Transmon qubit

The transmon Hamiltonian is identical to that of the Cooper-pair box [69]. The key difference between the transmon qubit and Cooper-pair box is the ratio E_J/E_C. The transmon qubit operates in the large E_J/E_C limit[1]. In this regime, the eigenenergies

[1]This corresponds to shunting the Josephson junction by a capacitor with a large capacitance, which leads to small E_C.

become insensitive to the offset charge q_g with increasing E_J/E_C as shown in fig. 2.4. Hence, the transmon qubit is protected from charge noise and thus has dramatically improved dephasing times compared to the Cooper-pair box.

2.4.3. Qubit approximation

In the large E_J/E_C limit, the eigenenergies E_k ($k = 0, 1, 2, \cdots$) are approximately [69]

$$E_k \approx \sqrt{8E_C E_J}\left(k + \frac{1}{2}\right) - \frac{E_C}{12}\left(6k^2 + 6k + 3\right) - E_J. \tag{2.22}$$

Hence, the energy difference ω_{10} between the ground and first excited states is approximately given by

$$\omega_{10} = E_1 - E_0 \approx \sqrt{8E_C E_J} - E_C. \tag{2.23}$$

For the first and second excited states, the energy difference is

$$\omega_{21} = E_2 - E_1 \approx \sqrt{8E_C E_J} - 2E_C. \tag{2.24}$$

The difference between ω_{21} and ω_{10} displays the nonlinearity of the transmon qubit. This nonlinearity protects the second excited state (and higher transmon levels) from being occupied. Hence, the transmon qubit can be described by the effective two-level Hamiltonian,

$$\mathsf{H}_{\text{eff}} = \frac{\Omega}{2}\sigma^z, \tag{2.25}$$

where $\Omega = \omega_{10}$ is the energy difference between the first two levels. As a result, the transmon circuit can be used as a superconducting qubit.

2.4.4. Tuning the transmon frequency

It is desirable that qubit frequencies are tunable. For the transmon qubit, the insensitivity to offset charge makes it impractical to tune the qubit frequency by adjusting the gate voltage V_g. The usual way to make a transmon qubit tunable is to replace the Josephson junction by a SQUID loop (fig. 2.5). One can show that the SQUID loop is equivalent to a single junction with an effective Josephson energy E_J^* that depends on the external magnetic flux ϕ_{ext} through the SQUID loop [69],

$$E_J^* = (E_{J1} + E_{J2}) \cos\left(\frac{\pi\phi_{\text{ext}}}{\Phi_0}\right) \sqrt{1 + d^2 \tan^2\left(\frac{\pi\phi_{\text{ext}}}{\Phi_0}\right)}. \tag{2.26}$$

Here, $\Phi_0 = \frac{h}{2e}$ is the magnetic flux quantum and $d = \frac{E_{J1} - E_{J2}}{E_{J1} + E_{J2}}$ the relative asymmetry of Josephson energies between the two junctions. Hence, the qubit frequency of the transmon qubit can be controlled by an external magnetic flux through the SQUID loop, and the accessible frequency range is determined by the asymmetry d.

2.5. Circuit-QED lattices

A circuit-QED lattice forms by coupling[2] circuit elements, including LC oscillators, transmission-line resonators and superconducting qubits, and arranging them into a particular lattice geometry. These lattices are one of the most direct ways to access

[2]The coupling is capacitive for the cases to be discussed later on in this thesis. Other types of coupling have also been proposed, e.g. coupling through Josephson junctions [34] to allow nonlinear coupling between circuit elements.

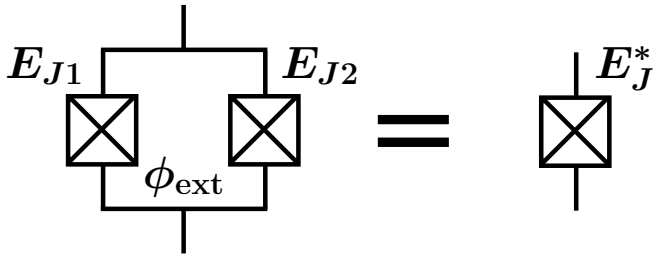

Figure 2.5. **The SQUID loop makes the Josephson energy tunable**. The SQUID loop is equivalent to a single Josephson junction. The effective Josephson energy E_J^* is tunable by the external magnetic flux ϕ_{ext}. The tunable range depends on the asymmetry between E_{J1} and E_{J2}.

many-body physics using circuit-QED systems. In this section, I will review two simple lattice models – a resonator array and the Jaynes-Cummings lattice.

2.5.1. Resonator array

A resonator array consists of coupled LC oscillators or transmission-line resonators. An experimental realization of 49 coupled transmission-line resonators is shown in fig. 2.6. The resonators are capacitively coupled at each end to the nearest-neighbor resonators. Generalizing the result in section 2.3, the general form of the Hamiltonian for a resonator array is

$$\mathsf{H} = \sum_{j=1}^{N} \sum_{\mu_j} \omega_{\mu_j;j}\ \mathsf{a}^\dagger_{\mu_j;j}\ \mathsf{a}_{\mu_j;j} + \sum_{\langle j,k\rangle} \sum_{\mu_j,\nu_k} t_{\mu_j\nu_k;jk} \left(\mathsf{a}^\dagger_{\mu_j;j}\mathsf{a}_{\nu_k;k} + \mathsf{a}_{\mu_j;j}\mathsf{a}^\dagger_{\nu_k;k}\right), \tag{2.27}$$

where $\mathsf{a}_{\mu_j;j}$ ($\mathsf{a}^\dagger_{\mu_j;j}$) is the photon annihilation (creation) operator of resonator mode μ_j at site j, and N is the total number of site. The second term in this equation represents photon hopping between the nearest-neighbor sties $\langle j,k\rangle$. The hopping rate $t_{\mu_j\nu_k;jk}$ is determined by the coupling capacitance and the mode functions φ_{μ_j} and φ_{ν_k}. (Note that

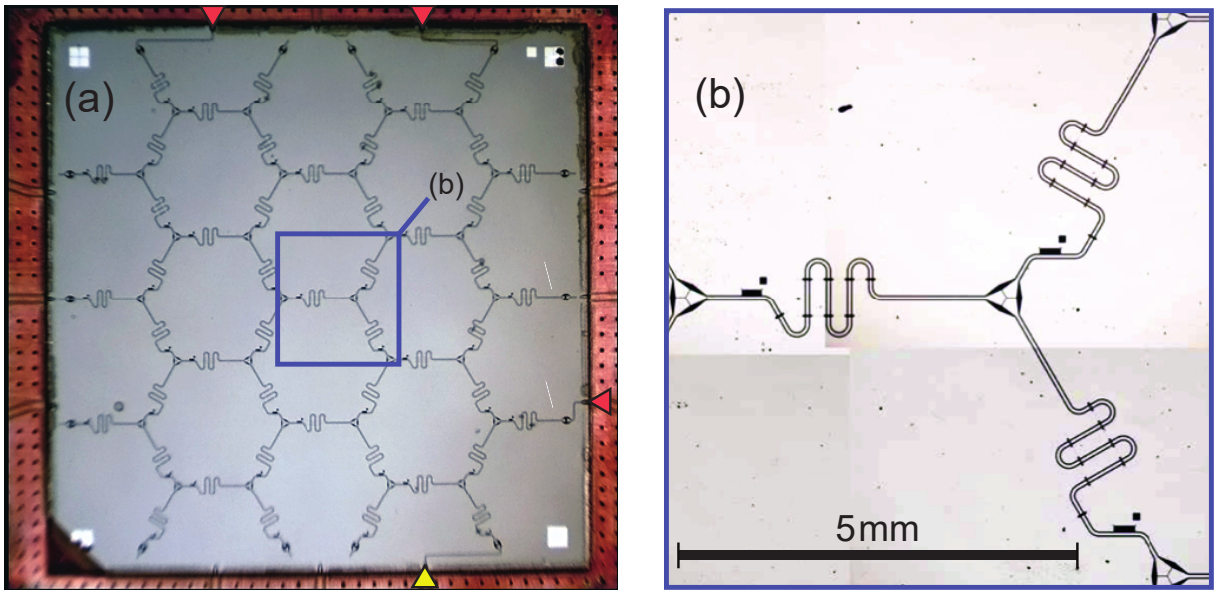

Figure 2.6. **Coupled transmission-line resonators**. This resonator array is the experimental device to be discussed in chapter 5. (a) Forty nine resonators are fabricated to form a Kagome lattice. (b) Resonators are coupled by three-way capacitors. One section of each resonator meanders to save space on the chip. (This figure is identical to fig. 5.2.)

the rotating wave approximation has been applied to drop the counter-rotating terms $\mathsf{a}^\dagger_{\mu_j;j}\mathsf{a}^\dagger_{\nu_k;k}$ and $\mathsf{a}_{\mu_j;j}\mathsf{a}_{\nu_k;k}$.)

The multi-mode Hamiltonian can be simplified if the resonators at different sites are nearly identical. In this case, the photon hopping between different modes, e.g. between the fundamental mode and first harmonic, is suppressed by a large frequency difference. Those hopping terms, i.e. $\mathsf{a}^\dagger_{\mu_j;j}\mathsf{a}_{\nu_k;k} + \text{h.c.}$ for $\mu_j \neq \nu_k$, can thus be dropped by using the rotating wave approximation. Now, if only one of the modes is excited by an external drive, we can use the effective single-mode Hamiltonian,

$$\mathsf{H} = \sum_{j=1}^{N} \omega_j \, \mathsf{a}_j^\dagger \mathsf{a}_j + \sum_{\langle j,k \rangle} t_{jk} \left(\mathsf{a}_j^\dagger \mathsf{a}_k + \mathsf{a}_j \mathsf{a}_k^\dagger \right). \tag{2.28}$$

Moreover, if resonators are identical, one obtains the standard tight-binding Hamiltonian for bosons,

$$\mathsf{H} = \omega \sum_{j=1}^{N} \mathsf{a}_j^\dagger \mathsf{a}_j + t \sum_{\langle j,k \rangle} \left(\mathsf{a}_j^\dagger \mathsf{a}_k + \mathsf{a}_j \mathsf{a}_k^\dagger \right). \tag{2.29}$$

2.5.2. Jaynes-Cummings lattice

To induce photon-photon interaction to a resonator array, one can capacitively couple a superconducting qubit (e.g. a transmon qubit) to each resonator. The on-site Hamiltonian corresponds to the Jaynes-Cummings model [73],

$$\mathsf{h}_j = \omega\, \mathsf{a}_j^\dagger \mathsf{a}_j + \frac{\Omega}{2} \sigma_j^z + g \left(\mathsf{a}_j \sigma_j^+ + \mathsf{a}_j^\dagger \sigma_j^- \right), \tag{2.30}$$

where σ_j^+ (σ_j^-) is the pseudo-spin raising (lowering) operator and g is the coupling strength between the qubit and resonator[3]. Together with photon hopping between nearest-neighbor sites, the full Hamiltonian for the Jaynes-Cummings lattice is given by

$$\mathsf{H} = \sum_j \mathsf{h}_j + t \sum_{\langle j,k \rangle} \left(\mathsf{a}_j^\dagger \mathsf{a}_k + \mathsf{a}_j \mathsf{a}_k^\dagger \right). \tag{2.31}$$

The Jaynes-Cummings lattice model is of great interest in the study of many-body physics. For instance, the superfluid-Mott-insulator phase transition [4] is encountered in the study of the Jaynes-Cummings lattice under thermal equilibrium conditions [74, 75].

[3] If the coupling strength g is large, i.e. the circuit is in the ultra-strong coupling regime, or the qubit is far detuned from the resonator, i.e. $\left| \frac{\Omega - \omega}{\Omega + \omega} \right|$ is not a small parameter, one also has to consider the counter-rotating term, $\mathsf{a}_j \sigma_j^- + \mathsf{a}_j^\dagger \sigma_j^+$.

2.6. Decoherence

The previous discussion applies to the case that the system is isolated from the environment. For a realistic device, the system is always intentionally and unintentionally coupled to the environment. First of all, a superconducting circuit can only be controlled/driven by coupling to other devices. This inevitably allows excitations to leak out of the circuit (decay). These control channels can also introduce noise to the circuit, e.g. a tunable transmon qubit is subject to the noise of the external magnetic flux, which leads to dephasing. Last but not least, there may be intrinsic decay/dephasing channels which depend on the particular design and fabrication process. Interested readers may find a more detailed discussion of possible decay and dephasing mechanisms in D. Schuster's thesis [60, ch. 4] and L. Bishop's thesis [76, sec. 3.6.1].

The knowledge of the microscopic decoherence mechanism is usually unnecessary if the circuit is only weakly coupled to the environment. In most cases relevant to circuit-QED experiments, it is sufficient to assume three effective decoherence channels: photon decay, qubit relaxation and qubit pure dephasing. Photon decay and qubit relaxation occur spontaneously when an excitation leaks from the circuit into the environment. Qubit pure dephasing describes the situation in which a qubit loses its quantum coherence in the absence of qubit relaxation. In the next chapter, I will discuss the Lindblad master equation which takes these decoherence channels into account.

CHAPTER 3

Lindblad master equation

An appropriate strategy to handle the coupling between a system and an environment plays an important role in the study of open quantum systems. One may directly consider the full Hamiltonian H describing both the system $\mathcal{S}$ and environment $\mathcal{E}$, which can be written as

$$\mathsf{H} = \mathsf{H}_{\mathcal{S}} + \mathsf{H}_{\mathcal{E}} + \mathsf{H}_{\mathcal{SE}}. \tag{3.1}$$

Here, $\mathsf{H}_{\mathcal{S}}$, $\mathsf{H}_{\mathcal{E}}$ and $\mathsf{H}_{\mathcal{SE}}$ are the system, environment and system-environment interaction Hamiltonians. Except in relatively simple cases, e.g. the spin-boson model [77], the direct study of the full Hamiltonian H is unpractical for two reasons: (i) the microscopic understanding of the environment is rather limited for most physical systems, and (ii) even if a physical model for the environment is available, it is usually extremely hard to solve the full Hamiltonian due to the huge number of environmental degrees of freedom. A pragmatic strategy is to trace out the environmental degrees of freedom. Under certain conditions, this allows us to focus on the system time evolution governed by the Lindblad master equation [41, ch. 3]. In this chapter, I will review the master-equation formalism, the properties of master equation and some simple applications.

3.1. Markovian dynamics

3.1.1. Density matrix

We begin this section with a quick review of the density matrix ρ, which is a convenient means to describe the state of an open system. A density matrix is a hermitian operator which has the general expression

$$\rho = \sum_j p_j \left|\psi_j\right\rangle \left\langle\psi_j\right| . \tag{3.2}$$

Here, $\{|\psi_j\rangle\}_j$ is a set of orthonormal quantum states. We can interpret ρ as the statistical mixture of the quantum states $|\psi_j\rangle$ with individual probabilities p_j. (A pure state $|\psi\rangle$ is represented by $\rho = |\psi\rangle\langle\psi|$.) This probabilistic interpretation requires the probabilities p_j to be non-negative and their sum to be one. As a result, the density matrix ρ is positive-semidefinite. Along the lines of the probabilistic interpretation, the expectation value of any operator A is given by

$$\langle \mathsf{A} \rangle = \sum_j p_j \left\langle\psi_j\right| \mathsf{A} \left|\psi_j\right\rangle = \mathrm{Tr}\left[\mathsf{A}\rho\right] . \tag{3.3}$$

3.1.2. Lindblad master equation

For a closed system described by the Hamiltonian H, the time evolution of the density matrix $\rho(t)$ is governed by the von Neumann equation,

$$\frac{\mathrm{d}\rho(t)}{\mathrm{d}t} = -i\left[\mathsf{H}, \rho(t)\right] , \tag{3.4}$$

which can be deduced from the definition (3.2) and the Schröedinger equation. As previously explained, the direct treatment based on the full Hamiltonian H is often unpractical. Instead, we consider the reduced density matrix $\rho_{\mathcal{S}}$ defined by

$$\rho_{\mathcal{S}}(t) = \mathrm{Tr}_{\mathcal{E}}\rho(t), \tag{3.5}$$

where the partial trace $\mathrm{Tr}_{\mathcal{E}}$ traces out the environmental degrees of freedom. Its generic time evolution is governed by

$$\frac{\mathrm{d}\rho_{\mathcal{S}}(t)}{\mathrm{d}t} = -i\mathrm{Tr}_{\mathcal{E}}\left[\mathsf{H}, \rho(t)\right]. \tag{3.6}$$

This equation is suboptimal due to the explicit dependence on the full density matrix $\rho(t)$ instead of simply the system density matrix $\rho_{\mathcal{S}}(t)$. Several approximation schemes with different underlying empirical models of the environment have been considered [41, sec. 3.3].

One widely adopted approximation scheme applicable to weak system-environment coupling is briefly outlined here [41, sec. 3.3.1]. The scheme begins with the assumption that the system $\mathcal{S}$ and environment $\mathcal{E}$ are weakly coupled and initially disentangled. This allows a perturbative treatment of the system-environment interaction using Born approximation and gives a time evolution equation which is nonlocal in time. We then employ a crucial assumption (Markov approximation) – the correlation times of excitations in the environment is small compared to the characteristic time scales of the system. As a result, the system approximately undergoes Markovian dynamics, i.e. the time evolution is completely determined by the system state at the current time. Another way to express this is to say that there is no "memory effect", see fig. 3.1 for the schematic of a Markovian

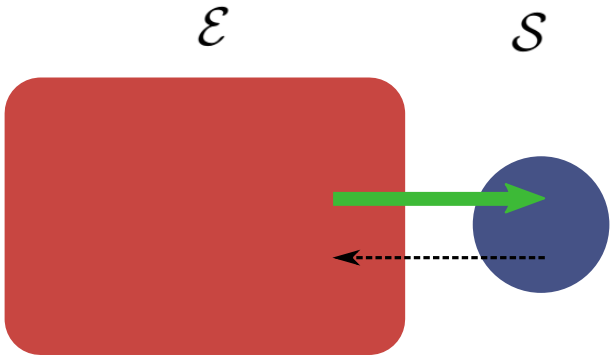

Figure 3.1. **Schematic of a Markovian open quantum system**. The system $\mathcal{S}$ is weakly coupled to the environment $\mathcal{E}$. This coupling in general leads to leakage (black dashed arrow) of excitations/information from the system to the environment. The change of the environment is eliminated (one-way green arrow) in the environmental correlation time scale. Hence. the environment has no "memory" of the system state in the past. This lack of "memory effect" renders the system Markovian.

open quantum system. One then obtains the Lindblad master equation in the general form

$$\frac{\mathrm{d}\rho_{\mathcal{S}}(t)}{\mathrm{d}t} = -i\left[\mathsf{H}'_{\mathcal{S}}, \rho_{\mathcal{S}}(t)\right] + \sum_j \gamma_j \mathbb{D}\left[\mathsf{A}_j\right]\rho_{\mathcal{S}}(t), \tag{3.7}$$

with the dissipator $\mathbb{D}\left[\mathsf{A}_j\right]\rho_{\mathcal{S}} = \mathsf{A}_j\rho_{\mathcal{S}}\mathsf{A}_j^\dagger - \frac{1}{2}\mathsf{A}_j^\dagger\mathsf{A}_j\rho_{\mathcal{S}} - \frac{1}{2}\rho_{\mathcal{S}}\mathsf{A}_j^\dagger\mathsf{A}_j$, jump operators A_j, corresponding rates γ_j, and Lamb-shifted system Hamiltonian $\mathsf{H}'_{\mathcal{S}}$. For convenience, we rewrite the master equation in short form using the Liouville superoperator (or Liouvillian) $\mathbb{L}$

$$\frac{\mathrm{d}\rho_{\mathcal{S}}(t)}{\mathrm{d}t} = \mathbb{L}\rho_{\mathcal{S}}(t). \tag{3.8}$$

The term "superoperator" designates an object mapping an ordinary Hilbert-space operator such as $\rho_{\mathcal{S}}$ to another Hilbert-space operator. (In my notation, I distinguish superoperators, operators, and real/complex numbers by using double-stroke, sans-serif, and regular lettering, respectively.)

The Lindblad master equation has a simple physical interpretation. If the system is not coupled to the environment, the system undergoes unitary time evolution governed by the von Neumann equation, $\frac{\mathrm{d}\rho_{\mathcal{S}}}{\mathrm{d}t} = -i\,[\mathsf{H}_{\mathcal{S}}, \rho_{\mathcal{S}}]$. With the system-environment coupling on, this unitary time evolution is slightly modified leading to the Lamb-shifted system Hamiltonian $\mathsf{H}'_{\mathcal{S}}$. The unitary time evolution is not the full story yet. The environment in general induces non-unitary effects such as dissipation and dephasing. The deviation from the unitary von-Neumann equation results in the second term with each jump operator A_j representing a particular non-unitary effect. We will discuss more concrete examples of jump operators in sections 3.4 and 3.5. From now on, we drop the subscript $\mathcal{S}$ and the prime symbol of the system Hamiltonian (unless otherwise stated).

3.1.3. Quantum dynamics semigroup

The derivation of the Lindblad master equation discussed above is based on a microscopic model of the environment. One may consider a different approach based merely on the properties of the system dynamics without considering any microscopic model. The system time evolution can be represented by a map $\mathbb{U}_t$ which propagates the system state from t_0 to $t_0 + t$, i.e. $\rho(t_0 + t) = \mathbb{U}_t\rho(t_0)$ for any propagation time $t > 0$. The map $\mathbb{U}_t$ is a member of the quantum dynamics semigroup [42, sec. 1.2.4] if it satisfies the following conditions.

(i) $\mathbb{U}_t$ is trace-preserving meaning that $\mathrm{Tr}\,[\mathbb{U}_t\mathsf{X}] = \mathrm{Tr}\,[\mathsf{X}]$ for an arbitrary Hilbert-space operator X. This is necessary for the time evolution to be physical since the trace of a density matrix is always one.

(ii) $\mathbb{U}_t$ is a completely positive map. A positive map requires that a positive-semidefinite operator always maps to a positive-semidefinite operator, which is consistent with

that fact that a density matrix must be positive semidefinite. Complete positivity is a stronger condition imposing on the outer product of the map and an identity. Its precise definition can be found in ref. [42, sec. 1.2.2].

(iii) $\mathbb{U}_t\rho(t_0)$ is continuous for all $t > 0$.

(iv) $\mathbb{U}_t\mathbb{U}_{t'} = \mathbb{U}_{t+t'}$ for all $t, t' > 0$. This essentially means that the time evolution at time t depends only on the system state at time t. Hence, this is called the Markov property.

These criteria are rather general requirement for the time evolution of a physical system. More importantly, if the time evolution satisfies these criteria, the Lindblad master equation is the most general form governing the system dynamics[1]. This further motivates the usage of the Lindblad master equation.

3.2. Eigenvalues and eigenstates of the Liouville superoperator

The time evolution of an open system is completely determined by the Liouville superoperator $\mathbb{L}$ as shown in eq. (3.8). In other words, $\mathbb{L}$ is the generator of the quantum dynamical semigroup, i.e. $\mathbb{U}_t = e^{\mathbb{L}t}$. Here, we will explore the master equation through the eigenvalues and eigenstates of the Liouville superoperator $\mathbb{L}$,

$$\mathbb{L}\mathsf{u}_\mu = \lambda_\mu \mathsf{u}_\mu. \tag{3.9}$$

While it is tempting to think of eq. (3.9) as a superoperator-analogue of the stationary Schrödinger equation, it is important to note that the Liouville superoperator $\mathbb{L}$ is in general non-Hermitian, i.e. $\mathbb{L}^\dagger$ is not equal to $\mathbb{L}$. Hence, its eigenvalues may be complex-valued

[1]This is proven for the case of finite-dimensional Hilbert space, see refs. [78, 79] for two independent proofs. For unbounded Hilbert space, all known examples are also in the general form (3.7) even though the formal proof is not known.

and we have to distinguish right eigenstates u_μ from left eigenstates $\breve{\mathsf{u}}_\mu$, given by

$$\breve{\mathsf{u}}_\mu^\dagger \mathbb{L} = \breve{\mathsf{u}}_\mu^\dagger \lambda_\mu. \tag{3.10}$$

As long as we keep this in mind, however, it is useful to mimic bra-ket notation and allow ourselves the freedom to write operators and their adjoints also in the alternative form

$$\mathsf{u}_\mu \leftrightarrow |\mathsf{u}_\mu) \quad \text{and} \quad \breve{\mathsf{u}}_\mu^\dagger \leftrightarrow (\breve{\mathsf{u}}_\mu| \,. \tag{3.11}$$

We can then denote the Hilbert-Schmidt inner product [80] between operators as $(\mathsf{x}|\mathsf{y}) \equiv \mathrm{Tr}[\mathsf{x}^\dagger \mathsf{y}]$. Linear algebra dictates that the right and left eigenstates of $\mathbb{L}$ are bi-orthogonal and, by appropriate normalization, can be chosen to be bi-orthonormal,

$$(\breve{\mathsf{u}}_\nu|\, \mathsf{u}_\mu) = \delta_{\mu\nu}. \tag{3.12}$$

The eigenspectrum of a valid Liouville superoperator $\mathbb{L}$ has the following two properties. First of all, the real part of any eigenvalue λ_μ must be non-positive. This is necessary for the density matrix $\rho(t)$ to remain positive-semidefinite in the long time limit. Moreover, there is a right eigenstate u_0 with trace one, i.e. $\mathrm{Tr}[\mathsf{u}_0] = (\mathbb{1}|\mathsf{u}_0) = 1$, associated with the eigenvalue λ_0. This is the immediate consequence of the trace of the density matrix being a conserved quantity. One can also show that the corresponding left eigenstate is the identity operator, $(\breve{\mathsf{u}}_0| = \mathsf{1}$, and the corresponding eigenvalue λ_0 always equals zero. We will further discuss in the next section that this eigenstate u_0 turns out to be the steady state if there exists a unique steady state.

It is useful to represent an operator or superoperator using the eigenstates of $\mathbb{L}$. We first assume that the eigenstates of $\mathbb{L}$ form a complete set[2] or equivalently the Liouville superoperator $\mathbb{L}$ can be diagonalized. Hence, we can represent an arbitrary operator X as

$$|\mathsf{X}) = \sum_{\mu} |\mathsf{u}_\mu)\,(\breve{\mathsf{u}}_\mu|\,\mathsf{X}) = \sum_{\mu} (\mathsf{X})_\mu\ |\mathsf{u}_\mu)\,, \tag{3.13}$$

and an arbitrary superoperator $\mathbb{A}$ as

$$\mathbb{A} = \sum_{\mu,\nu} |\mathsf{u}_\mu)(\breve{\mathsf{u}}_\mu|\mathbb{A}|\mathsf{u}_\nu)(\breve{\mathsf{u}}_\nu| = \sum_{\mu,\nu} (\mathbb{A})_{\mu\nu}\,|\mathsf{u}_\mu)(\breve{\mathsf{u}}_\nu|. \tag{3.14}$$

In particular, the Liouville superoperator $\mathbb{L}$ is represented by a diagonal matrix,

$$\mathbb{L} = \sum_{\mu} \lambda_\mu |\mathsf{u}_\mu)(\breve{\mathsf{u}}_\mu|. \tag{3.15}$$

Except for the matter of left vs. right eigenvectors, these expressions are familiar from the usual decomposition of states and operators in Hilbert space. Analogous to solving the Schrödinger equation using the eigenvalues and eigenstates of the Hamiltonian, the formal solution of the Lindblad master equation is given by

$$|\rho_0) = \sum_{\mu} |\mathsf{u}_\mu)\,(\breve{\mathsf{u}}_\mu|\ \rho_0) \implies |\rho(t)) = \sum_{\mu} e^{\lambda_\mu t}\,|\mathsf{u}_\mu)\,(\breve{\mathsf{u}}_\mu|\ \rho_0)\,. \tag{3.16}$$

where $|\rho_0)$ is the initial state at $t = 0$. This immediately provides us with insight into the physical meaning of the eigenvalues of $\mathbb{L}$. The imaginary part of an eigenvalue governs the oscillatory behavior of the time evolution. It thus plays a role similar to the eigenenergy of a closed system. The real part governs the amplitude of its corresponding eigenstate. (The

[2]The Liouville superoperator $\mathbb{L}$ is non-Hermitian, so that completeness of the set of eigenstates is not guaranteed, though heuristically very common for $\mathbb{L}$.

amplitude must either decrease or remain the same since $\mathrm{Re}\,\lambda_\mu \leq 0$ for all eigenvalues λ_μ of $\mathbb{L}$.) Hence, it is closely related to the dissipation of the system.

For completeness, we now briefly discuss the case in which the eigenstates of $\mathbb{L}$ do not form a complete set, i.e. the Liouville superoperator $\mathbb{L}$ is not diagonalizable. There, $\mathbb{L}$ can still be decomposed through a similarity transformation into a specific block diagonal matrix, namely the Jordan normal form $\mathbb{J}$ [81, sec. 5.3],

$$\mathbb{L} = \mathbb{S}^{-1}\mathbb{J}\mathbb{S}. \tag{3.17}$$

This similarity transformation specifies a bi-orthonormal basis – the columns of $\mathbb{S}^{-1}$ and rows of $\mathbb{S}$ play a role analogous to the eigenstates $|\mathsf{u}_\mu)$ and $(\breve{\mathsf{u}}_\mu|$, respectively. (Many of them are indeed identical, e.g. those eigenstates associated with non-degenerate eigenvalues.) Arbitrary operators and superoperators can thus be represented in a way similar to eqs. (3.13) and (3.14). The formal solution of the Lindblad master equation is slightly modified since the chosen basis is not entirely formed by the eigenstates of $\mathbb{L}$. As we are not going to utilize this basis in this thesis, we will leave the discussion here without go into any detail.

3.3. Nonequilibrium steady state

The (nonequilibrium) steady state is recently of great interest for the study of many topics in condensed-matter physics and quantum information. A few examples include dissipative phase transitions [25, 28, 29, 34, 82] and dissipation engineering for state preparation [83].

A system coupled to an environment evolves toward its steady state ρ_s in the long-time limit, i.e.

$$\lim_{t\to\infty} \rho(t) = \rho_s. \tag{3.18}$$

For example, the steady state of an undriven system coupled to a thermal bath is the thermal equilibrium state. In general, the steady state of an open system can differ from the equilibrium state due to, for example, external drive, coupling to multiple baths, etc. Note that the presence of an external drive, in general, results in a time-dependent Liouville superoperator $\mathbb{L}(t)$. The definition (3.18) of the steady state is thus not directly applicable. However, for many models relevant to circuit-QED experiments, one can reduce the time-dependent models into time-independent Liouville superoperators by a transformation to a rotating frame. Examples with single-frequency cosine-periodic drive will be discussed in sections 3.4 and 3.5.

A steady state ρ_s is unique if and only if the system long-time limit is independent of the initial state. (In other words, all information of the initial state is washed out in the long-time limit.) Assuming that a unique steady state ρ_s exists, we deduce from the time evolution equation (3.16) that ρ_s is indeed the eigenstate u_0 associated with the eigenvalue $\lambda_0 = 0$. This means that ρ_s is characterized by the time invariance property,

$$\frac{\mathrm{d}\rho_s}{\mathrm{d}t} = \mathbb{L}\rho_s = \mathbb{L}\mathsf{u}_0 = 0. \tag{3.19}$$

One can also deduce from eq. (3.16) that a unique steady state exists if and only if all except one eigenvalues of $\mathbb{L}$ have negative real part, i.e.

(3.20) u_0 is the unique steady state if and only if $\mathrm{Re}\,[\lambda_\mu] < 0$ for all $\mu \neq 0$.

Note that the eigenvalues $\lambda_{\mu\neq 0}$ give the timescales of transient dynamics. In particular, λ_{ADR} is the eigenvalue of $\mathbb{L}$ with its real part closest to zero. The negative real part of λ_{ADR}, namely the asymptotic decay rate or $\mathrm{ADR} = -\mathrm{Re}\,\lambda_{\mathrm{ADR}}$ [29], determines the longest time scale for the system to relax to the unique steady state. The ADR plays a crucial role in the study of dissipative phase transitions, which will be further discussed in chapter 6.

The reader may have the impression that a unique steady state is rare since its existence poses a global constraint [eq. (3.20)] on the full spectrum of $\mathbb{L}$. However, Davies [84] has shown that a moderate condition satisfied by many driven-dissipative systems is sufficient for the existence of a unique steady state. Roughly speaking, a unique steady state is guaranteed for a finite-dimensional system if the jump operators A_j and Hamiltonian H "connect" the full Hilbert space[3]. One example satisfying this condition is a driven N-level system, $\mathsf{H} = \epsilon\,\mathsf{S}_x$, with the only jump operator being the lowering operator S_-. Note that the aforementioned theorem does not apply to any infinite-dimensional process. This might seem to make the theorem rather limited in studying circuit-QED models since a resonator is already associated with an infinite-dimensional Hilbert space. However, in almost all cases, the resonator Hilbert space can be safely truncated to finite number of excitations and thus the time evolution is once again a finite-dimensional process. (There

[3] "Connect" here means that any state $|\psi\rangle$ is linked to the full Hilbert space by H and A_j. In other words, there is no proper subspace $\mathcal{K}$ of the Hilbert space $\mathcal{H}$ such that for any state $|\psi\rangle$ in $\mathcal{K}$, $\mathsf{A}_j\ |\psi\rangle$ and $(H - \frac{i}{2}\sum_j A_j^\dagger A_j)\,|\psi\rangle$ remains in $\mathcal{K}$. A more precise condition is given by Davies [84, Thm. 13].

are other known sufficient conditions for the existence of a unique steady state, e.g. Spohn [85] has shown a condition regarding the number of jump operators A_j.)

3.4. Driven-damped harmonic oscillator

In this section, we review a simple example of the Lindblad master equation, describing a driven-damped harmonic oscillator. This is a good model of the single-mode microwave resonator (sections 2.2 and 2.3) driven by an AC tone. We will find the analytic solution by employing the third-quantization method [86–88]. This analytic solution facilitates the analysis of more complicated circuit-QED lattices, for example the perturbative study of Jaynes-Cummings lattices (section 4.5).

A harmonic oscillator of frequency ω is modeled by the oscillator Hamiltonian,

$$\mathsf{H}_o = \omega \mathsf{a}^\dagger \mathsf{a}. \tag{3.21}$$

We consider the simplest possible external drive, which is a sinusoidal continuous-wave drive with frequency ω_d and amplitude ϵ. This gives the time-dependent drive Hamiltonian

$$\mathsf{H}_d(t) = 2\epsilon \cos(\omega_d t)\left(\mathsf{a}^\dagger + \mathsf{a}\right). \tag{3.22}$$

The fact that the oscillator is damped results in loss of excitations. For superconducting circuits, the excitations are microwave photons and hence we call this decoherence channel photon decay in this context. Photon decay is modeled by the dissipator $\gamma\,\mathbb{D}[\mathsf{a}]$, where the annihilation operator a serves as the jump operator and γ is the photon decay rate.

We then write the Lindblad master equation (3.7) as

$$\frac{\mathrm{d}\rho(t)}{\mathrm{d}t} = \mathbb{L}(t)\rho(t) = -i\left[\mathsf{H}_o + \mathsf{H}_d(t), \rho(t)\right] + \gamma\,\mathbb{D}\left[\mathsf{a}\right]\rho(t). \tag{3.23}$$

This Liouville superoperator is time-dependent. To arrive at a time-independent one, we consider a transformation into the frame co-rotating with the drive, i.e.

$$\begin{cases} \mathsf{H}(t) & \rightarrow & \mathsf{H}'(t) = e^{i\omega_d \mathsf{a}^\dagger \mathsf{a} t}\mathsf{H}(t)e^{-i\omega_d \mathsf{a}^\dagger \mathsf{a} t} - \frac{\mathrm{d}}{\mathrm{d}t}\left(\omega_d \mathsf{a}^\dagger \mathsf{a} t\right), \\ \rho(t) & \rightarrow & \rho'(t) = e^{i\omega_d \mathsf{a}^\dagger \mathsf{a} t}\rho(t)e^{-i\omega_d \mathsf{a}^\dagger \mathsf{a} t}, \\ \mathbb{D}\left[\mathsf{a}\right] & \rightarrow & \mathbb{D}\left[e^{i\omega_d \mathsf{a}^\dagger \mathsf{a} t}\mathsf{a}e^{-i\omega_d \mathsf{a}^\dagger \mathsf{a} t}\right] = \mathbb{D}\left[\mathsf{a}\right]. \end{cases} \tag{3.24}$$

One can show that the Lindblad master equation is covariant under this transformation, i.e.

$$\frac{\mathrm{d}\rho'(t)}{\mathrm{d}t} = \mathbb{L}'(t)\rho'(t) = -i\left[\mathsf{H}'(t), \rho'(t)\right] + \gamma\mathbb{D}\left[\mathsf{a}\right]\rho'(t), \tag{3.25}$$

with the Hamiltonian in the rotating frame,

$$\mathsf{H}'(t) = \delta\omega \mathsf{a}^\dagger \mathsf{a} + \epsilon\left(\mathsf{a}^\dagger + \mathsf{a}\right) + \epsilon\left(\mathsf{a}^\dagger e^{2i\omega_d t} + \mathsf{a}e^{-2i\omega_d t}\right), \tag{3.26}$$

and the detuning $\delta\omega = \omega - \omega_d$. Assuming that the drive amplitude ϵ is much smaller than the drive frequency ω_d, i.e. $\epsilon \ll \omega_d \sim \omega$, it is justified to drop the time-dependent term in H' using the rotating wave approximation. From now on, we will work with the time-independent Liouville superoperator in the rotating frame and drop the prime symbol, i.e.

$$\frac{\mathrm{d}\rho(t)}{\mathrm{d}t} = \mathbb{L}\rho(t) = -i\left[\delta\omega \mathsf{a}^\dagger \mathsf{a} + \epsilon\left(\mathsf{a}^\dagger + \mathsf{a}\right), \rho(t)\right] + \gamma\,\mathbb{D}\left[\mathsf{a}\right]\rho(t). \tag{3.27}$$

This Liouville superoperator is bilinear, i.e. each term involves at most two annihilation and/or creation operators. In this case, the exact solution to the stationary Lindblad equation (3.9) can be obtained by using the third-quantization method for the boson operator space [87]. We introduce the superoperators $\mathbb{b}$, $\mathbb{b}^\ddagger$, β, $\beta^\ddagger$, which mimic boson annihilation and creation operators, by

$$\mathbb{b}\rho = \mathsf{a}\rho \quad \text{and} \quad \mathbb{b}^\ddagger\rho = \mathsf{a}^\dagger\rho - \rho\mathsf{a}^\dagger, \tag{3.28}$$

$$\beta\rho = \rho\mathsf{a}^\dagger \quad \text{and} \quad \beta^\ddagger\rho = \rho\mathsf{a} - \mathsf{a}\rho. \tag{3.29}$$

While $\mathbb{b}^\ddagger$ and $\mathbb{b}$ are not proper adjoints, the use of the unconventional "‡" symbol is motivated by the resulted commutation relations of the ordinary form,

$$[\mathbb{b}, \mathbb{b}^\ddagger] = [\beta, \beta^\ddagger] = 1, \tag{3.30}$$

and all other commutators vanish. Thanks to this commutator algebra, $\mathbb{L}$ takes on the compact form [87],

$$\mathbb{L} = \theta\mathbb{b}^\ddagger\mathbb{b} + \theta^*\beta^\ddagger\beta - i\epsilon\left(\mathbb{b}^\ddagger - \beta^\ddagger\right). \tag{3.31}$$

Here, $\mathbb{b}$ ($\mathbb{b}^\ddagger$) and β ($\beta^\ddagger$) may be viewed as "normal-mode" superoperators associated with complex-valued "mode frequencies" $\theta = -i\,\delta\omega - \gamma/2$. To make the Liouville superoperator even simpler, we apply a coherent displacement

$$\mathsf{a} \to \mathsf{D}^\dagger\mathsf{a}\mathsf{D} = \mathsf{a} + \alpha \;\text{ and }\; \mathsf{a}^\dagger \to \mathsf{D}^\dagger\mathsf{a}^\dagger\mathsf{D} = \mathsf{a}^\dagger + \alpha^*, \tag{3.32}$$

where $\mathsf{D} = \exp(\alpha \mathsf{a}^\dagger - \alpha^* \mathsf{a})$ is the displacement operator and α the displacement amplitude. In the superoperator language, this corresponds to the following transformation,

$$\mathbb{b} \to \mathbb{b} + \alpha \quad \text{and} \quad \mathbb{b}^\ddagger \to \mathbb{b}^\ddagger, \tag{3.33}$$

$$\beta\!\!\!^{-} \to \beta\!\!\!^{-} + \alpha^* \quad \text{and} \quad \beta\!\!\!^{-\ddagger} \to \beta\!\!\!^{-\ddagger}. \tag{3.34}$$

By choosing $\alpha = i\epsilon/\theta$, $\mathbb{L}$ takes on the simple diagonal form

$$\mathbb{L} = \theta \mathbb{b}^\ddagger \mathbb{b} + \theta^* \beta\!\!\!^{-\ddagger} \beta\!\!\!^{-}. \tag{3.35}$$

From this, it is straightforward to read off eigenvalues and eigenstates of $\mathbb{L}$, analogous to the way we find eigenvalues and eigenstates of a harmonic-oscillator Hamiltonian. The right and left "vacuum states" obey $\mathbb{b} \left|\mathsf{r}_{00}\right) = \beta\!\!\!^{-} \left|\mathsf{r}_{00}\right) = 0$ and $\left(\breve{\mathsf{r}}_{00}\right| \mathbb{b}^\ddagger = \left(\breve{\mathsf{r}}_{00}\right| \beta\!\!\!^{-\ddagger} = 0$. (The double indices in the subscript correspond to the two normal modes $\mathbb{b}$ and $\beta\!\!\!^{-}$.) The right "vacuum state" is therefore the projector $\left|\mathsf{r}_{00}\right) = |0\rangle\langle 0|$ onto the (displaced) zero-photon state. As discussed in section 3.2, the left "vacuum state" always coincides with the identity operator, $\left(\breve{\mathsf{r}}_{00}\right| = \mathsf{1}$. Once the coherent displacement is reversed, we thus obtain $|\alpha\rangle\langle\alpha|$ for the steady state of the Liouville superoperator $\mathbb{L}$. The "excited" eigenstates of $\mathbb{L}$ are obtained by acting with the creation superoperators on the "vacuum states." This means

$$\left|\mathsf{r}_{mn}\right) = \frac{1}{\sqrt{m!n!}} (\mathbb{b}^\ddagger)^m (\beta\!\!\!^{-\ddagger})^n \left|\mathsf{r}_{00}\right) \quad \text{and} \quad \left(\breve{\mathsf{r}}_{mn}\right| = \frac{1}{\sqrt{m!n!}} \left(\breve{\mathsf{r}}_{00}\right| (\mathbb{b})^m (\beta\!\!\!^{-})^n \,, \tag{3.36}$$

where m and n are non-negative integers. The corresponding eigenvalues are given by

$$\lambda_{mn} = m\theta + n\theta^*. \tag{3.37}$$

3.5. Driven-damped two-level system

Another important example is the driven-damped two-level system (TLS), which is a good model of many circuit-QED qubits, say the transmon qubit reviewed in section 2.4. We will first introduce the Bloch equations and then outline the exact solution. This solution provides an easily accessible path to further our conceptual understanding of relaxation and dephasing. It also forms a basis for studying more complicated systems.

A TLS with energy Ω, driven by a sinusoidal tone, is modeled by the Hamiltonian,

$$\mathsf{H}(t) = \frac{\Omega}{2}\sigma^z + 2\epsilon\cos(\omega_d t)\,\sigma^x. \tag{3.38}$$

Qubit relaxation and dephasing are modeled by two jump operators σ^- and σ^z, respectively. Similar to the harmonic oscillator case, we get a time-independent Liouville superoperator by transforming into a frame co-rotating with the drive and applying the rotating wave approximation. This gives the Lindblad master equation

$$\frac{\mathrm{d}\rho(t)}{\mathrm{d}t} = \mathbb{L}\rho(t) = -i\left[\frac{\delta\Omega}{2}\sigma^z + \epsilon\sigma^x, \rho(t)\right] + \Gamma\mathbb{D}\left[\sigma^-\right]\rho(t) + \frac{\gamma_\phi}{2}\mathbb{D}\left[\sigma^z\right]\rho(t), \tag{3.39}$$

where $\delta\Omega = \Omega - \omega_d$ is the detuning between the TLS and the drive frequencies, Γ is the TLS relaxation rate and γ_ϕ is the pure dephasing rate.

An elegant way to solve the master equation is to decompose the density matrix in terms of the identity matrix $\mathsf{1}$ and Pauli matrices $\vec{\sigma} = (\sigma^x, \sigma^y, \sigma^z)$ in the Bloch vector

form,

$$\rho(t) = \frac{1}{2}\left(1 + \langle\vec{\sigma}\rangle(t) \cdot \vec{\sigma}\right), \tag{3.40}$$

where $\langle\vec{\sigma}\rangle(t) = (\langle\sigma^x\rangle(t), \langle\sigma^y\rangle(t), \langle\sigma^z\rangle(t))$ is the expectation value of $\vec{\sigma}$ at time t. Hence, the master equation (3.39) can be expressed as

$$\frac{\mathrm{d}}{\mathrm{d}t}\begin{pmatrix} 1 \\ \langle\sigma^x\rangle(t) \\ \langle\sigma^y\rangle(t) \\ \langle\sigma^z\rangle(t) \end{pmatrix} = \begin{pmatrix} 0 & 0 & 0 & 0 \\ 0 & -\frac{\Gamma}{2} - \gamma_\phi & -\delta\Omega & 0 \\ 0 & \delta\Omega & -\frac{\Gamma}{2} - \gamma_\phi & -2\epsilon \\ -\Gamma & 0 & 2\epsilon & -\Gamma \end{pmatrix} \begin{pmatrix} 1 \\ \langle\sigma^x\rangle(t) \\ \langle\sigma^y\rangle(t) \\ \langle\sigma^z\rangle(t) \end{pmatrix}. \tag{3.41}$$

Note that the 4×4 matrix on the right-hand side is a matrix representation of $\mathbb{L}$. Diagonalizing it yields the eigenspectrum of $\mathbb{L}$. Here, we take a slightly different approach by rewriting eq. (3.41) to obtain the famous Bloch equations [89, Ch. 3],

$$\frac{\mathrm{d}}{\mathrm{d}t}\begin{pmatrix} \langle\sigma^x\rangle(t) \\ \langle\sigma^y\rangle(t) \\ \langle\sigma^z\rangle(t) \end{pmatrix} = \begin{pmatrix} -\frac{\Gamma}{2} - \gamma_\phi & -\delta\Omega & 0 \\ \delta\Omega & -\frac{\Gamma}{2} - \gamma_\phi & -2\epsilon \\ 0 & 2\epsilon & -\Gamma \end{pmatrix} \begin{pmatrix} \langle\sigma^x\rangle(t) \\ \langle\sigma^y\rangle(t) \\ \langle\sigma^z\rangle(t) \end{pmatrix} - \begin{pmatrix} 0 \\ 0 \\ \Gamma \end{pmatrix}, \tag{3.42}$$

or in more compact form:

$$\frac{\mathrm{d}\langle\vec{\sigma}\rangle}{\mathrm{d}t} = \mathbf{A}\langle\vec{\sigma}\rangle - \vec{\mathsf{b}}. \tag{3.43}$$

From the Bloch equations, one can identify the relaxation time $T_1 = \Gamma^{-1}$, dephasing time $T_2 = (\frac{\Gamma}{2} + \gamma_\phi)^{-1}$ and pure dephasing time $T_2^* = \gamma_\phi^{-1}$. The well-known inequality, $T_2 \leq 2T_1$, is also apparent.

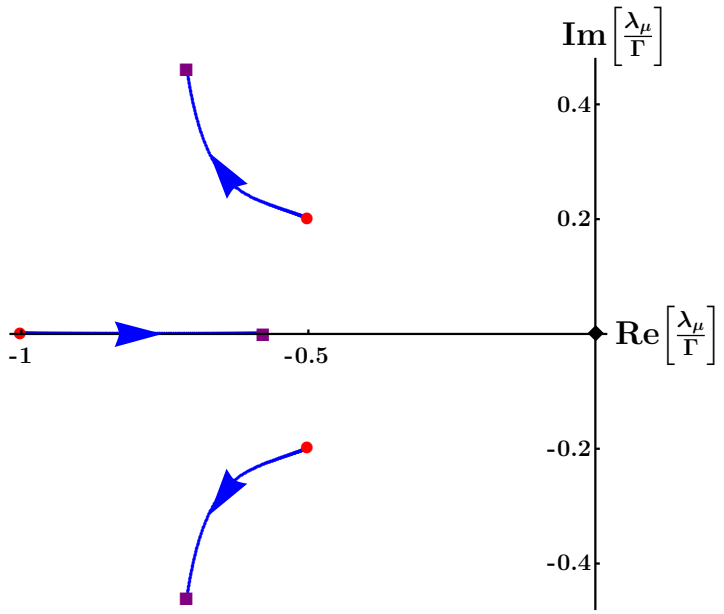

Figure 3.2. **Eigenvalue spectrum of a driven-damped TLS**. The diagram shows the eigenvalue spectrum for system parameters chosen as $\frac{\delta\Omega}{\Gamma} = 0.2$ and varying drive strength from $\frac{\epsilon}{\Gamma} = 0$ (red circles) to $\frac{\epsilon}{\Gamma} = 0.25$ (purple squares). The fourth eigenvalue (black diamond) corresponds to the steady state and is always zero. As illustrated by the blue trajectories, the flow of the eigenvalues is non-trivial and the eigenvalue(s) closest to zero switches from the complex pair to the purely real eigenvalue as ϵ increases.

We can determine the steady state from the Bloch equations by demanding $\frac{\mathrm{d}\langle\vec{\sigma}\rangle}{\mathrm{d}t} = 0$. This turns the Bloch equations into the system of linear equations, $\mathbf{A}\langle\vec{\sigma}\rangle_s = \vec{\mathsf{b}}$, and we obtain the solution

$$\rho_s = \frac{1}{2}\left[1 - \frac{2\epsilon\,\delta\Omega}{\delta\Omega^2 + \frac{1}{4}\Gamma^2 + 2\epsilon^2}\sigma^x - \frac{\epsilon\,\Gamma}{\delta\Omega^2 + \frac{1}{4}\Gamma^2 + 2\epsilon^2}\sigma^y + \frac{\delta\Omega^2 + \frac{\Gamma^2}{4}}{\delta\Omega^2 + \frac{1}{4}\Gamma^2 + 2\epsilon^2}\sigma^z\right]. \tag{3.44}$$

Other than the steady state, the remaining eigenspectrum of $\mathbb{L}$ coincides with the eigenspectrum of the matrix $\mathbf{A}$. However, the eigenvalues and eigenstates of $\mathbf{A}$ usually depend on the system parameters $\delta\Omega$, ϵ and Γ in a rather non-trivial way, see fig. 3.2. The general

analytic expressions of them are complicated except for a few special cases, e.g. for $\delta\Omega = 0$ or $\epsilon = 0$.

3.6. Numerical methods and approximations

As we have seen in the last section, the exact solution of the Lindblad master equation can be non-trivial even for a simple TLS. For many models relevant to circuit QED, we indeed have to rely on numerics and approximations to investigate their behavior. In this section, we will briefly review some of the numerical methods and approximations.

3.6.1. Numerical methods

The most straightforward numerical approach to solving the master equation is exact numerical diagonalization of $\mathbb{L}$. Once a linear basis is introduced, the Liouville superoperator $\mathbb{L}$ can be represented by a $N^2 \times N^2$ matrix, where N is the dimension of the system Hilbert space. [For example, a matrix representation of $\mathbb{L}$ for the driven-damped TLS was shown in eq. (3.41).] For relatively simple systems where N is small, e.g. coupled TLSs [90, 91] or Jaynes-Cummings lattices [30, 92, 93] with small numbers of sites, exact numerical diagonalization is possible.

Exact diagonalization, however, quickly becomes impractical when we deal with larger systems. For instance, for an open system with 16 interacting TLS, $\mathbb{L}$ is represented by a matrix of size 2^{32} by 2^{32}. This already approaches the state-of-the-art limit of exact diagonalization [94, 95]. The Hilbert space dimension N grows exponentially with system size, and the even more dramatic N^2 growth of the number of operator basis states severely limits the applicability of the exact diagonalization method. Exact diagonalization is

insufficient for the study of the collective behavior of open lattices, say dissipative phase transitions [25, 28, 29, 34]. It is also impractical for investigating nonlinear systems with more complex lattice structure, e.g. Jaynes-Cummings Kagome lattices realizable in the circuit QED architecture [52, 53]. To go beyond this limitation, alternative theoretical and numerical approaches are being developed.

One well-established numerical alternative to (partial) diagonalization of $\mathbb{L}$ are quantum trajectory methods [96, 97]. This approach converts the time evolution of the density matrix to the time evolution of quantum states with stochastic jumps (trajectories). The steady-state expectation values are then determined by the long-time limit of an ensemble of trajectories [45]. Quantum trajectories approach involves only quantum states but not density matrices, hence the number of basis states grows with the Hilbert space dimension N, not with N^2. This enables the simulation of larger systems compared to exact diagonalization. However, quantum trajectory simulation remains limited due to the exponential growth of N with system size. Another sophisticated numerical alternative consists of matrix product methods [46, 47, 98]. Matrix product methods have been successful in simulating large one-dimensional open systems [91, 99]. Applying these methods to systems of higher dimension may be possible [100] but remains difficult. Recently, variational methods [49, 50] have been introduced and show promising potential in determining the steady state of higher-dimensional systems. However, a consensus regarding the quantity to be varied has not yet been reached.

3.6.2. Approximations

Apart from these numerical methods, several approaches based on different analytical approximations have been developed. Some of these approaches utilize the concept of perturbation theory. Specialized perturbative approaches have been applied to open quantum systems in specific contexts, which include full counting statistics [101, 102], finite-time evolution [103, 104] and critical behavior [32, 33]. Another perturbative approach is the generalized Schrieffer-Wolff formalism [105–108] for systems with separable fast and slow degrees of freedom. However, the above approaches are intended to be applied to specific types of open quantum systems. They cannot be easily used for open lattices, e.g. driven-dissipative JC lattices. Hence, I have developed a general perturbative formalism describing corrections to eigenvalues and eigenstates of the Liouville superoperator $\mathbb{L}$ [109, 110] as discussed in chapter 4.

Approaches based on mean-field theory [111] are also widely utilized. The mean-field ansatz results in a set of equations which is relatively easy to solve. This allows investigation of several nonlinear open systems in which other methods are impractical [25, 28, 30, 34, 90, 112, 113]. It has been shown that the mean-field ansatz is justified for specific nonequilibrium systems coupled to a thermal bath [111, 114]. However, a general justification for the mean-field ansatz in open quantum systems remains absent to the best of my knowledge. Other than the lack of general justification, understanding the mean-field result can sometimes be difficult. For example it is widely observed that the mean-field steady-state solution can exhibit bistability [25, 28, 30, 112, 115–117]. Interpreting the observed mean-field bistability is a non-trivial task, and the interpretation indeed varies

from case to case [25, 28, 48, 117–119]. The mean-field bistability for a circuit-QED chain will be further discussed in section 6.4.2.

CHAPTER 4

Nonequilibrium perturbation theory and resummation

The dynamics and steady state of an Markovian open quantum system are determined by the eigenvalues and eigenstates of of the Liouville superoperator $\mathbb{L}$ as discussed in chapter 3. However, solving for the eigenvalues and eigenstates of $\mathbb{L}$ is theoretically challenging. Here, we present a perturbation theory (PT) in the framework of the Lindblad master equation that systematically determines the corrections to eigenstates and eigenvalues of $\mathbb{L}$. Our treatment is not limited to a certain system or system type. Rather, it is applicable to a wide range of perturbations and different open quantum systems. PT similar to the one presented here was previously studied [120, 121], but results were limited to the steady state and the issue of non-positivity of density matrices due to truncation was not addressed by the authors.

The density-matrix PT we develop yields results both for the steady state as well as for all other eigenstates of $\mathbb{L}$. Further, we propose and derive a new PT based on the amplitude matrix. This amplitude-matrix PT guarantees a properly positive steady-state density matrix. Both kinds of PT can be applied to large open systems with lattice structure. Understanding the properties of such open systems is of immense interest and would otherwise be challenging due to the system size[1]. The study of such systems is an

[1]There are a few numerical methods, e.g. matrix product methods and variational methods, suitable for large open lattices. However, each of them has its own limitation as discussed in section 3.6.

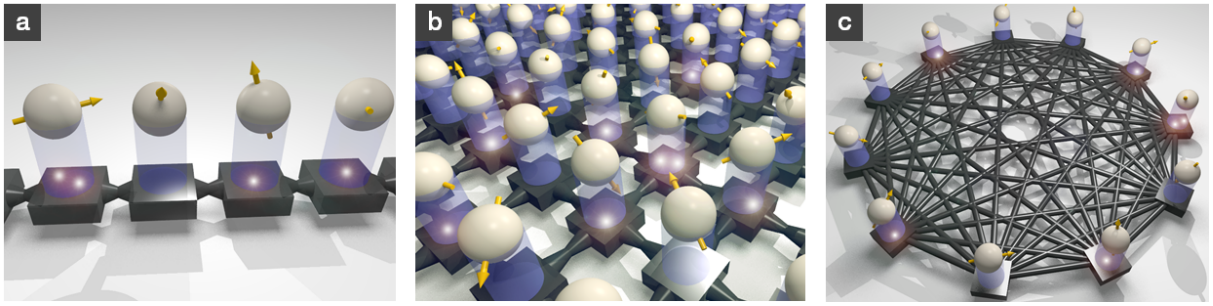

Figure 4.1. **Open quantum lattices of different dimensionalities and geometries**. The examples show Jaynes-Cummings lattices in which photons can hop between neighboring resonators (dark boxes) and experience an interaction mediated by the coupling to two-level systems (represented as spins). Lattice types of interest include (a) one-dimensional Jaynes-Cummings chains, (b) two-dimensional arrays such as the depicted square lattice, and (c) more artificial arrangements of theoretical interest, such as the global-coupling scenario where each site is connected to all other sites.

important motivation for developing the PT presented here. (The two PTs have been reported in [109].)

We then take a crucial step beyond finite-order PT by demonstrating a partial resummation of the perturbation series for the steady-state solution of the Lindblad master equation. We employ this method to study an open Jaynes-Cummings lattice [fig. 4.1] and establish that the resummation affords a significant improvement of the approximation accuracy. We illustrate the method's versatility in handling both finite-size and infinite lattices as well as different geometries and dimensionalities in a natural way. (The resummation scheme has been reported in [110].)

4.1. Density-matrix perturbation theory

We propose a non-degenerate density-matrix PT based on the eigenvalues and eigenstates of the Liouville superoperator $\mathbb{L}$. The right and left eigenstates $|\mathsf{u}_\mu)$ and $(\breve{\mathsf{u}}_\mu|$ of $\mathbb{L}$

associated with the eigenvalue $\lambda_\mu \in \mathbb{C}$ are defined by eqs. (3.9) and (3.10):

$$\mathbb{L}\,|\mathsf{u}_\mu) = \lambda_\mu\,|\mathsf{u}_\mu)\,, \qquad (\breve{\mathsf{u}}_\mu|\,\mathbb{L} = (\breve{\mathsf{u}}_\mu|\,\lambda_\mu. \tag{4.1}$$

Here, to mimic bra-ket notation, we write operators and their adjoints according to eq. (3.11):

$$\mathsf{v} \leftrightarrow |\mathsf{v}) \quad \text{and} \quad \mathsf{v}^\dagger \leftrightarrow (\mathsf{v}|\,. \tag{4.2}$$

Suitably normalized, the left and right eigenstates obey the bi-orthonormality relation

$$(\breve{\mathsf{u}}_\mu|\mathsf{u}_\nu) = \delta_{\mu\nu}, \tag{4.3}$$

where $(\mathsf{x}|\mathsf{y}) \equiv \mathrm{Tr}[\mathsf{x}^\dagger\mathsf{y}]$ is the Hilbert-Schmidt inner product. As discussed in sections 3.2 and 3.3, the eigenvalues λ_μ and the associated right eigenstates $|\mathsf{u}_\mu)$ contain all information of the steady state (labeled by $\mu = 0$) and the dynamics of the system.

In analogy to closed-system PT, the density-matrix PT is based on the series expansion of λ_μ and $|\mathsf{u}_\mu)$ with respect to a small parameter α set by the perturbation. The starting point is, thus, the separation of $\mathbb{L}$ into two parts: an unperturbed superoperator $\mathbb{L}_0$ and a perturbation $\alpha\,\mathbb{L}_1$, i.e.

$$\mathbb{L} = \mathbb{L}_0 + \alpha\,\mathbb{L}_1. \tag{4.4}$$

Like the original Liouville superoperator, $\mathbb{L}_0$ must still be a proper generator of the quantum dynamical semigroup. (The requirements for being a proper generator are discussed in section 3.1.) In addition, we are interested in determining the corrections to part of the

unperturbed spectrum $\{\lambda_\mu^{(0)}, (\breve{\mathsf{u}}_\mu^{(0)}|, |\mathsf{u}_\mu^{(0)})\}$. As appropriate for non-degenerate PT, we will assume that this part of the spectrum is solvable and non-degenerate.

We next employ a general series expansion of eigenvalues and eigenstates in α,

$$\lambda_\mu = \sum_{j=0}^{\infty} \alpha^j \lambda_\mu^{(j)}, \quad |\mathsf{u}_\mu) = \sum_{j=0}^{\infty} \alpha^j \left|\mathsf{u}_\mu^{(j)}\right) . \tag{4.5}$$

Here, the index j counts orders of perturbation theory and $\lambda_\mu^{(j)}$ and $|\mathsf{u}_\mu^{(j)})$ are hence the j-th-order corrections to the eigenvalue and the right eigenstate. We determine recursion relations for $\lambda_\mu^{(j)}$ and $|\mathsf{u}_\mu^{(j)})$ by first plugging eqs. (4.4) and (4.5) into eq. (4.1) and then examining the result order by order in α. For the j-th order in α, we obtain the general recursive expression

$$\left(\mathbb{L}_0 - \lambda_\mu^{(0)}\right) \left|\mathsf{u}_\mu^{(j)}\right) = -\mathbb{L}_1 \left|\mathsf{u}_\mu^{(j-1)}\right) + \left|\Delta_\mu^{(j)}\right) \tag{4.6}$$

with $|\Delta_\mu^{(j)}) = \sum_{k=1}^{j} \lambda_\mu^{(k)} |\mathsf{u}_\mu^{(j-k)})$.

So far, our treatment directly mirrors the well-known derivation of stationary PT for a closed system. Specifically, consider replacing $\mathbb{L}_0$, $\mathbb{L}_1$, $|\mathsf{u}_\mu)$ and λ_μ by the unperturbed Hamiltonian H_0, the perturbation V, the eigenvectors $|\psi_\mu\rangle$ and eigenenergies E_μ of $\mathsf{H} \equiv \mathsf{H}_0 + \alpha\mathsf{V}$. Then, eq. (4.6) takes exactly the form of the usual recursion equation in closed-system PT, namely

$$\left(\mathsf{H}_0 - E_\mu^{(0)}\right) \left|\psi_\mu^{(j)}\right\rangle = -\mathsf{V} \left|\psi_\mu^{(j-1)}\right\rangle + \left|\delta_\mu^{(j)}\right\rangle , \tag{4.7}$$

with $|\delta_\mu^{(j)}\rangle = \sum_{k=1}^{j} E_\mu^{(k)} |\psi_\mu^{(j-k)}\rangle$. To obtain the recursive relation for the eigenenergy correction $E_\mu^{(j)}$, we multiply eq. (4.7) with $\langle\psi_\mu^{(0)}|$ from the left. This yields

$$E_\mu^{(j)} = \langle\psi_\mu^{(0)}| \mathsf{V} |\psi_\mu^{(j-1)}\rangle - \sum_{k=1}^{j-1} E_\mu^{(k)} \langle\psi_\mu^{(0)}| \psi_\mu^{(j-k)}\rangle . \tag{4.8}$$

Analogously, for the open-system case, we take the inner product of eq. (4.6) with the left eigenstate $(\breve{\mathsf{u}}_\mu^{(0)}|$. This yields the recursion relation for $\lambda_\mu^{(j)}$,

$$\lambda_\mu^{(j)} = (\breve{\mathsf{u}}_\mu^{(0)}| \mathbb{L}_1 \mathsf{u}_\mu^{(j-1)}) - \sum_{k=1}^{j-1} \lambda_\mu^{(k)} (\breve{\mathsf{u}}_\mu^{(0)}| \mathsf{u}_\mu^{(j-k)}) . \tag{4.9}$$

Note that eq. (4.8) is usually simplified further by demanding $\langle\psi_\mu^{(0)}|\psi_\mu^{(j)}\rangle = 0$ for $j \neq 0$ (and adjusting the overall normalization of states after all corrections are determined). We will instead keep the corresponding term $(\breve{\mathsf{u}}_\mu^{(0)}|\mathsf{u}_\mu^{(j-k)})$ in eq. (4.9) for reasons that will become clear momentarily.

We next turn to the computation of the eigenstate corrections. The Hamiltonian of any closed system is hermitian. Hence, H_0 provides a complete orthonormal eigenbasis $\{|\psi_\mu^{(0)}\rangle\}$. As a result, $|\psi_\mu^{(j)}\rangle$ in eq. (4.7) can be decomposed in this eigenbasis. Solving eq. (4.7) is then straightforward. By contrast, $\mathbb{L}$ is not hermitian and may not even be diagonalizable. As a result, the decomposition of $|\mathsf{u}_\mu^{(j)})$ in terms of $|\mathsf{u}_\mu^{(0)})$ may fail[2]. To solve the recursive expression (4.6) for the correction $|\mathsf{u}_\mu^{(j)})$, we therefore adopt the strategy of applying an appropriate generalized inverse to the singular[3] superoperator $(\mathbb{L}_0 - \lambda_\mu^{(0)})$. Several options exist for such a generalized inverse [101, 102, 107, 120]; here, we choose

[2]For the study of non-Hermitian Hamiltonians, the phenomenon of incomplete eigenbasis is widely known as self-orthogonality or exceptional point [122, Sec. 9.1].

[3]The superoperator $(\mathbb{L}_0 - \lambda_\mu^{(0)})$ is singular since $(\mathbb{L}_0 - \lambda_\mu^{(0)})|\mathsf{u}_\mu^{(0)}) = 0$.

the Moore-Penrose pseudoinverse which is well-defined for non-invertible matrices $\mathbb{A}$ and which we denote by $\mathbb{A}^{\leftarrow 1}$. (A brief review of the Moore-Penrose pseudoinverse is provided in appendix A.1.) Applying the pseudoinverse to eq. (4.6), we obtain

$$\left|\mathsf{u}_\mu^{(j)}\right) = \left(\mathbb{L}_0 - \lambda_\mu^{(0)}\right)^{\leftarrow 1} \left[-\mathbb{L}_1 \left|\mathsf{u}_\mu^{(j-1)}\right) + \left|\Delta_\mu^{(j)}\right)\right]. \tag{4.10}$$

Details of the derivation of eq. (4.10) are given below in appendix A.2. We emphasize that this pseudoinverse does not guarantee that $(\breve{\mathsf{u}}_\mu^{(0)}|\mathsf{u}_\mu^{(j)}) = 0$, explaining our previous remark on not demanding this term vanishing.

The steady-state density matrix $|\rho_s) \equiv |\mathsf{u}_0)$ defined by $\mathbb{L}|\rho_s) = 0$ [eq. (3.19)] is of particular interest. As a special case of eqs. (4.9) and (4.10), we can simplify the corrections $\lambda_0^{(j)}$ and $|\rho_s^{(j)})$ to

$$\lambda_0^{(j)} = 0, \tag{4.11}$$

$$\left|\rho_s^{(j)}\right) = -\mathbb{L}_0^{\leftarrow 1}\mathbb{L}_1 \left|\rho_s^{(j-1)}\right), \tag{4.12}$$

see appendix A.3 for details.

Corrections to λ_0 and ρ_s were previously derived without using the Moore-Penrose pseudoinverse [120]. The result for the density-matrix corrections in ref. 120 differs from ours [eq. (4.12)] merely by a shift,

$$\left|\rho_s^{(j)}\right) \to \left|\rho_s^{(j)}\right) + c_j \left|\rho_s^{(0)}\right), \tag{4.13}$$

where c_j is a constant. This shift can be interpreted as follows. Note that eq. (4.6) does not have a unique solution since $(\mathbb{L}_0 - \lambda_\mu^{(0)})$ is non-invertible. Indeed, for any given solution

$|\rho_s^{(j)})$ of eq. (4.6) its shifted counterpart from eq. (4.13) is also a solution. The choice of a particular generalized inverse effectively selects a specific set of shift parameters c_j. The difference between the result in ref. 120 and ours merely reflects the different choices of generalized inverses. Since shifts of the form of eq. (4.13) only affect the overall normalization of $|\rho_s)$, our result for the steady state corrections is equivalent to that given in ref. 120. We properly normalize our result by

$$|\rho_s) = \mathbb{N}\left[\sum_{j=0}^{\infty} \alpha^j \left|\rho_s^{(j)}\right)\right], \tag{4.14}$$

with $\mathbb{N}[\mathsf{A}] \equiv \mathsf{A}/\mathrm{Tr}\,[\mathsf{A}]$ effecting normalization for any non-traceless operator A.

As a special case, if $\mathbb{L}_0$ is diagonalizable and its eigenstates form a complete set, it is more convenient to define the inversion of $\mathbb{L}_0$ to be restricted to the space orthogonal to the unperturbed steady state, i.e.,

$$\mathbb{L}_0^{-1} = \sum_{\mu>0} (\lambda_\mu^{(0)})^{-1} |\mathsf{u}_\mu)(\breve{\mathsf{u}}_\mu|. \tag{4.15}$$

We can then use this generalized inverse $\mathbb{L}_0^{-1}$ to modify eq. (4.12),

$$\left|\rho_s^{(j)}\right) = -\mathbb{L}_0^{-1}\mathbb{L}_1 \left|\rho_s^{(j-1)}\right). \tag{4.16}$$

Here, one can readily show that the corrections $|\rho_s^{(j)})$ defined recursively by eq. (4.16) are traceless[4]. Hence, the normalization is trivial and eq. (4.14) is simplified to

$$|\rho_s) = \sum_{j=0}^{\infty} \alpha^j \left|\rho_s^{(j)}\right). \tag{4.17}$$

[4]Note the property that $\mathrm{Tr}[1\mathbb{L}_0^{-1}\mathsf{A}] = \sum_{\mu>0}(\lambda_\mu^{(0)})^{-1}(\breve{\mathsf{u}}_0|\mathsf{u}_\mu)(\breve{\mathsf{u}}_\mu|\mathsf{A}) = 0$ for any operator A.

Just as in closed-system PT, finite-order PT truncates the series in eq. (4.14). Let us denote the approximate result up to M-th order as $|\rho_s^M) \equiv \mathbb{N}[\sum_{j=0}^{M} \alpha^j |\rho_s^{(j)})]$.[5] We next check whether $|\rho_s^M)$ indeed represents a proper density matrix, i.e., whether it is normalized, hermitian and positive-semidefinite (section 3.1.1). By virtue of $\mathbb{N}$, the finite-order result $|\rho_s^M)$ is explicitly normalized. Hermiticity can be verified by noting that $\mathbb{L}_0^{\leftarrow 1}$ and $\mathbb{L}_1$ map hermitian operators to hermitian operators. However, omission of higher-order terms in the truncation can render $|\rho_s^M)$ non-positive. In the examples presented later on, this issue indeed occurs for certain parameter choices. Beyond mere conceptual concerns, non-positivity also prevents direct calculation of quantities such as state fidelity and von-Neumann entropy. This marks a key difference between closed-system PT and density-matrix PT. In closed-system PT, the approximate result is always a proper quantum state. By contrast, for density-matrix PT the approximate result may, strictly speaking, not be a proper density matrix.

Similar issues with non-positivity of approximate density matrices are also encountered in quantum tomography, there caused by measurement errors. In this case, a maximum-likelihood method is typically used to reconstruct a physical density matrix from the non-positive approximation [123, 124]. However, this method is impractical to apply to the large density matrices we are interested in. We next discuss an alternative strategy which reinstates positivity for large density matrices obtained within PT.

[5]Here, we work with the general case involving the Moore-Penrose pseudoinverse and thus normalization is necessary.

4.2. Amplitude-matrix perturbation theory

We propose an amplitude-matrix PT to perturbatively construct an approximate steady-state density matrix which is manifestly positive. For this, recall that any hermitian and positive-semidefinite matrix $\rho \leftrightarrow |\rho)$ can be decomposed in the form [125, p. 407]: $\rho = \zeta\zeta^\dagger$. Following ref. 126, we will refer to ζ as the amplitude matrix. The decomposition $\rho = \zeta\zeta^\dagger$ is not unique: there are many choices for ζ leading to the same matrix ρ. To eliminate these extra degrees of freedom, we choose ζ to be lower triangular with real, non-negative diagonal elements. Existence and uniqueness of ζ are then guaranteed by the Cholesky decomposition. (In the case that ρ possesses a zero eigenvalue, the Cholesky decomposition is not unique but this issue can be bypassed by known strategies [127, 128].)

We start from the power series expansion of the steady-state amplitude matrix in α: $\zeta_\mathrm{s} = \sum_{j=0}^{\infty} \alpha^j \zeta_\mathrm{s}^{(j)}$. Here, all matrices $\zeta_\mathrm{s}^{(j)}$ are again of lower triangular shape. Plugging this expansion into $\rho_s = \zeta_\mathrm{s}\zeta_\mathrm{s}^\dagger$ and collecting terms of the same order in α, we obtain

$$\zeta_\mathrm{s}^{(0)} \left(\zeta_\mathrm{s}^{(0)}\right)^\dagger = \rho_s^{(0)}, \tag{4.18}$$

$$\mathbb{Z}\zeta_\mathrm{s}^{(j)} = \rho_s^{(j)} - \sum_{k=1}^{j-1} \zeta_\mathrm{s}^{(k)} \left(\zeta_\mathrm{s}^{(j-k)}\right)^\dagger. \tag{4.19}$$

Here, the superoperator $\mathbb{Z}$ is defined via $\mathbb{Z}\mathsf{A} = \zeta_\mathrm{s}^{(0)}\mathsf{A}^\dagger + \mathsf{A}\,(\zeta_\mathrm{s}^{(0)})^\dagger$. The zero-order amplitude matrix $\zeta_\mathrm{s}^{(0)}$ is directly obtained from eq. (4.18) by Cholesky decomposition and $\zeta_\mathrm{s}^{(j)}$ is determined recursively from the system of linear equations in eq. (4.19). We determine $\rho_s^{(j)}$ in eq. (4.19) by density-matrix PT; in this sense, the amplitude-matrix PT is based on the density-matrix PT.

Once we truncate the amplitude matrix to M-th order, $\zeta_{\rm s}^M \equiv \sum_{j=0}^M \alpha^j \zeta_{\rm s}^{(j)}$, we can compute the steady-state density matrix $\rho_{\rm s,AM}^M$ by

$$\rho_{\rm s,AM}^M = \mathbb{N}\left[\zeta_{\rm s}^M \left(\zeta_{\rm s}^M\right)^\dagger\right]. \tag{4.20}$$

Now, $\rho_{\rm s,AM}^M$ is manifestly a proper density matrix: it is normalized, hermitian and positive-semidefinite by construction. Looking ahead, expectation values for observables obtained from amplitude-matrix PT, however, are not necessarily more accurate than those obtained from density-matrix PT. Even if the steady state ρ_s^M approximated by density-matrix PT is slightly non-positive, its accuracy is the same as that from amplitude-matrix PT. (Both are accurate up to order M.) The examples in the following section illustrate that the respective accuracies of density-matrix versus amplitude-matrix PT generally depend on the specific perturbation and system parameters.

Amplitude-matrix PT is more involved if one or more eigenvalues of $\rho_s^{(0)}$ vanish, e.g. when $\rho_s^{(0)}$ represents a pure state. In that case, the superoperator $\mathbb{Z}$ in eq. (4.19) is non-invertible (see appendix A.4) and thus a unique solution for eq. (4.19) does not exist. Depending on the specific case, there may be infinitely many solutions or no solution. In the case of infinitely many solutions, we add a small identity-matrix component to $\rho_s^{(0)}$, i.e., $\rho_s^{(0)} \to \rho_s^{(0)} + c\mathbb{1}$ with $0 < c \ll 1$. The identity matrix then acts as a correction matrix which stabilizes the procedure of solving the linear equation [eq. (4.19)] to provide a unique $\zeta_{\rm s}^{(j)}$. We utilize this correction matrix strategy in the second example discussed below. Whenever eq. (4.19) has no solution, other forms of series expansions need to be applied. We will not further consider that case here. The correction-matrix method and the validity of the series expansion are further discussed in appendix A.4.

4.3. Comparing PT with exact results

To illustrate the use and assess the accuracy of density-matrix and amplitude-matrix PT, we study two example systems, see fig. 4.2. These two examples are not claimed to be particularly original. Our selection is guided by the intention to discuss two systems that are non-trivial, yet sufficiently small to still allow for a numerically exact treatment of the master equation. This way, we can compare steady-state expectation values from second-order PT with those obtained from exact diagonalization of $\mathbb{L}$. We note again that the steady-state result obtained from finite-order density-matrix PT can be non-positive. This is indeed the case for some choices of parameters in the two following examples. Thus, we also apply the amplitude-matrix PT and compare results from the two perturbative treatments.

4.3.1. Four driven and damped spins coupled in a ring

We consider four spins coupled in a ring as shown in fig. 4.2(a). The spins are coupled by flip-flop interaction with spin-spin coupling strength t. We assume all spins are driven equally with strength ϵ and drive frequency ω_d. Within the rotating wave approximation, the Hamiltonian describing this system is given by

$$\mathsf{H} = \sum_n \left[\delta\Omega\, \sigma_n^+ \sigma_n^- + \epsilon(\sigma_n^+ + \sigma_n^-)\right] + t \sum_n \left(\sigma_n^+ \sigma_{n+1}^- + \text{h.c.}\right). \tag{4.21}$$

Here, $\sigma_n^\pm$ are the raising or lowering operators for the spin at site n, and $\delta\Omega \equiv \Omega - \omega_d$ is the detuning between the spin frequency Ω and the drive frequency ω_d. Note that in eq. (4.21), the time dependence of the drive has already been eliminated by working in a frame co-rotating with the drive. All four spins are coupled to a zero-temperature bath,

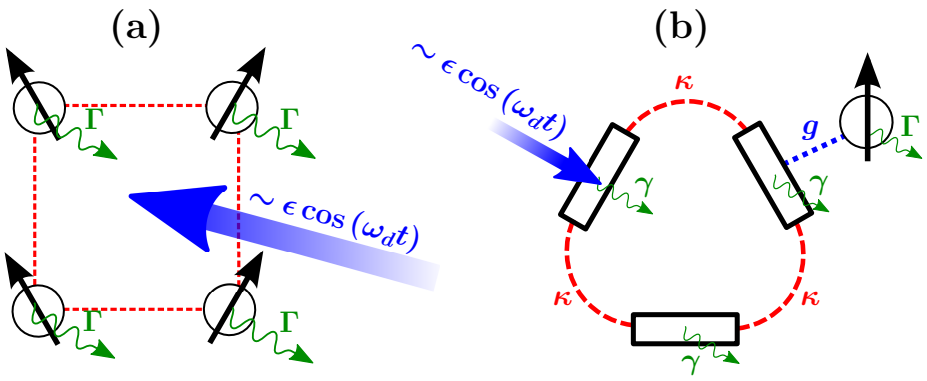

Figure 4.2. **Schematic of the examples**. (a) The first system consists of a ring of four coupled spins with nearest-neighbor flip-flop interaction of strength t (dashed red lines). The spins are jointly driven with a coherent tone of strength ϵ and frequency ω_d (blue arrow). Each spin is further subjected to local dissipation with spin relaxation rate Γ (green curly arrows). (b) The second system is composed of a three-resonator ring (black rectangles). One resonator is coupled to a single qubit with Jaynes-Cummings interaction strength g (blue dotted line). The resonators are coupled to each other through photon hopping with rate κ (red dashed lines). One of the resonators is driven coherently (blue arrow). Resonators and qubit are subject to local dissipation with photon decay rate γ and qubit relaxation rate Γ (green curly arrows).

leading to pure spin relaxation with relaxation rate Γ. Thus, the Liouville superoperator $\mathbb{L}$ is given by

$$\mathbb{L}\rho = -i[\mathsf{H}, \rho] + \Gamma \sum_n \mathbb{D}\left[\sigma_n^-\right] \rho, \tag{4.22}$$

where $\mathbb{D}\left[\sigma_n^-\right] \rho \equiv \sigma_n^- \rho \sigma_n^+ - \frac{1}{2}\sigma_n^+ \sigma_n^- \rho - \frac{1}{2}\rho \sigma_n^+ \sigma_n^-$ is the usual dissipator for spin relaxation.

As the perturbation, we choose the spin-spin coupling and, thus, separate $\mathbb{L}$ into two parts, $\mathbb{L} = \mathbb{L}_0 + t\,\mathbb{L}_1$ where

$$\mathbb{L}_0 \rho = \sum_n \{-i\left[\delta\Omega \sigma_n^+ \sigma_n^- + \epsilon(\sigma_n^+ + \sigma_n^-), \rho\right] + \Gamma\, \mathbb{D}\left[\sigma_n^-\right] \rho\}$$

describes the "atomic limit" in which the spin-spin coupling is absent, and the perturbation

$$t\,\mathbb{L}_1\rho = t\sum_n -i\left[\left(\sigma_n^+\sigma_{n+1}^- + \sigma_n^-\sigma_{n+1}^+\right),\rho\right] \tag{4.23}$$

captures the spin-spin coupling. Orders of perturbation theory are counted with respect to t. Even though the system possesses a high degree of symmetry, the steady states of the unperturbed and perturbed systems are unique. Hence, the zero-eigenvalues of $\mathbb{L}_0$ and $\mathbb{L}$ are non-degenerate and non-degenerate PT for the steady state is applicable.

We can thus implement second-order PT to compute the steady-state expectation values for several operators such as σ_1^- and the excitation number $\sigma_1^+\sigma_1^-$. These two expectation values fully capture the reduced density matrix of a single spin (which is the same for all spins due to symmetry). In fig. 4.3, we compare results from density-matrix PT and amplitude-matrix PT to the exact and the unperturbed results.

We first consider the case shown in fig. 4.3(a) and (b), where the coupling strength t represents the smallest energy scale. Consistent with findings in ref. 129, we observe two symmetric resonance peaks in $|\langle\sigma_1^-\rangle|$ for the unperturbed result (separate spins). When the coupling is present, the two peaks are shifted in position and become asymmetric, in agreement with the results from ref. 30. For $\langle\sigma_1^+\sigma_1^-\rangle$, we observe a similar shift and asymmetry in the resonance peak due to the spin-spin coupling. Second-order PT nicely captures the above features. Note that the amplitude-matrix-PT result is actually slightly less accurate than the density-matrix-PT result in this particular case.

To illustrate the expected limitations of PT, we next increase the coupling strength so much that it matches the drive strength. Results for this parameter choice are shown in fig. 4.3(c) and (d). Qualitatively, the behavior predicted by the exact calculation is still

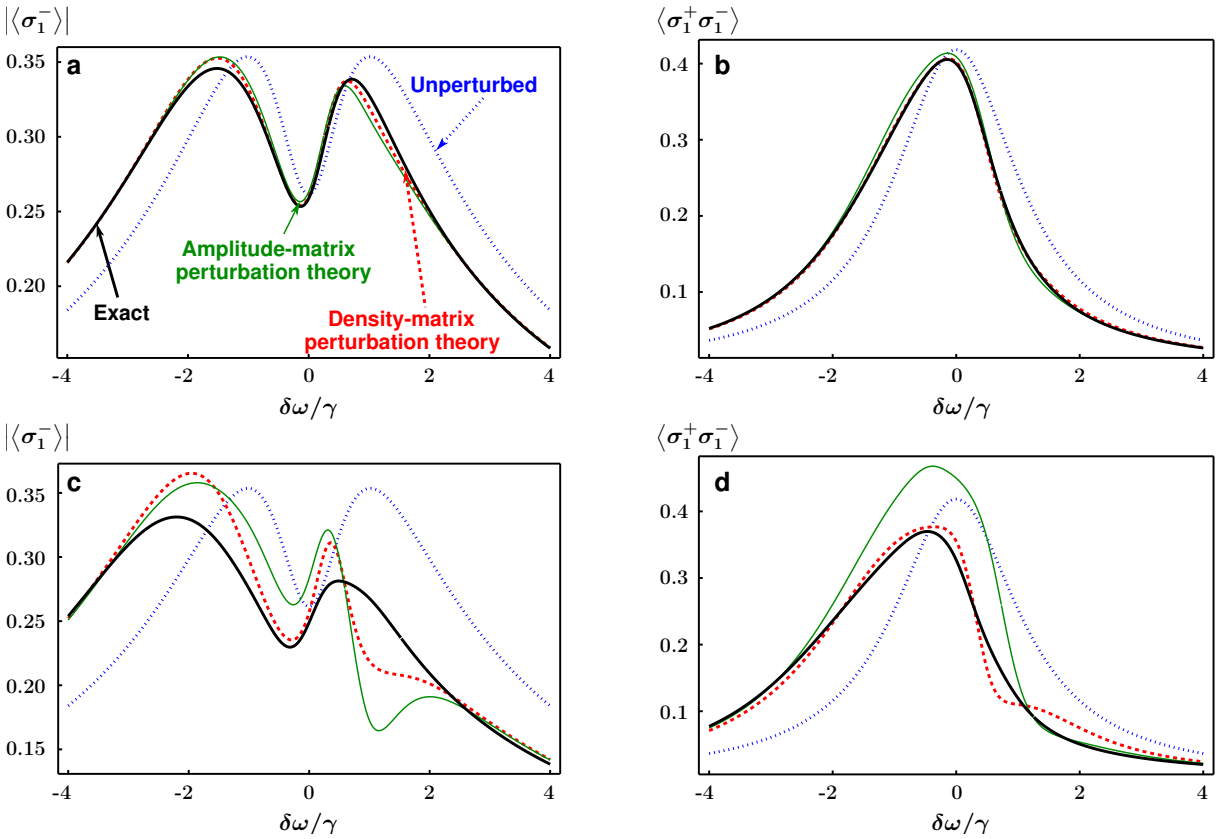

Figure 4.3. **Results for four spins coupled in a ring**. Shown are: the unperturbed result with respect to $\mathbb{L}_0$ (blue dotted line), the exact result from diagonalizing $\mathbb{L}$ (black solid line), the second-order density-matrix-PT result (red dashed line) and the second-order amplitude-matrix-PT result (green thin line). (a) and (b): $|\langle\sigma_1^-\rangle|$ and $\langle\sigma_1^+\sigma_1^-\rangle$ are plotted as a function of $\frac{\delta\Omega}{\Gamma}$ for $\frac{\epsilon}{\Gamma} = 0.8$ and $\frac{t}{\Gamma} = 0.4$. The exact result is well approximated by the second-order PT result. The amplitude-matrix PT is slightly less accurate in this case, as is best visible for $\langle\sigma_1^+\sigma_1^-\rangle$. (c) and (d): The same quantities are plotted, here for increased $\frac{t}{\Gamma} = 0.8$ to illustrate the expected limitation of PT. Although deviations are significant, the qualitative behavior exhibited by the exact result is captured by second-order PT.

captured by the perturbative results. However, quantitatively, the results from PT show significant deviations from the exact result. (Large deviations like this are expected since the "perturbation" parameter t now matches both ϵ and Γ and PT breaks down.)

It is an interesting question whether a dimensionless parameter α can be identified that governs the convergence of this PT. To investigate this question, we recall that in simple cases of closed-system PT, α may be inferred from the expression for second-order corrections. α is then given by the ratio of the perturbation strength t and the difference between the relevant unperturbed eigenenergies; for instance, for the ground state we have:

$$\alpha = \frac{t}{|E_0^{(0)} - E_1^{(0)}|} \qquad \text{(closed system)}. \tag{4.24}$$

where $E_0^{(0)}$ and $E_1^{(0)}$ are the unperturbed ground state and first excited state energies, respectively. For open systems, the unperturbed eigenvalues of the Hamiltonian are replaced by those of the superoperator $\mathbb{L}_0$. For the steady state, the relevant eigenvalue difference is that between the steady-state eigenvalue zero and that of the closest non-zero eigenvalues,

$$\alpha = \frac{t}{\min_{\mu\neq 0}\left|\lambda_\mu^{(0)} - \lambda_0\right|} = \frac{t}{\min_{\mu\neq 0}\left|\lambda_\mu^{(0)}\right|}. \tag{4.25}$$

Even for a simple system like a driven-damped spin, the spectrum of complex eigenvalues $\lambda_\mu^{(0)}$ depends on the system parameters $\delta\Omega$, ϵ and γ in a rather non-trivial way, see fig. 3.2. The tuning of system parameters can even change *which* eigenvalue $\lambda_\mu^{(0)}$ is closest to zero, resulting, for example, in a discontinuous switch from a purely real λ_{ADR} (ADR eigenvalue) to a complex pair of λ_{ADR}. Hence, it is in general difficult to write the small parameter α in a simple form showing the dependence on the various system parameters.

4.3.2. Qubit coupled to a driven and damped resonator ring

As our second example, we choose a system composed of a single qubit coupled to a three-resonator ring, see fig. 4.2(b). The resonators are coupled among each other by photon hopping with rate κ. The first resonator is driven with strength ϵ and drive frequency ω_d. The qubit is coupled to the second resonator with a coupling strength g. Within the rotating wave approximation and in the frame co-rotating with the drive, the system Hamiltonian H is given by

$$\begin{aligned}\mathsf{H} = &\sum_{n=1}^{3} \delta\omega\, \mathsf{a}_n^\dagger \mathsf{a}_n + \epsilon\left(\mathsf{a}_1 + \mathsf{a}_1^\dagger\right) + \delta\Omega\, \sigma^+\sigma^- + g\left(\mathsf{a}_2\sigma^+ + \mathsf{a}_2^\dagger\sigma^-\right) \\ &+ \kappa\left(\mathsf{a}_1^\dagger\mathsf{a}_2 + \mathsf{a}_2^\dagger\mathsf{a}_3 + \mathsf{a}_3^\dagger\mathsf{a}_1 + \text{h.c.}\right). \end{aligned} \tag{4.26}$$

Here, a_n ($\mathsf{a}_n^\dagger$) is the annihilation (creation) operator for photons in the resonator at site n and $\delta\omega \equiv \omega - \omega_d$ is the detuning between the bare resonator frequency ω and the drive frequency ω_d. The qubit is assumed to be in resonance with the bare resonator frequency. Qubit and resonators are each coupled to zero-temperature baths, inducing qubit relaxation and photon decay with rates Γ and γ, respectively. The superoperator $\mathbb{L}$ is thus given by

$$\mathbb{L}\rho = -i\left[\mathsf{H}, \rho\right] + \gamma \sum_n \mathbb{D}\left[\mathsf{a}_n\right]\rho + \Gamma\mathbb{D}\left[\sigma^-\right]\rho. \tag{4.27}$$

The qubit-resonator coupling mediates two effects: an indirect coherent drive on the qubit, and correlations between the resonator ring and the qubit. We wish to treat the correlation effects perturbatively. To do so, we separate the two effects by means of a coherent displacement as follows. Note that in the absence of qubit-resonator coupling,

the drive places the eigenmodes $\mu = 1, 2, 3$ of the resonator ring in coherent states with amplitudes $\langle \mathsf{b}_\mu \rangle^{(0)} \equiv \beta_\mu$ where

$$\beta_\mu = -\frac{\epsilon}{\sqrt{3}} \left(\delta\Omega + 2\kappa \cos \tfrac{2\pi\mu}{3} - i\tfrac{\gamma_a}{2} \right)^{-1} e^{i\frac{2\pi\mu}{3}} \tag{4.28}$$

and $\mathsf{b}_\mu \equiv \frac{1}{\sqrt{3}} \sum_n a_n \exp(i\frac{2\pi}{3}\mu n)$ is the annihilation operator for photons in mode μ. We thus displace b_μ according to

$$\mathsf{b}'_\mu = \mathsf{b}_\mu - \beta_\mu. \tag{4.29}$$

and rewrite the Liouville superoperator as

$$\mathbb{L}\rho = -i \left[\mathsf{H}_0 + g\mathsf{H}_1, \rho \right] + \gamma \sum_\mu \mathbb{D} \left[\mathsf{b}'_\mu \right] \rho + \Gamma \mathbb{D} \left[\sigma^- \right] \rho.$$

Here, H_0 is the unperturbed Hamiltonian

$$\mathsf{H}_0 = \sum_\mu \left(\delta\omega + 2\kappa \cos \tfrac{2\pi\mu}{3} \right) \left(\mathsf{b}'_\mu \right)^\dagger \mathsf{b}'_\mu + \delta\Omega\, \sigma^+\sigma^- + \left(\epsilon_{\text{eff}}\, \sigma^+ + \epsilon^*_{\text{eff}} \sigma^- \right) \tag{4.30}$$

in which the displaced eigenmodes b'_μ and the qubit are decoupled. One finds that the effective drive on the qubit is given by $\epsilon_{\text{eff}} \equiv \frac{g}{\sqrt{3}} \sum_\mu \beta_\mu \exp(-i\frac{4\pi\mu}{3})$. The perturbation $g\mathsf{H}_1$ describes the remaining coupling between the displaced eigenmodes and the qubit,

$$g\mathsf{H}_1 = \frac{g}{\sqrt{3}} \sum_\mu \left(e^{-i\frac{4\pi\mu}{3}} \mathsf{b}'_\mu \sigma^+ + \text{h.c.} \right). \tag{4.31}$$

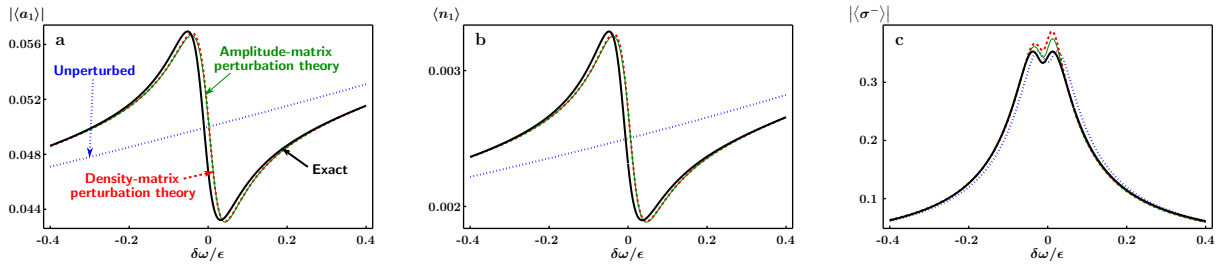

Figure 4.4. **Results for single qubit coupled to a resonator ring**. The color scheme of fig. 4.3 is used. We plot $|\langle a_1\rangle|$, $\langle n_1\rangle$ and $|\langle\sigma^-\rangle|$ as a function of $\frac{\delta\Omega}{\epsilon}$ for $\frac{\kappa}{\epsilon}=10$, $\frac{g}{\epsilon}=0.5$ and $\frac{\gamma_q}{\epsilon}=\frac{\gamma_a}{\epsilon}=0.05$. The resonance at $\delta\Omega=0$ is well captured by second-order PT. The amplitude-matrix PT and density-matrix PT yield with nearly identical accuracies.

The perturbative treatment then simply involves separating the Liouville superoperator, i.e. $\mathbb{L}=\mathbb{L}_0+g\,\mathbb{L}_1$, into the unperturbed superoperator

$$\mathbb{L}_0\rho=-i\left[\mathsf{H}_0,\rho\right]+\gamma\sum_\mu\mathbb{D}\left[\mathsf{b}'_\mu\right]\rho+\Gamma\mathbb{D}\left[\sigma^-\right]\rho. \tag{4.32}$$

and a perturbation which captures the remaining coupling,

$$g\,\mathbb{L}_1\rho=-i\left[g\mathsf{H}_1,\rho\right]. \tag{4.33}$$

The order of perturbation theory here is counted with respect to g.

We then apply second-order PT to determine the corrections to the steady state of $\mathbb{L}_0$. The unperturbed steady state $|\rho_s^{(0)}\rangle$ is a product state composed of a density matrix for the resonator ring and one for the qubit. The resonator ring is in a pure state (all displaced eigenmodes in the vacuum state). As a consequence, $|\rho_s^{(0)}\rangle$ has multiple eigenvalues zero. Therefore, when implementing amplitude-matrix PT, we employ the correction matrix method mentioned above (with parameter $c=10^{-9}$).

Density-matrix PT and Amplitude-matrix PT determine the steady-state density matrix according to eqs. (4.14) and (4.20), respectively. We will focus on expectation values at site 1, specifically $|\langle \mathsf{a}_1 \rangle|$ and $\langle \mathsf{n}_1 \rangle \equiv \langle \mathsf{a}_1^\dagger \mathsf{a}_1 \rangle$, as a function of the drive frequency, expressed in terms of the detuning $\delta\omega$. In the unperturbed, i.e., decoupled case ($g = 0$), we expect two resonances at $\delta\omega = -2\kappa$ and $\delta\omega = \kappa$ corresponding to the eigenmodes of the resonator ring. Once the qubit is coupled to the resonator ring, we expect a resonance at $\delta\omega = 0$ originating from the qubit's response to the drive. We monitor this response by calculating the expectation value $|\langle \sigma^- \rangle|$.

As shown in fig. 4.4, we confirm that the resonance at $\delta\omega = 0$, a key consequence of the coupling, is successfully captured by second-order PT. Specifically, we consider the case where drive and coupling strengths ϵ and g are small compared to the hopping rate κ, but large compared to the relaxation and decay rates Γ and γ. Note that the perturbation parameter g is *not* the smallest energy scale in this case; nonetheless, PT holds. The expectation values $|\langle \mathsf{a}_1 \rangle|$, $\langle \mathsf{n}_1 \rangle$ and $|\langle \sigma^- \rangle|$ are shown in fig. 4.4(a), (b) and (c) respectively. The results from second-order PT are in good agreement with the exact result. Amplitude-matrix PT and density-matrix PT here give results with nearly identical accuracies. The saturation effect visible in fig. 4.4(c) shows that the qubit is in the nonlinear regime. These results also illustrate that the correction matrix method required for the amplitude-matrix PT reliably yields results consistent with the exact solution.

4.4. General Resummation Framework for steady state

In the following, we will focus on the steady-state physics and take a vital step to go beyond finite-order PT by demonstrating a general resummation scheme[6]. I will first present a resummation formalism for the Lindblad perturbation theory in this section. The concrete application of the formalism to an open Jaynes-Cummings lattice follows in section 4.5.

Consider the general case of an open quantum system with Hamiltonian H and Liouville superoperator $\mathbb{L}$. We shall assume that $\mathbb{L}$ is amenable to a perturbative treatment and can be decomposed into a sum $\mathbb{L} = \mathbb{L}_0 + \mathbb{L}_1$ [eq. (4.4) with the order-counting parameter α taken to be 1], consisting of the unperturbed Liouville superoperator $\mathbb{L}_0$, and the perturbation $\mathbb{L}_1$. As discussed in section 4.1, we expect in particular that the exact spectrum $\{\lambda_\mu^{(0)}, |\mathsf{u}_\mu^{(0)}), (\breve{\mathsf{u}}_\mu^{(0)}|\}$ of $\mathbb{L}_0$ can be obtained.

The spectra of $\mathbb{L}$ and $\mathbb{L}_0$ differ, but corrections may be calculated by the density-matrix PT [eqs. (4.9) and (4.10)] if $\mathbb{L}_1$ is "sufficiently small." Here, our interest primarily regards the steady state ρ_s. We apply density-matrix PT assuming the steady state is unique and eigenstates span the full operator space. Two remarks may be useful for clarification. First, we emphasize that non-degeneracy refers to the spectrum of $\mathbb{L}_0$, *not* to that of the Hamiltonian H; we make no assumptions about the spectrum of H. Second, we note that non-uniqueness of the steady state and non-analyticities are crucial at the phase boundary of a dissipative phase transition. Perturbative series expansions will generally not hold directly at such a boundary, but may still be applicable in its vicinity.

[6]Steady-state behavior can be directly related to experimental observables such as microwave transmission in circuit-QED lattices [53–55, 129]. Steady-state quantities are also of paramount importance for the detection of dissipative phase transitions to be discussed in section 6.1.

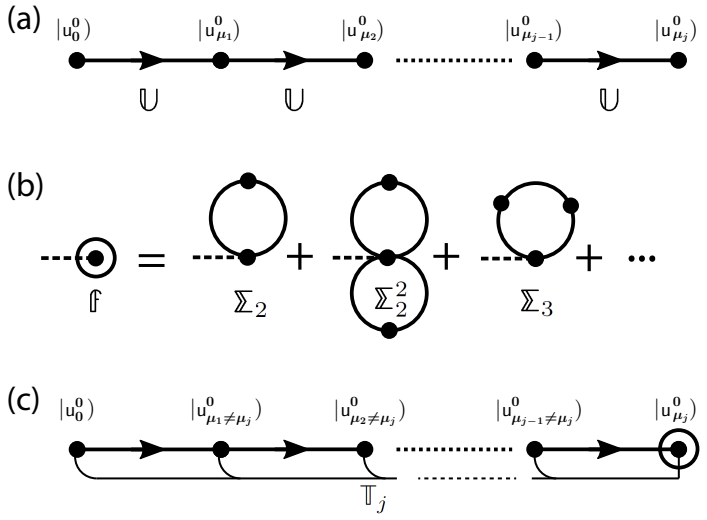

Figure 4.5. **Diagrams for perturbative corrections**. (a) The order-j correction to the steady state [eq. (4.37)] is depicted as a chain of j lines, each representing one factor $\mathbb{U}$. The chain connects $j+1$ dots symbolizing $\mathbb{L}_0$-eigenstates. The leftmost state is the unperturbed steady state $|\rho_s^{(j)}) = |\mathsf{u}_0^{(0)})$, the rightmost one the unperturbed eigenstate $|\mathsf{u}_{\mu_j}^{(0)})$. One fully labeled diagram gives rise to one specific correction term. The full correction is obtained by summation over all final and intermediate states $\mu_1, \ldots, \mu_j$. (b) The resummation superoperator $\mathbb{f}$ is the sum of all (reducible and irreducible) $\mathbb{\Sigma}$-superoperators. Each $\mathbb{\Sigma}$-diagram starts and ends with the same unperturbed eigenstate. (c) Resummation combines evaluation of $\mathbb{\Sigma}$ and $\mathbb{T}$-superoperators. Terms of rank j are comprised of the fully off-diagonal chain specified by $\mathbb{T}_j$ and final application of the resummation superoperator.

Turning now to the concrete series expansion $|\rho_s) = \sum_j |\rho_s^{(j)})$ of the steady state, the j-th order contribution $\rho_s^{(j)}$ is obtained from the recursion relation (4.16)[7]:

$$|\rho_s^{(j)}) = -\mathbb{L}_0^{-1}\mathbb{L}_1|\rho_s^{(j-1)}). \tag{4.34}$$

[7]As discussed in section 4.3, the steady-state expectation values obtained from density-matrix PT showed good agreement in the two examples even if the truncated density matrix was slightly non-positive. It is thus sufficient to base the resummation scheme on density-matrix PT.

As explained in section 4.1, inversion of $\mathbb{L}_0$ will always be understood as restricted to the space orthogonal to the unperturbed steady state, i.e., $\mathbb{L}_0^{-1} = \sum_{\mu>0}(\lambda_\mu^{(0)})^{-1}|\mathsf{u}_\mu)(\breve{\mathsf{u}}_\mu|$. With this, we obtain the formal expression

$$|\rho_s^{(j)}) = \left(-\mathbb{L}_0^{-1}\mathbb{L}_1\right)^j |\rho_s^{(0)}) = \mathbb{U}^j|\rho_s^{(0)}), \tag{4.35}$$

where $\rho_s^{(0)}$ is the unperturbed steady state of $\mathbb{L}_0$, and we have introduced the shorthand $\mathbb{U} \equiv -\mathbb{L}_0^{-1}\mathbb{L}_1$. The matrix elements of the $\mathbb{U}$-superoperator are

$$(\mathbb{U})_{\mu\nu} = (\breve{\mathsf{u}}_\mu^{(0)}|\mathbb{U}|\mathsf{u}_\nu^{(0)}) = -(\breve{\mathsf{u}}_\mu^{(0)}|\mathbb{L}_1|\mathsf{u}_\nu^{(0)})/\lambda_\mu^{(0)} \tag{4.36}$$

for $\mu > 0$ and $(\mathbb{U})_{0\nu} = 0$. Using this shorthand, we write the j-th order contribution to the steady state in the form of the chain expression

$$|\rho_s^{(j)}) = \sum_{\mu_1,\mu_2,\cdots,\mu_j} |\mathsf{u}_{\mu_j}^{(0)}) \cdot (\mathbb{U})_{\mu_j\mu_{j-1}} \cdots (\mathbb{U})_{\mu_2\mu_1} (\mathbb{U})_{\mu_1 0}\,, \tag{4.37}$$

and represent it diagrammatically as shown in fig. 4.5(a). As a diagrammatic rule, we choose dots to represent unperturbed eigenstates, $|\mathsf{u}_{\mu_j}^{(0)})$, and interconnecting lines to represent factors of $\mathbb{U}$. Reading from the left to right, the leftmost state is the unperturbed steady state $|\rho_s^{(0)}) = |\mathsf{u}_0^{(0)})$, and the rightmost one the final state $|\mathsf{u}_{\mu_j}^{(0)})$ which appears explicitly in the expression (4.37). All intermediate states and the final state, μ_1 through μ_j are subject to summation, but cannot coincide with the initial unperturbed steady state due to $(\mathbb{U})_{0\nu} = 0$.

4.4.1. Resummation scheme

To facilitate our resummation scheme for the steady-state series [eq. (4.17)]

$$|\rho_s) = \sum_{j=0}^{\infty} \mathbb{U}^j |\rho_s^{(0)}), \tag{4.38}$$

we decompose the $\mathbb{U}$-superoperator into two parts

$$\mathbb{U}^1 = \mathbb{\Sigma}_1 + \mathbb{T}_1. \tag{4.39}$$

To make the definition parallel to expressions to come, we have explicitly recorded the exponent $j = 1$ on the left-hand side. We now specify the terms on the right-hand side in such a way that resummation takes a particularly simple form. We define the first-order $\mathbb{\Sigma}$-superoperator as the diagonal part of $\mathbb{U}^1$, i.e. $(\mathbb{\Sigma}_1)_{\mu\nu} = \delta_{\mu\nu}(\mathbb{U}^1)_{\mu\nu}$. Accordingly, $\mathbb{\Sigma}_1$ and $\mathbb{L}_0$ share the same set of right eigenstates, i.e., $\mathbb{\Sigma}_1|\mathsf{u}_\mu^{(0)}) = \Sigma_{1;\mu}|\mathsf{u}_\mu^{(0)})$, with corresponding eigenvalues $\Sigma_{1;\mu} = (\mathbb{U}^1)_{\mu\mu}$. We will see that this simplicity of $\mathbb{\Sigma}_1$ will be important for the resummation of the series, eq. (4.38). The term $\mathbb{T}_1$ in eq. (4.39) is the off-diagonal remainder of the $\mathbb{U}$-superoperator.

A simplification of the previous expressions occurs when making the natural assumption that the perturbation $\mathbb{L}_1$ is itself off-diagonal with respect to the unperturbed eigenstates of $\mathbb{L}_0$. (Whenever $\mathbb{L}_1$ does not satisfy this assumption, a simple re-definition of $\mathbb{L}_0$ and $\mathbb{L}_1$ can be used to make $\mathbb{L}_1$ off-diagonal.) Now, if $\mathbb{L}_1$ is off-diagonal, so is $\mathbb{U} = -\mathbb{L}_0^{-1}\mathbb{L}_1$ and we immediately obtain

$$\mathbb{\Sigma}_1 = 0 \quad \text{and} \quad \mathbb{T}_1 = \mathbb{U}. \tag{4.40}$$

This may initially make the decomposition of $\mathbb{U}$ seem pointless, but we will see momentarily that this simplification does not carry over to higher orders $j > 1$, thus justifying our approach.

We next consider the second-order term $\mathbb{U}^2|\rho_s^{(0)})$, which warrants a decomposition of $\mathbb{U}^2 = \mathbb{T}_1\mathbb{U}$ into

$$\mathbb{T}_1\mathbb{U} = \mathbb{\Sigma}_2 + \mathbb{T}_2. \tag{4.41}$$

Analogous to our strategy above, we define the second-order $\mathbb{\Sigma}$-superoperator, as the diagonal part of the left-hand side,

$$(\mathbb{\Sigma}_2)_{\mu\nu} = \delta_{\mu\nu}\,(\mathbb{T}_1\mathbb{U})_{\mu\nu} = \delta_{\mu\nu}\sum_\tau (\breve{\mathsf{u}}_\nu^{(0)}|\mathbb{U}|\mathsf{u}_\tau^{(0)})(\breve{\mathsf{u}}_\tau^{(0)}|\mathbb{U}|\mathsf{u}_\nu^{(0)}) = \delta_{\mu\nu}\sum_\tau (\mathbb{U})_{\nu\tau}\,(\mathbb{U})_{\tau\nu}\,. \tag{4.42}$$

Note that the off-diagonal character of $\mathbb{U}$ automatically leads to exclusion of the term with $\tau = \nu$. As before, $\mathbb{T}_2$ represents the remaining off-diagonal part in eq. (4.41). We represent $\mathbb{\Sigma}_2$ by the loop diagram shown in fig. 4.5(b). Since $\mathbb{\Sigma}_2$ is diagonal, its initial and final state $|\mathsf{u}_\mu^{(0)})$ must be identical. However, the intermediate state $|\mathsf{u}_\tau^{(0)})$ involved in the expression (4.42) must differ from $|\mathsf{u}_\mu^{(0)})$.

For resummation of terms to infinite order, we need to formulate our decomposition strategy for arbitrary order j. It is natural to extend the definitions for diagonal and off-diagonal superoperators, eqs. (4.41) and (4.42), by setting

$$\mathbb{T}_{j-1}\mathbb{U} = \mathbb{\Sigma}_j + \mathbb{T}_j, \qquad (\mathbb{\Sigma}_j)_{\mu\nu} = \delta_{\mu\nu}\,(\mathbb{T}_{j-1}\mathbb{U})_{\mu\nu}\,. \tag{4.43}$$

The recurrence relation is solved by

$$\mathbb{T}_j = [\![[\![\cdots[\![[\![\mathbb{U}]\!]\mathbb{U}]\!]\cdots\mathbb{U}]\!]\mathbb{U}]\!] \qquad (j \text{ times}), \tag{4.44}$$

where $[\![\mathbb{A}]\!]$ denotes the off-diagonal part of $\mathbb{A}$ with respect to the unperturbed basis $\{|\mathsf{u}_\mu^{(0)})\}$. We must note, however, that the definition (4.43) does not yet determine a unique separation scheme beyond second order. Consider, for instance, the case of the third-order term involving $\mathbb{U}^3$. While we know the decomposition of $\mathbb{U}^2 = \mathbb{T}_1\mathbb{U}$ from eq. (4.41), we still have the freedom to perform the substitution for either $\mathbb{U}^3 = \mathbb{U}(\mathbb{U}^2)$ or $\mathbb{U}^3 = (\mathbb{U}^2)\mathbb{U}$. Both forms are mathematically equivalent, but only the systematic usage of one replacement rule produces expressions for which resummation becomes simple. We will consistently employ the form

$$\mathbb{U}^j = \underline{\mathbb{U}^{j-1}}\,\mathbb{U}, \tag{4.45}$$

where $\underline{\mathbb{U}^{j-1}}$ signals that $\mathbb{U}^{j-1}$ is to be replaced by an expression composed of $\mathbb{\Sigma}$, $\mathbb{T}$, and $\mathbb{U}$-superoperators. Multiple replacements, in some cases making use of the identity $\mathbb{U} = \mathbb{T}_1$, may be necessary to reach the final decomposed form only involving $\mathbb{\Sigma}$ and $\mathbb{T}$-superoperators.

For illustration, we consider the decompositions of $\mathbb{U}^3$, $\mathbb{U}^4$, and $\mathbb{U}^5$. For the third-order case, we first make use of eq. (4.45) and then eq. (4.43) to obtain

$$\mathbb{U}^3 = \underline{\mathbb{U}^2}\,\mathbb{U} = \underline{\mathbb{T}_1\mathbb{U}}\,\mathbb{U} = \mathbb{T}_2\mathbb{U} + \mathbb{\Sigma}_2\mathbb{U}. \tag{4.46}$$

The last term on the right-hand side cannot be simplified further (except for substituting $\mathbb{U} = \mathbb{T}_1$), the first term is further decomposed by using eq. (4.43), leading to the final expression

$$\mathbb{U}^3 = \underline{\mathbb{T}_2\mathbb{U}} + \mathbb{\Sigma}_2\mathbb{T}_1 = \mathbb{\Sigma}_3 + \mathbb{T}_3 + \mathbb{\Sigma}_2\mathbb{T}_1. \tag{4.47}$$

Recall from eq. (4.40) that $\mathbb{\Sigma}_1 = 0$, which reduces the number of terms here and in the following significantly. For the fourth order, we merely sketch the decomposition,

$$\mathbb{U}^4 = \underline{\mathbb{U}^3}\,\mathbb{U} = \mathbb{\Sigma}_2\,\underline{\mathbb{T}_1\mathbb{U}} + \mathbb{\Sigma}_3\mathbb{U} + \mathbb{\Sigma}_4 + \mathbb{T}_4 = \mathbb{\Sigma}_4 + \mathbb{\Sigma}_2^2 + \mathbb{\Sigma}_3\mathbb{T}_1 + \mathbb{\Sigma}_2\mathbb{T}_2 + \mathbb{T}_4. \tag{4.48}$$

We give the fifth-order result without showing substeps,

$$\mathbb{U}^5 = \mathbb{\Sigma}_5 + \mathbb{\Sigma}_2\mathbb{\Sigma}_3 + \mathbb{\Sigma}_3\mathbb{\Sigma}_2 + \left(\mathbb{\Sigma}_4 + \mathbb{\Sigma}_2^2\right)\mathbb{T}_1 + \mathbb{\Sigma}_3\mathbb{T}_2 + \mathbb{\Sigma}_2\mathbb{T}_3 + \mathbb{T}_5. \tag{4.49}$$

Inspection of eqs. (4.47) to (4.49) indicates a systematic structure underlying the expressions, namely

$$\mathbb{U}^j = \sum_{k=0}^{j} \varpi_{j-k}\mathbb{T}_k. \tag{4.50}$$

Each term in this sum has one factor of $\mathbb{T}_k$ of order $0 \leq k \leq j$ and a prefactor ϖ_{j-k} consisting of all possible combinations of $\mathbb{\Sigma}$-superoperators of total order $j - k$. A formal proof of this is given in appendix A.5. Using the decomposition (4.50) and regrouping terms according to each occurrence of $\mathbb{T}_j$, we can now rewrite the perturbation series for

the steady state in the form

$$|\rho_s) = \sum_{j=0}^{\infty}\sum_{k=0}^{j} \varpi_{j-k}\mathbb{T}_k|\rho_s^{(0)}) = \mathbb{f}\sum_{j=0}^{\infty}\mathbb{T}_j|\rho_s^{(0)}). \tag{4.51}$$

Here, the superoperator $\mathbb{f} = \mathbb{f}(\mathbb{\Sigma}_1, \mathbb{\Sigma}_2, \cdots) = \sum_{n=0}^{\infty}\varpi_n$ implements the resummation of terms that we have been aiming for. It is given by

$$\mathbb{f} = \mathbb{1} + \mathbb{\Sigma}_2 + \mathbb{\Sigma}_3 + \mathbb{\Sigma}_4 + \mathbb{\Sigma}_2^2 + \mathbb{\Sigma}_5 + \mathbb{\Sigma}_2\mathbb{\Sigma}_3 + \mathbb{\Sigma}_3\mathbb{\Sigma}_2 \cdots , \tag{4.52}$$

i.e., the sum of all possible products of $\mathbb{\Sigma}$-superoperators (here explicitly shown up to fifth order). Diagrammatically, we represent $\mathbb{f}$ in the form shown in fig. 4.5(b). Due to the definitions of $\mathbb{\Sigma}_j$ and $\mathbb{T}_j$ as diagonal and off-diagonal superoperators, $\mathbb{\Sigma}_j$ corresponds to a loop diagram with initial and final state being identical, all $(j-1)$ intermediate states being different from the initial/final state, and consecutive intermediate states being different from each other.

The role of $\mathbb{\Sigma}_j$ resembles that of an irreducible self-energy contribution of order j in closed-system PT. The concrete physical interpretation of $\mathbb{\Sigma}_j$ has to wait until we apply the formalism to a physical system, for example the Jaynes-Cummings lattice model in section 4.5.3. Moreover, if we define $\mathbb{\Sigma} = \sum_{j=1}^{\infty}\mathbb{\Sigma}_j$ as the sum of all irreducible "self-energy" contributions, we can rewrite $\mathbb{f} = \sum_{j=0}^{\infty}\mathbb{\Sigma}^j = (\mathbb{1}-\mathbb{\Sigma})^{-1}$, and obtain

$$|\rho_s) = \sum_{j=0}^{\infty}\frac{1}{\mathbb{1}-\mathbb{\Sigma}}\mathbb{T}_j|\rho_s^{(0)}) \tag{4.53}$$

for our resummed series expansion of the steady state. Due to the $(\mathbb{1}-\mathbb{\Sigma})^{-1}$ prefactor, each term $|\rho_s^{[j]}) = (\mathbb{1}-\mathbb{\Sigma})^{-1}\mathbb{T}_j|\rho_s^{(0)})$ in this sum includes perturbative corrections up to

infinite order. We therefore call the term $|\rho_s^{[j]})$ the rank-j term of the resummed series. We note that, formally, eq. (4.53) is an exact expression for the steady state. Practical calculations will typically involve a truncation in both the maximum summation index j as well as the maximum order of irreducible self-energy contributions taken into account.

We represent individual terms $|\rho_s^{[j]})$ in the resummed series by the type of diagram shown in fig. 4.5(c). The final-state dot is marked with a circle to indicate the inclusion of the self-energy correction. The diagrammatic rules are similar to the case without resummation, fig. 4.5(a), except that the off-diagonal nature of $\mathbb{T}_j$ in addition requires that all intermediate states be different from the final state. This is simple to infer from writing $\mathbb{T}_j$ in the form of eq. (4.44). Each diagram then translates to an expression with the following structure:

$$|\rho_s^{[j]}) = \sum_{\mu_j} \sum_{\nu_1,\ldots,\nu_{j-1}\neq\mu_j} |\mathsf{u}_{\mu_j}^{(0)}) \left(\frac{1}{\mathbb{1}-\mathbb{\Sigma}}\right)_{\mu_j\mu_j} (\mathbb{U})_{\mu_j\nu_{j-1}} (\mathbb{U})_{\nu_{j-1}\nu_{j-2}} \cdots (\mathbb{U})_{\nu_2\nu_1} (\mathbb{U})_{\nu_1 0} \,. \tag{4.54}$$

4.5. Application to the open Jaynes-Cummings lattice

Lindblad perturbation theory and resummation as discussed in the previous section are applicable to a large class of open quantum systems. Here, we present its concrete use in studying the open Jaynes-Cummings lattice as a specific example of an open driven quantum lattice. The example is of particular interest due to its role as a minimal model for experiments with circuit-QED lattices [25, 52].

We shall consider a uniform Jaynes-Cummings lattice, in which resonator frequencies, qubit frequencies, and related quantities have uniform values across the lattice. (Disorder levels, especially in qubit frequencies, may need to be considered carefully for detailed

modeling of concrete circuit-QED experiments, but this consideration is beyond the scope of the discussion here.) The Hamiltonian is given by (see section 2.5.2)

(4.55)
$$\mathsf{H} = \sum_{\mathbf{r}} \left[\delta\omega \mathsf{a}_{\mathbf{r}}^{\dagger}\mathsf{a}_{\mathbf{r}} + \delta\Omega\sigma_{\mathbf{r}}^{+}\sigma_{\mathbf{r}}^{-} + g\left(\mathsf{a}_{\mathbf{r}}\sigma_{\mathbf{r}}^{+} + \mathsf{a}_{\mathbf{r}}^{\dagger}\sigma_{\mathbf{r}}^{-}\right) + \epsilon\left(\mathsf{a}_{\mathbf{r}} + \mathsf{a}_{\mathbf{r}}^{\dagger}\right)\right] + \sum_{\mathbf{r}\mathbf{r}'} \kappa_{\mathbf{r}\mathbf{r}'}(\mathsf{a}_{\mathbf{r}}^{\dagger}\mathsf{a}_{\mathbf{r}'} + \mathsf{a}_{\mathbf{r}}\mathsf{a}_{\mathbf{r}'}^{\dagger}),$$

with g the resonator-qubit coupling strength and ϵ the uniform drive strength. The lattice structure is encoded in the hopping matrix $(\kappa_{\mathbf{r}\mathbf{r}'})$ with uniform hopping rate between nearest-neighbor sites. In the usual way, we have already eliminated the original time dependence of the drive by switching to a frame rotating with the drive frequency. Consequently, the photon and qubit terms involve frequency detunings, $\delta\omega$ and $\delta\Omega$, relative to the drive. Finally, we consider the damping induced by photon decay (rate γ) and qubit relaxation (rate Γ). If both processes occur due to coupling to separate zero-temperature baths, then the appropriate jump operators are the photon annihilation operator $\mathsf{a}_{\mathbf{r}}$ and the pseudo-spin lowering operator $\sigma_{\mathbf{r}}^{-}$ (see sections 3.4 and 3.5). Overall, we thus obtain the Lindblad master equation

(4.56)
$$\dot{\rho} = -i\left[\mathsf{H}, \rho\right] + \sum_{\mathbf{r}} \gamma\, \mathbb{D}\left[\mathsf{a}_{\mathbf{r}}\right]\rho + \sum_{\mathbf{r}} \Gamma\, \mathbb{D}\left[\sigma_{\mathbf{r}}^{-}\right]\rho.$$

4.5.1. Preparatory steps

We find the modes of the photonic lattice structure by diagonalizing the $N \times N$ hopping matrix $(\kappa_{\mathbf{r}\mathbf{r}'})$, N being the number of lattice sites[8]. For periodic lattices, diagonalization is achieved in the usual way by switching from real space to momentum space via the

[8]For an infinite system, $N \gg 1$ is the auxiliary lattice size involved in applying Born-von Karmann periodic boundary conditions.

transformation $\mathsf{a}_{\mathbf{r}} = \sum_{\mathbf{k}} \tilde{\mathsf{a}}_{\mathbf{k}} e^{i\mathbf{k}\cdot\mathbf{r}}/\sqrt{N}$. Here, photons inside the mode with quasi-momentum $\mathbf{k}$ are annihilated by $\tilde{\mathsf{a}}_{\mathbf{k}}$, and $\mathbf{k}$ runs over all reciprocal lattice vectors from the first Brillouin zone. Note that $\mathbf{k} = \mathbf{0}$ corresponds to the uniform mode with identical amplitudes on all sites, which is the mode being excited by a global coherent drive.

Depending on the values of model parameters, it is beneficial to perform a displacement transformation which eliminates the coherent drive on the photon mode and converts it into an effective qubit drive instead. This is particularly helpful when the uniform photon mode is approximately in a coherent state with a large number of photons. The coherent displacement then serves as a tool incorporating this insight directly into the unperturbed Liouville superoperator and mitigates the need for large photon number cutoffs. (In a regime of low photon occupation, however, the displacement transformation can be skipped and the perturbative treatment carried out directly.) The displacement is applied to the $\mathbf{k} = \mathbf{0}$ mode, i.e., $\mathsf{b}_{\mathbf{0}} = \tilde{\mathsf{a}}_{\mathbf{0}} - \alpha$, with $\alpha = -\sqrt{N}\epsilon/(\delta\omega_{\mathbf{k}=\mathbf{0}} - i\gamma/2)$.

After this displacement, the resonator drive is converted into an effective qubit drive of strength $\epsilon_{\text{eff}} = g\alpha/\sqrt{N}$. The resulting Hamiltonian has the form

$$\mathsf{H}' = \sum_{\mathbf{k}} \mathsf{H}_r^{\mathbf{k}} + \sum_{\mathbf{r}} \mathsf{H}_q^{\mathbf{r}} + \sum_{\mathbf{k},\mathbf{r}} \mathsf{H}_{rq}^{\mathbf{kr}}, \tag{4.57}$$

where the three terms correspond to the photon, qubit, and photon-qubit coupling contributions. The resonator part now lacks the drive term, $\mathsf{H}_r^{\mathbf{k}} = \delta\omega_{\mathbf{k}} \mathsf{b}_{\mathbf{k}}^\dagger \mathsf{b}_{\mathbf{k}}$. (We define $\mathsf{b}_{\mathbf{k}} = \tilde{\mathsf{a}}_{\mathbf{k}}$ for $\mathbf{k} \neq \mathbf{0}$ to unify notation.) The qubit Hamiltonian including the effective drive reads

$$\mathsf{H}_q^{\mathbf{r}} = \delta\Omega\, \sigma_{\mathbf{r}}^+ \sigma_{\mathbf{r}}^- + (\epsilon_{\text{eff}} \sigma_{\mathbf{r}}^+ + \epsilon_{\text{eff}}^* \sigma_{\mathbf{r}}^-), \tag{4.58}$$

and the interaction Hamiltonian is given by

$$\mathsf{H}_{rq}^{\mathbf{kr}} = \frac{g}{\sqrt{N}} \left(\mathsf{b}_{\mathbf{k}} \sigma_{\mathbf{r}}^{+} e^{i\mathbf{k}\cdot\mathbf{r}} + \mathsf{b}_{\mathbf{k}}^{\dagger} \sigma_{\mathbf{r}}^{-} e^{-i\mathbf{k}\cdot\mathbf{r}} \right). \tag{4.59}$$

Finally, the dissipator term simply transforms as $\gamma \sum_{\mathbf{r}} \mathbb{D}\left[\tilde{\mathsf{a}}_{\mathbf{r}}\right] = \gamma \sum_{\mathbf{k}} \mathbb{D}\left[\mathsf{b}_{\mathbf{k}}\right]$.

In the absence of the interaction $\mathsf{H}_{rq}^{\mathbf{kr}}$, resonator modes and qubits decouple, and the associated master equation is exactly solvable. This presents us with an ideal starting point for a perturbative treatment of $\mathsf{H}_{rq}^{\mathbf{kr}}$, which physically is a very sensible treatment of the dispersive regime. The unperturbed Liouville superoperator is then $\mathbb{L}_0 = \sum_{\mathbf{k}} \mathbb{L}_r^{\mathbf{k}} + \sum_{\mathbf{r}} \mathbb{L}_q^{\mathbf{r}}$ with separate photon contribution, $\mathbb{L}_r^{\mathbf{k}} \bullet = -i \left[\mathsf{H}_r^{\mathbf{k}}, \bullet\right] + \gamma \mathbb{D}\left[\mathsf{b}_{\mathbf{k}}\right] \bullet$, and qubit contribution, $\mathbb{L}_q^{\mathbf{r}} \bullet \equiv -i \left[\mathsf{H}_q^{\mathbf{r}}, \bullet\right] + \Gamma\, \mathbb{D}\left[\sigma_{\mathbf{r}}^{-}\right] \bullet$.

4.5.2. Exact solution for the unperturbed lattice problem

We can diagonalize the photonic part $\sum_{\mathbf{k}} \mathbb{L}_r^{\mathbf{k}}$ analytically by using the third-quantization method discussed in section 3.4. This method employs the superoperators $\mathbb{b}_{\mathbf{k}}$, $\mathbb{b}_{\mathbf{k}}^{\ddagger}$, $\beth_{\mathbf{k}}$, $\beth_{\mathbf{k}}^{\ddagger}$, which mimic boson annihilation and creation operators and are defined by eq. (3.28):

$$\mathbb{b}_{\mathbf{k}} \rho = \mathsf{b}_{\mathbf{k}} \rho \qquad \text{and} \qquad \mathbb{b}_{\mathbf{k}}^{\ddagger} \rho = \mathsf{b}_{\mathbf{k}}^{\dagger} \rho - \rho \mathsf{b}_{\mathbf{k}}^{\dagger}, \tag{4.60}$$

$$\beth_{\mathbf{k}} \rho = \rho \mathsf{b}_{\mathbf{k}}^{\dagger} \qquad \text{and} \qquad \beth_{\mathbf{k}}^{\ddagger} \rho = \rho \mathsf{b}_{\mathbf{k}} - \mathsf{b}_{\mathbf{k}} \rho. \tag{4.61}$$

Recall that while $\mathbb{b}_{\mathbf{r}}^{\ddagger}$ and $\mathbb{b}_{\mathbf{r}}$ are not proper adjoints, the use of the unconventional "$\ddagger$" symbol is motivated by the fact that it leads to commutation relations of the ordinary

form,

$$[\mathbb{b}_{\mathbf{k}}, \mathbb{b}^{\ddagger}_{\mathbf{k}'}] = [\beta\!\!\!^{-}_{\mathbf{k}}, \beta\!\!\!^{-\ddagger}_{\mathbf{k}'}] = \delta_{\mathbf{k}\mathbf{k}'}, \tag{4.62}$$

and all other commutators vanish. Thanks to this commutator algebra, $\mathbb{L}_r^{\mathbf{k}}$ takes on the compact form [87],

$$\mathbb{L}_r^{\mathbf{k}} = \theta_{\mathbf{k}} \mathbb{b}^{\ddagger}_{\mathbf{k}} \mathbb{b}_{\mathbf{k}} + \theta^*_{\mathbf{k}} \beta\!\!\!^{-\ddagger}_{\mathbf{k}} \beta\!\!\!^{-}_{\mathbf{k}}. \tag{4.63}$$

Here, $\mathbb{b}_{\mathbf{k}}$ ($\mathbb{b}^{\ddagger}_{\mathbf{k}}$) and $\beta\!\!\!^{-}_{\mathbf{k}}$ ($\beta\!\!\!^{-\ddagger}_{\mathbf{k}}$) may be viewed as "normal-mode" superoperators with complex-valued "mode frequencies" $\theta_{\mathbf{k}} = -i\,\delta\omega_{\mathbf{k}} - \gamma/2$.

As explained in section 3.4, it is straightforward to read off eigenvalues and eigenstates of $\mathbb{L}_r^{\mathbf{k}}$, analogous to the way one finds eigenvalues and eigenstates of a non-interacting boson Hamiltonian. For a given $\mathbf{k}$-mode, the right and left "vacuum states" obey $\mathbb{b}_{\mathbf{k}}|\mathsf{r}^{\mathbf{k}}_{00}) = \beta\!\!\!^{-}_{\mathbf{k}}|\mathsf{r}^{\mathbf{k}}_{00}) = 0$ and $(\check{\mathsf{r}}^{\mathbf{k}}_{00}|\mathbb{b}^{\ddagger}_{\mathbf{k}} = (\check{\mathsf{r}}^{\mathbf{k}}_{00}|\beta\!\!\!^{-\ddagger}_{\mathbf{k}} = 0$. The right "vacuum state" is therefore the projector $|\mathsf{r}^{\mathbf{k}}_{00}) = |0_{\mathbf{k}}\rangle\langle 0_{\mathbf{k}}|$ onto the pure state without any photons in mode $\mathbf{k}$. One can show that the left "vacuum states" must always coincide with the identity operator, $(\check{\mathsf{r}}^{\mathbf{k}}_{00}| = \mathsf{1}$.

The "excited" eigenstates of $\mathbb{L}_r^{\mathbf{k}}$ are obtained by acting with the creation superoperators on the "vacuum states." For given $\mathbf{k}$, this means

$$\left|\mathsf{r}^{\mathbf{k}}_{mn}\right) = \frac{1}{\sqrt{m!n!}} \left(\mathbb{b}^{\ddagger}_{\mathbf{k}}\right)^m \left(\beta\!\!\!^{-\ddagger}_{\mathbf{k}}\right)^n \left|\mathsf{r}^{\mathbf{k}}_{00}\right) , \tag{4.64}$$

and

$$\left(\check{\mathsf{r}}^{\mathbf{k}}_{mn}\right| = \frac{1}{\sqrt{m!n!}} \left(\check{\mathsf{r}}^{\mathbf{k}}_{00}\right| \left(\mathbb{b}_{\mathbf{k}}\right)^m \left(\beta\!\!\!^{-}_{\mathbf{k}}\right)^n . \tag{4.65}$$

The corresponding eigenvalues are $\lambda^{\mathbf{k}}_{mn} = m\theta_{\mathbf{k}} + n\theta^*_{\mathbf{k}}$ $(m, n = 0, 1, \ldots)$. When forming the appropriate product states and summing eigenvalues over $\mathbf{k}$, we thus obtain the entire spectrum of the photonic part $\sum_{\mathbf{k}} \mathbb{L}^{\mathbf{k}}_r$.

Moreover, the qubit Liouvillian $\sum_{\mathbf{r}} \mathbb{L}^{\mathbf{r}}_q$ can be diagonalized exactly since it decomposes into a direct product of 4×4 matrices. For each $\mathbb{L}^{\mathbf{r}}_q$, we denote the eigenvalues, and right/left eigenstates by $\ell^{\mathbf{r}}_\mu$, $|\mathsf{q}^{\mathbf{r}}_\mu)$ and $(\breve{\mathsf{q}}^{\mathbf{r}}_\mu|$, respectively $(\mu = 0, \ldots, 3)$. Except for special parameters, analytical expressions for these quantities are too lengthy to provide much insight, and will hence not be recorded here.

Altogether, right and left eigenstates of the full-lattice Liouvillian $\mathbb{L}_0$ thus take the form

$$|\mathsf{u}^{(0)}_{\vec{m}\vec{n}\vec{\mu}}) = \bigotimes_{\mathbf{k}} |\mathsf{r}^{\mathbf{k}}_{m_{\mathbf{k}} n_{\mathbf{k}}}) \bigotimes_{\mathbf{r}} |\mathsf{q}^{\mathbf{r}}_{\mu_{\mathbf{r}}}), \tag{4.66}$$

with corresponding eigenvalues

$$\lambda^{(0)}_{\vec{m}\vec{n}\vec{\mu}} = \sum_{\mathbf{k}} \lambda^{\mathbf{k}}_{m_{\mathbf{k}} n_{\mathbf{k}}} + \sum_{\mathbf{r}} \ell^{\mathbf{r}}_{\mu_{\mathbf{r}}}. \tag{4.67}$$

The multi-indices $\vec{m}$, $\vec{n}$, and $\vec{\mu}$ collect the sets of all "quantum numbers" $m_{\mathbf{k}}$, $n_{\mathbf{k}}$ and $\mu_{\mathbf{r}}$. With this, we are ready for the perturbative treatment of the Liouvillian $\mathbb{L}_1$ capturing the Jaynes-Cummings interaction $\mathsf{H}^{\mathbf{kr}}_{rq}$.

4.5.3. Perturbative treatment and resummation

The perturbation superoperator decomposes into a sum $\mathbb{L}_1 = \sum_{\mathbf{k},\mathbf{r}} \mathbb{L}^{\mathbf{kr}}_1$, in which each term describes the interaction between an individual resonator mode $\mathbf{k}$ and a qubit at position

$\mathbf{r}$:

$$\mathbb{L}_1^{\mathbf{kr}} \bullet = -i\frac{g}{\sqrt{N}}\left[\mathsf{b}_{\mathbf{k}}\sigma_{\mathbf{r}}^{+}e^{i\mathbf{k}\cdot\mathbf{r}} + \mathsf{b}_{\mathbf{k}}^{\dagger}\sigma_{\mathbf{r}}^{-}e^{-i\mathbf{k}\cdot\mathbf{r}}, \bullet\right]. \tag{4.68}$$

It is therefore convenient to write the $\mathbb{U}$-superoperator (see section 4.4) as an analogous sum, i.e., $\mathbb{U} = \sum_{\mathbf{k},\mathbf{r}} \mathbb{U}^{\mathbf{kr}}$ with $\mathbb{U}^{\mathbf{kr}} = -\mathbb{L}_0^{-1}\mathbb{L}_1^{\mathbf{kr}}$. Each $\mathbb{U}^{\mathbf{kr}}$ is off-diagonal with respect to the unperturbed basis, so that $\mathbb{U}^{\mathbf{kr}} = [\![\mathbb{U}^{\mathbf{kr}}]\!] = \mathbb{T}_1^{\mathbf{kr}}$ holds.

The rank-1 term in the resummation [eq. (4.53)] is given by

$$\left|\rho_s^{[1]}\right) = \frac{1}{\mathbb{1}-\mathbb{\Sigma}}\sum_{\mathbf{k},\mathbf{r}} \mathbb{U}^{\mathbf{kr}}\left|\rho_s^{(0)}\right) = \sum_{\mathbf{k},\mathbf{r}}\sum_{\vec{s}} \frac{1}{\mathbb{1}-\mathbb{\Sigma}}\left|\rho_{\mathbf{kr}\vec{s}}^{[1]}\right)\left(\breve{\rho}_{\mathbf{kr}\vec{s}}^{[1]}\right|\mathbb{U}^{\mathbf{kr}}\left|\rho_s^{(0)}\right). \tag{4.69}$$

Here, the cluster $|\rho_{\mathbf{kr}\vec{s}}^{[1]}) = |\mathsf{r}_{mn}^{\mathbf{k}}\mathsf{q}_{\mu}^{\mathbf{r}}) \bigotimes_{\mathbf{k}'\neq\mathbf{k}} |\mathsf{r}_{00}^{\mathbf{k}'}) \bigotimes_{\mathbf{r}'\neq\mathbf{r}} |\mathsf{q}_0^{\mathbf{r}'})$ involves photon mode $\mathbf{k}$ and qubit at position $\mathbf{r}$ in state $\vec{s} = (m, n, \mu)$. In a similar manner, we see that the rank-2 term

$$\begin{aligned}\left|\rho_s^{[2]}\right) &= \frac{1}{\mathbb{1}-\mathbb{\Sigma}}\sum_{\mathbf{k},\mathbf{k}',\mathbf{r},\mathbf{r}'} [\![[\![\mathbb{U}^{\mathbf{kr}}]\!]\mathbb{U}^{\mathbf{k}'\mathbf{r}'}]\!]\left|\rho_s^{(0)}\right) \\ &= \sum_{\mathbf{k},\mathbf{k}',\mathbf{r},\mathbf{r}'}\sum_{[\vec{s}\vec{s}']} \frac{1}{\mathbb{1}-\mathbb{\Sigma}}\left|\rho_{\mathbf{kr}\vec{s};\mathbf{k}'\mathbf{r}'\vec{s}'}^{[2]}\right)\left(\breve{\rho}_{\mathbf{kr}\vec{s};\mathbf{k}'\mathbf{r}'\vec{s}'}^{[2]}\right|\mathbb{U}^{\mathbf{kr}}\left|\rho_{\mathbf{k}'\mathbf{r}'\vec{s}'}^{[1]}\right)\left(\breve{\rho}_{\mathbf{k}'\mathbf{r}'\vec{s}'}^{[1]}\right|\mathbb{U}^{\mathbf{k}'\mathbf{r}'}\left|\rho_s^{(0)}\right)\end{aligned} \tag{4.70}$$

incorporates the resummation of a cluster $|\rho_{\mathbf{kr}\vec{s},\mathbf{k}'\mathbf{r}'\vec{s}'}^{[2]})$ composed of two photon modes and two qubits in states $\vec{s}$ and $\vec{s}'$. (The bracket notation in the corresponding summation signals that the allowed choices of these states is dictated by the off-diagonal requirement in $\mathbb{T}_2 = [\![[\![\mathbb{U}^{\mathbf{kr}}]\!]\mathbb{U}^{\mathbf{k}'\mathbf{r}'}]\!]$.) In the definition of $|\rho_{\mathbf{kr}\vec{s},\mathbf{k}'\mathbf{r}'\vec{s}'}^{[2]})$, several cases must be distinguished according to whether $\mathbf{k} = \mathbf{k}'$ and/or $\mathbf{r} = \mathbf{r}'$. For the case where both pairs are distinct, we have

$$|\rho_{\mathbf{kr}\vec{s},\mathbf{k}'\mathbf{r}'\vec{s}'}^{[2]}) = |\mathsf{r}_{mn}^{\mathbf{k}}\mathsf{r}_{m'n'}^{\mathbf{k}'}\mathsf{q}_{\mu}^{\mathbf{r}}\mathsf{q}_{\mu'}^{\mathbf{r}'}) \bigotimes_{\mathbf{k}''\neq\mathbf{k},\mathbf{k}'} |\mathsf{r}_{00}^{\mathbf{k}''}) \bigotimes_{\mathbf{r}''\neq\mathbf{r},\mathbf{r}'} |\mathsf{q}_0^{\mathbf{r}''}).$$

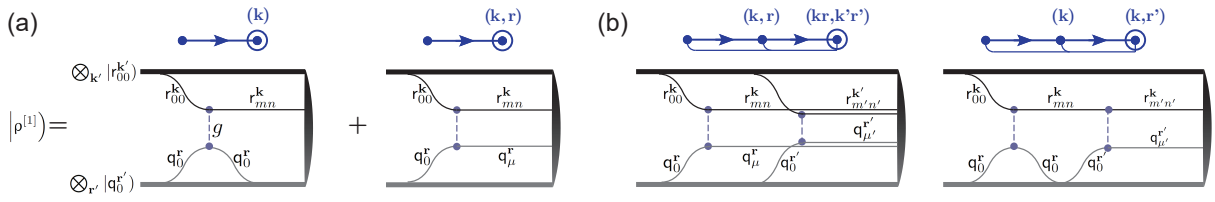

Figure 4.6. **Diagrams for perturbative treatment and resummation of a Jaynes-Cummings lattice**. In each panel, the top part shows the general diagram labeled by constituents deviating from the steady-state configuration. Bottom parts are JC-lattice specific diagrams, with the upper branch denoting photon modes and the lower one qubit degrees of freedom. (a) Rank-1 corrections. There are two classes of terms with either a photon mode or a cluster of a photon mode $\mathbf{k}$ and a qubit at site $\mathbf{r}$ deviating from the unperturbed steady-state configuration. Each interaction vertex g must switch the photon mode configuration, but may leave that of the qubit unchanged. Terminating symbols on the right signal application of the resummation superoperator $(\mathbb{1} - \mathbb{\Sigma})^{-1}$. (b) Two examples of rank-2 corrections, which differ in the number of involved photon modes and qubits, and number of constituents deviating from the steady-state configuration.

Analogous definitions hold in the other three cases.

By inspection of eqs. (4.69) and (4.70) we expect that, in general, the rank-j correction consists of a sum over all possible terms in which clusters of j photon modes and j qubits deviate from the unperturbed density matrix. Thanks to resummation, interaction within each cluster includes terms up to infinite order. We note that this cluster structure directly implies a hierarchy of correlations with increasing rank j. Specifically, every n-point correlation function with p photon and q qubit operators, $\langle \mathsf{b}^{(\dagger)}_{\mathbf{k}_1} \cdots \mathsf{b}^{(\dagger)}_{\mathbf{k}_p} \sigma^{a_1}_{\mathbf{r}_1} \cdots \sigma^{a_q}_{\mathbf{r}_q} \rangle_{\mathrm{ss}}$, does not trivially separate into a product of correlators if the rank j of the correction satisfies $j \geq \max\{p, q\}$. We also emphasize that clusters automatically include long-range correlations between distant qubits.

The essential tasks of determining the perturbative corrections and resummation consist of evaluating matrix elements of the form given in eqs. (4.69) and (4.70), and computing

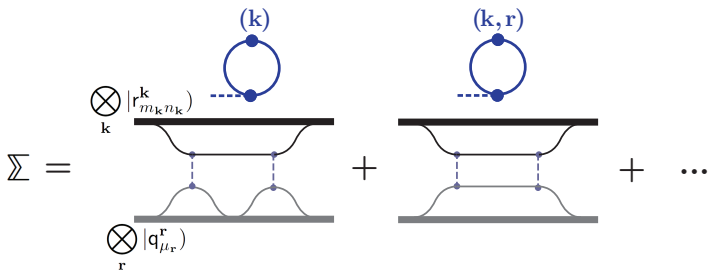

Figure 4.7. **Evaluation of the $\mathbb{\Sigma}$-superoperator**. $\mathbb{\Sigma}$ is needed for resummation and composed of irreducible diagrams starting end terminating in the same state. The two diagrams show the leading-order contributions, $\mathbb{\Sigma}_2$.

the effect of the resummation superoperator $\mathbb{\Sigma}$ to a given order. We illustrate the procedure for the example of rank-1 corrections. Plugging in the definition of $\mathbb{U}^{\mathbf{kr}}$ and recalling that $\mathbb{L}_0$ is diagonal with respect to the unperturbed basis states, we obtain

$$\left(\breve{\rho}^{[1]}_{\mathbf{kr}\vec{s}}\middle|\mathbb{U}^{\mathbf{kr}}\middle|\mathsf{r}^{\mathbf{k}}_{00}\mathsf{q}^{\mathbf{r}}_{0}\right) = -\left(\breve{\mathsf{r}}^{\mathbf{k}}_{mn}\breve{\mathsf{q}}^{\mathbf{r}}_{\mu}\middle|\mathbb{L}_1^{\mathbf{kr}}\middle|\mathsf{r}^{\mathbf{k}}_{00}\mathsf{q}^{\mathbf{r}}_{0}\right)/\lambda_{\mathbf{kr}\vec{s}} = i\mathrm{Tr}(\breve{\mathsf{r}}^{\mathbf{k}\dagger}_{mn}\breve{\mathsf{q}}^{\mathbf{r}\dagger}_{\mu}\,[\mathsf{H}^{\mathbf{kr}}_{rq},\mathsf{r}^{\mathbf{k}}_{00}\mathsf{q}^{\mathbf{r}}_{0}])/\lambda_{\mathbf{kr}\vec{s}} \tag{4.71}$$

where $\lambda_{\mathbf{kr}\vec{s}} = \lambda^{\mathbf{k}}_{mn} + \ell^{\mathbf{r}}_{\mu}$. Once the commutator is opened, it is useful to note that the simple properties of the $\mathbb{L}_r$-eigenstates lead to vanishing overlaps $\mathrm{Tr}(\breve{\mathsf{r}}^{\mathbf{k}\dagger}_{mn}\mathsf{b}^{(\dagger)}_{\mathbf{k}}\mathsf{r}^{\mathbf{k}}_{mn}) = \mathrm{Tr}(\breve{\mathsf{r}}^{\mathbf{k}\dagger}_{mn}\mathsf{r}^{\mathbf{k}}_{mn}\mathsf{b}^{(\dagger)}_{\mathbf{k}}) = 0$, so that any application of $\mathbb{U}^{\mathbf{kr}}$ must switch to a different resonator-mode eigenstate. The same does not hold for traces of the qubit degrees of freedom, i.e., the overlaps $\mathrm{Tr}(\breve{\mathsf{q}}^{\mathbf{k}\dagger}_{\mu}\sigma^{+}_{\mathbf{r}}\mathsf{q}^{\mathbf{k}}_{\mu})$ etc. may indeed be non-zero. As a result, we obtain the two types of terms for the rank-1 correction which are diagrammatically depicted in fig. 4.6(a). The evaluation of rank-2 corrections follows the same basic scheme. Unsurprisingly, it is more tedious and we only show two examples of corresponding diagrams in fig. 4.6(b).

The effect of the resummation superoperator is to redistribute weights among cluster contributions. Since $\mathbb{\Sigma}$ is diagonal with respect to unperturbed Liouvillian eigenstates, we can cast its contribution to a particular form $\mathbb{\Sigma}|\mathsf{u}^{(0)}_{\vec{s}}) = |\mathsf{u}^{(0)}_{\vec{s}})(\breve{\mathsf{u}}^{(0)}_{\vec{s}}|\mathbb{\Sigma}|\mathsf{u}^{(0)}_{\vec{s}})$ and evaluate

the occurring matrix element as follows. We choose an appropriate truncation for the series $\mathbb{\Sigma} = \mathbb{\Sigma}_2 + \mathbb{\Sigma}_3 + \cdots$ of irreducible resummation operators $(\mathbb{\Sigma}_j)_{\vec{s}\vec{s}'} = \delta_{\vec{s}\vec{s}'}(\mathbb{T}_{j-1}\mathbb{U})_{\vec{s}\vec{s}'}$. Figure 4.7 shows the resulting two diagrams for $\mathbb{\Sigma}_2$. Physically, these diagrams and their resummation capture the fact that the coupling between resonator modes and qubits alters the frequencies and lifetimes of Liouvillian eigenstates. Specifically, the resummation accounts for virtual processes in which excitations are repeatedly created, exchanged between qubits and resonator modes, and annihilated. The first diagram in fig. 4.7, for instance, describes the creation of a qubit excitation, its swapping into a resonator mode and back into a qubit, and final annihilation. (The analogous reverse process where a missing excitation is swapped back and forth is included in this diagram as well.) The second diagram differs from the former by the altered qubit state in the virtual intermediate state. These second-order diagrams involve at most one excitation at a time; higher-order virtual processes allow more excitations. We emphasize that the physical interpretation is based on eigenstates of the Liouvillian, rather than states in Hilbert space.

The above calculation of perturbative corrections and resummation may be simplified if we are merely interested in steady-state expectation values (rather than in the density matrix itself). As an example, consider computing an expectation value of a local qubit operator $\sigma^a_{\mathbf{r}}$ up to corrections of rank j, $\langle\sigma^a_{\mathbf{r}}\rangle \approx \sum_{j'=0}^{j} \mathrm{Tr}(\sigma^a_{\mathbf{r}}\rho_s^{[j']})$. To effect the desired simplification, we recall that all eigenstates of $\mathbb{L}_r^{\mathbf{k}}$ and $\mathbb{L}_q^{\mathbf{r}}$ other than the steady state must be traceless[9], i.e., $\mathrm{Tr}(\mathsf{q}_\mu^{\mathbf{r}}) = 0$ for $\mu \neq 0$ and $\mathrm{Tr}(\mathsf{r}_{mn}^{\mathbf{k}}) = 0$ for non-zero m or n. Therefore, any perturbative contribution $\sim \mathrm{Tr}(\sigma^a_{\mathbf{r}}\mathsf{u}^{(0)}_{\vec{m}\vec{n}\vec{\mu}})$ in which $\mu_{\mathbf{r}'} \neq 0$ for some $\mathbf{r}' \neq \mathbf{r}$ will immediately vanish since the partial trace over the qubit at position $\mathbf{r}'$ is zero. Similarly, any term

[9]To quickly confirm the tracelessness, refer to the orthonormality condition (4.3) and note that the left eigenstate corresponding to the steady state is the identity, $(\breve{\rho}^{[0]}| = \mathsf{1}$.

with $(m_{\mathbf{k}}, n_{\mathbf{k}}) \neq (0,0)$ for some photon mode $\mathbf{k}$ will vanish. As a result, none of the rank-1 corrections [fig. 4.6(a)] contribute to local qubit expectation values. Only those diagrams that terminate in a state labeled $(\mathbf{r})$ will yield a nonzero contribution to $\langle \sigma^a_{\mathbf{r}} \rangle$. Analogous diagrammatic rules apply for photon-mode operators.

4.5.4. Perturbative results for the near-resonant regime

We now illustrate the validity and improvement achieved by (partial) resummation of the Lindblad perturbation series. For this purpose, we compare perturbative results for finite-size Jaynes-Cummings chains [fig. 4.1(a)] to exact results computed via quantum trajectories methods. Perturbative resummation further allows us to treat periodic chains (or, open chains if desired) of sizes beyond the computational capabilities of exact quantum-trajectory solutions. Finally, we can carry out perturbative resummation even for an infinite system with chain or global-coupling geometry [figs. 4.1(b) and (c)]. This versatility enables us to predict finite-size effects, the approach to the thermodynamic limit, as well as differences according to distinct lattice geometries. (We discuss the quite moderate computational costs of the perturbative treatment in appendix A.6.)

In our treatment, we capture photon mediated qubit-qubit interactions by second-order Lindblad perturbation theory with resummation based on single-loop terms $\mathbb{\Sigma}_2$ (i.e., corrections of rank 2 in the above terminology). The most natural regime for treating the Jaynes-Cummings coupling perturbatively in this way is the dispersive regime where the detuning $\Delta = \min_{\mathbf{k}} |\Omega - \omega_{\mathbf{k}}|$ between qubit and photon-mode frequencies is large compared to their mutual coupling strength g [130]. We have confirmed by exact numerics that the

perturbation theory is indeed reliable in this regime and, over a wide range of parameters, we identify $g^2/\Gamma\Delta$ as the relevant small parameter governing the series expansion.

In the following, we choose to present results from exploring a different parameter regime more directly based on the open-system nature of Jaynes-Cummings lattices. Specifically, we consider the case where photon hopping dominates over both photon decay and Jaynes-Cummings coupling, and where the latter two are permitted to be of the same order, i.e. $\kappa \gg g \sim \gamma$. The strong hopping κ shifts the majority of the photon mode frequencies away from the bare resonator frequency which is chosen degenerate with the qubit frequency, $\Omega = \omega$. This regime is not fully dispersive, so that nonlinearities are more pronounced, and the significance of resummation becomes easily visible. Moreover, the condition $g \sim \gamma$ results in weakly perturbed coherent states for the photon modes over the full range of weak to strong drive strengths, without any particular limitation.

We begin with the comparison between perturbative and exact results for the steady state of few-site Jaynes-Cummings chains with periodic boundary conditions. In our calculations, we have considered several qubit and resonator expectation values. Among those, we find that $|\langle\sigma^-\rangle| = \sqrt{\langle\sigma^x\rangle^2 + \langle\sigma^y\rangle^2}/2$ is a convenient choice for clearly resolving resonances. Representing the reduced steady-state density matrix for one of the qubits by means of the Bloch sphere picture, this quantity is directly proportional to the distance of the Bloch vector from the z axis, see fig. 4.8(a). Computing exact steady-state solutions for Jaynes-Cummings chains even as small as 4 sites, is a non-trivial task which we accomplish by averaging of quantum trajectories. For instance, exact results presented in fig. 4.8 for $N = 4$ were determined from stochastic time evolution of a quantum state vector of size

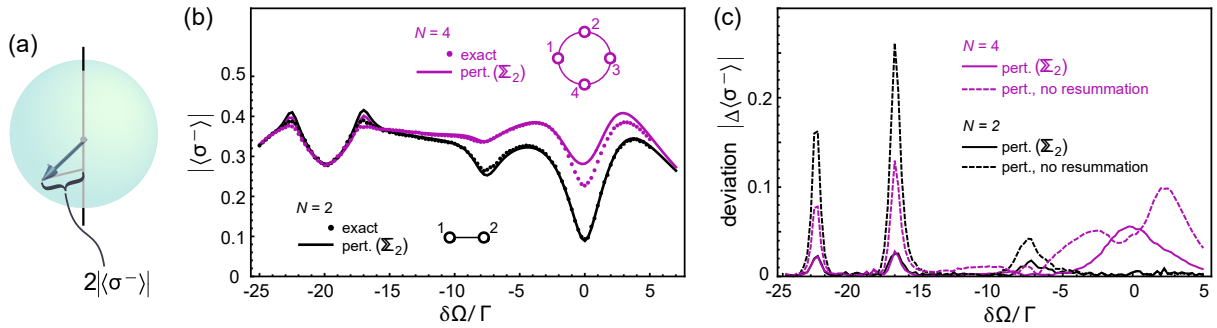

Figure 4.8. **Comparison between perturbative results and exact solution**. (a) Within the Bloch-sphere picture, the steady-state expectation value $|\langle\sigma^-\rangle|$ is directly proportional to the distance of the Bloch vector (representing ρ_s^{qubit}) from the z axis. (b) shows $|\langle\sigma^-\rangle|$ as a function of detuning $\delta\Omega$ between drive and bare qubit frequency, in units of the qubit relaxation rate Γ. Qubits are held in resonance with the bare resonator frequency, $\Omega = \omega$. Exact and perturbative results for chain sizes $N = 2$ and 4 are in good agreement. (See text for explanation of deviations close to $\delta\Omega = 0$ in the $N = 4$ case.) (c) Curves here depict the absolute deviations between exact and perturbative results for calculations with (solid lines) and without resummation (dashed lines). Perturbation theory is not sufficient to describe the region close to $\delta\Omega = 0$ for $N = 4$ (see text). Outside this region, resummation consistently improves agreement with the exact solution. [Parameters: $g/\Gamma = 3$, $\epsilon/\Gamma = 20$, $\kappa/\Gamma = 10$, and $\gamma/\Gamma = 4$.]

10^4. Sufficient averaging of a single data point required a runtime of several days on one core.

The comparison between exact and rank-2 perturbative data (including resummation at the level of $\mathbb{\Sigma}_2$) in fig. 4.8(b) shows very good agreement, and indicates that the resummation procedure closely matches the exact solution. Plots in this figure show the steady-state value of $|\langle\sigma^-\rangle|$ as a function of the detuning $\delta\Omega = \Omega - \omega_d$ between the drive and the bare qubit frequency. Multiple resonances are visible over the chosen frequency range (the nature of which we will further discuss below). The only notable quantitative deviations occur for $N = 4$ in the vicinity of the bare qubit frequency where $\delta\Omega = 0$. This

deviation has a simple explanation: a look ahead at fig. 4.10(b) shows that the 4-site chain has a photon mode with large spectral weight directly on resonance with the bare qubit frequency, so that there we must expect the perturbative treatment in g to break down. With the exception of this finding, we conclude that resummation of the perturbative series in the chosen parameter regime works very well. The improvement gained over the pure second-order approximation is illustrated in fig. 4.8(c). In this panel, curves show the difference between approximate and exact results, $\Delta\langle\sigma^-\rangle = \langle\sigma^-\rangle_{\text{approx}} - \langle\sigma^-\rangle_{\text{exact}}$, for the case including resummation (solid lines) and lacking resummation (dashed lines). Excluding the pathological region for $N = 4$ around $\delta\Omega = 0$, we observe that resummation consistently improves the results, reducing the deviation from the exact solution. The improvement is especially significant in the resonance region between $\delta\Omega/\Gamma \approx -17$ and -23. Here, the drive populates the uniform mode (centered at $\delta\Omega/\Gamma = -20$) and renders photon-mediated qubit-qubit interaction important, making resummation of corrections up to infinite order particularly fruitful.

The improvement gained by including resummation is even more striking for the 3-site chain. In fig. 4.9, the comparison between exact and perturbative result (no resummation) shows three regions with significant deviations. The deviations for $\delta\Omega/\Gamma \approx -24$ and -14 arise from spurious resonance peaks which we can trace back to the poles of the inverse $\mathbb{L}_0^{-1}$ of the unperturbed Liouville superoperator [eq. (4.34)]. Resummation nicely cures these spurious peaks, effectively by shifting away poles of the relevant superoperators. This indicates that including resummation has an effect beyond simply truncating the perturbative series at higher orders. The deviation for $\delta\Omega/\Gamma \approx 1$ is associated with the resonance dip being incorrectly shifted. Resummation improves the prediction of not

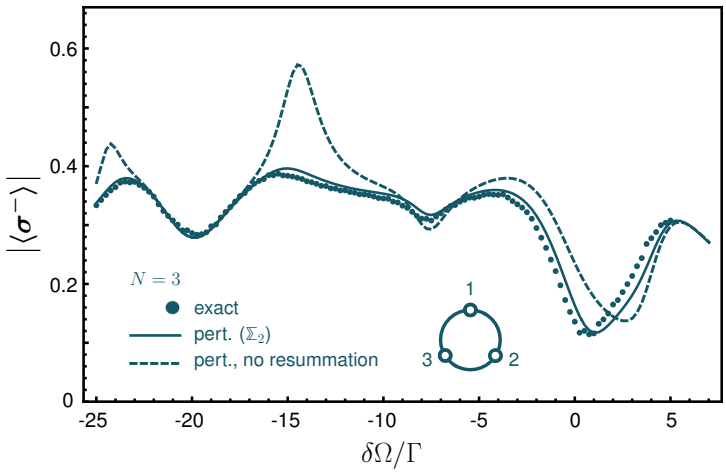

Figure 4.9. **Comparison between perturbative results with resummation (solid line) and without (dashed line) for the 3-site chain**. The result without resummation shows three regions with significant deviations from the exact solution (dots) for $\delta\Omega/\Gamma \approx -24$, -14 and 1. These deviations (spurious and wrongly shifted resonances) are cured by including corrections obtained by resummation. [All system parameters are identical to those in fig. 4.8.]

just the resonance position but also its shape. These resonances contain information on many-body effects due to the coupling between the resonators and qubits. Hence, curing both incorrectly shifted and spurious resonances by including resummation is vital and crucial for verification of experimental data.

We next turn to the discussion of the resonances visible in fig. 4.8 and shown for additional site numbers N in fig. 4.10(a). For small chain lengths up to $N = 5$ sites, we observe three resonances labeled A, B, and C in the range of drive frequencies spanning the photon-chain eigenmodes and qubit frequencies. [The uniform photon mode has the lowest frequency, $\delta\Omega/\Gamma = -20$, and the bare qubit frequency is at $\delta\Omega/\Gamma = 0$, see vertical lines in fig. 4.10(b)]. We find that the detailed positions and strengths of resonances depend on the number of sites, revealing systematic finite-size effects for chains of short lengths.

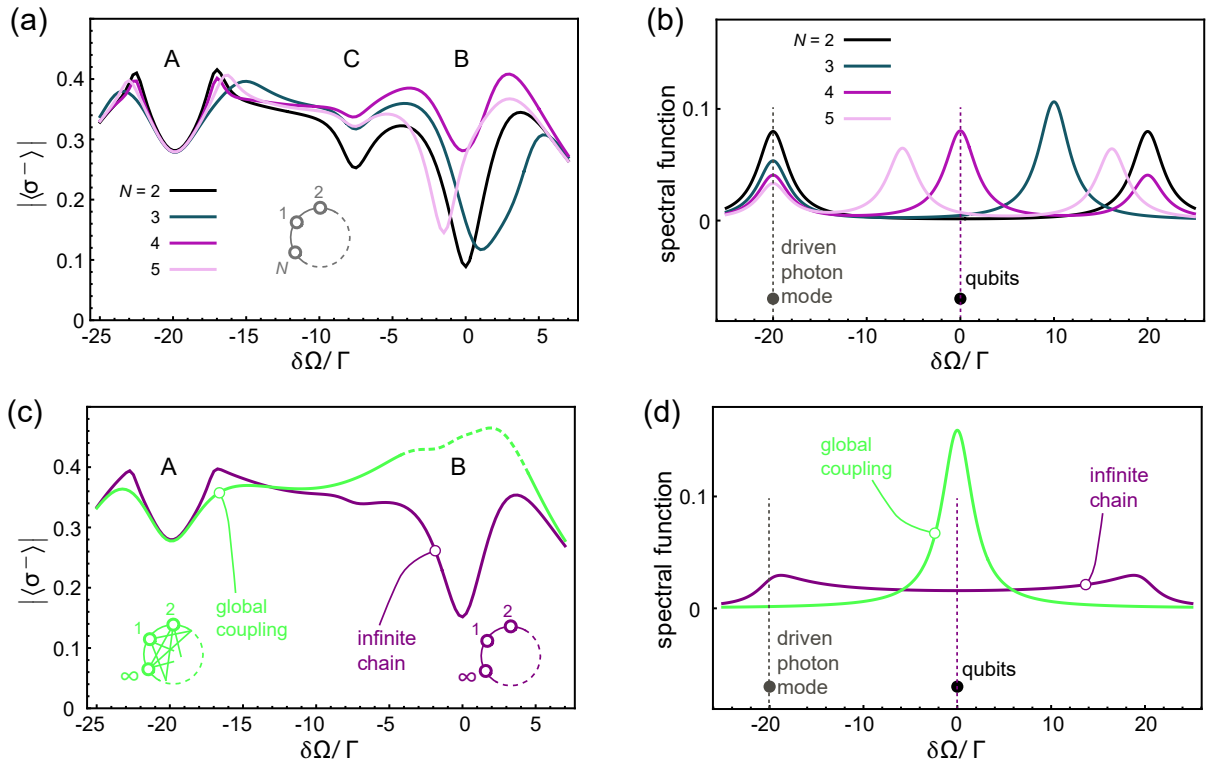

Figure 4.10. **Perturbative results and spectral functions for periodic Jaynes-Cummings chains and global-coupling model**. (a) shows the qubit expectation value $|\langle\sigma^-\rangle|$ for periodic chains with different site numbers N. We observe three resonance dips (labeled A–C). A and B are located roughly at the driven photon mode and qubit frequencies, respectively. (b) Spectral functions resonator modes differ for small site numbers. Presence and position of resonances near the qubit frequency explain the N-dependence of strength and shift of the B resonance. (c,d) show analogous plots for infinite lattices with periodic chain or global-coupling geometry. Resonances A and B are visible, but resonance C is (nearly) absent. [All system parameters are identical to those in fig. 4.8.]

Both the nature and N dependence of resonances can be explained, or at least motivated, by the following considerations.

The resonance marked A directly coincides with the frequency of the uniform photon mode. Equivalent interpretations of the resonance can be given based on the original Hamiltonian eq. (4.55) with a coherent tone driving this particular mode with strength ϵ, or for the

Hamiltonian following the displacement transformation eqs. (4.57) and (4.58). Employing the language of the latter description, we note that the strength $\epsilon_{\text{eff}} = -g\epsilon/(\delta\omega_{\mathbf{k}=\mathbf{0}} - i\gamma/2)$ of the effective qubit drive reaches its local maximum at the uniform-mode frequency ($\delta\Omega/\Gamma = -20$). This peak in the off-resonant Rabi drive, modified by weak coupling to photon modes, is responsible for resonance A. Its dependence on the site number N is relatively weak and mainly affects the shoulders of the resonance. This is further confirmed by our results for the infinite-system case with periodic-chain and global-coupling geometry [fig. 4.10(c)]. Both show the same resonance A, but differ in the resonance shoulders.

For resonance B, the N dependence of resonance position and strength is much more pronounced. The general region where B occurs is close to $\delta\Omega = 0$, i.e., where bare qubit frequency and drive frequency match. Upon displacement, the drive transforms into an effective Rabi drive on each qubit [eq. (4.58)]. Hence, the presence of a resonance is natural, and variations in its strength and precise position must be governed by the Jaynes-Cummings interaction playing the role of the perturbation in our treatment [eq. (4.68)]. The importance of this interaction is influenced by the position of photon-mode resonances $\omega_{\mathbf{k}}$ relative to the bare qubit frequency. In fig. 4.10(b) and (d), we depict width and position of photon modes in terms of the spectral function $s(\omega) = \sum_{\mathbf{k}} \frac{\gamma/2}{(\omega-\omega_{\mathbf{k}})^2+(\gamma/2)^2}$, which is the sum over individual Lorentzians for each photon mode, normalized such that $\int d\omega\, s(\omega) = 1$. Inspection of resonance-B positions [fig. 4.10(a),(c)] and peaks in the spectral function [fig. 4.10(b),(d)] shows that peaks in $s(\omega)$ with significant weight in the region $\Omega \pm g$, shift B resonances towards the closest photon mode (such as for $N = 3, 5$). Further, it is clear that strongly increased weight of the spectral function directly at the qubit frequency (such as for $N = 4$ and for the global-coupling geometry) endangers the validity of perturbation

theory in the Jaynes-Cummings coupling. Above, we recognized this as the reason for the observed deviations between perturbation theory and exact solution close to $\delta\Omega = 0$ in the $N = 4$ case. A look at the spectral function for the global-coupling geometry shows that the same issue occurs here. Accordingly, we show the perturbative result in fig. 4.10(c) only with dashes in that region.

We note that steady-state expectation values for infinite lattices are not always easily accessible by other methods. Thanks to the possibility of carrying out leading-order resummation analytically in the infinite-system case, our treatment gives direct access to the thermodynamic limit of different lattice geometries. Here, we have chosen two extreme cases: the infinite periodic chain with a minimum number of links between sites, and the global-coupling model with a maximum number of links. Figure 4.10(c) depicts results for both lattice structures. We expect that the region close to $\delta\Omega = 0$ is unproblematic for the infinite chain case, but potentially pathological for the global-coupling model which accumulates maximum spectral weight at the bare qubit frequency [fig. 4.10(d)]. Away from the $\delta\Omega = 0$ range, the two geometries yield similar behavior of $|\langle\sigma^-\rangle|$ versus drive detuning $\delta\Omega$. As before, characteristic differences occur primarily in the shoulders of resonance A. Interestingly, the resonance C is absent for both infinite lattices, and we discuss the rather anomalous behavior of this finite-size resonance next.

The anomalous properties of resonance C are illustrated in fig. 4.11. The position of this resonance close to $\delta\Omega/\Gamma \approx 8$ does not simply coincide with a resonance between photon modes and bare qubits. Panel (a) shows the decrease of the resonance strength for increasing chain length N. Moreover, both resonance position and strength depend sensitively on the drive power $\sim \epsilon$ as shown in fig. 4.11 for the dimer case, $N = 2$. We

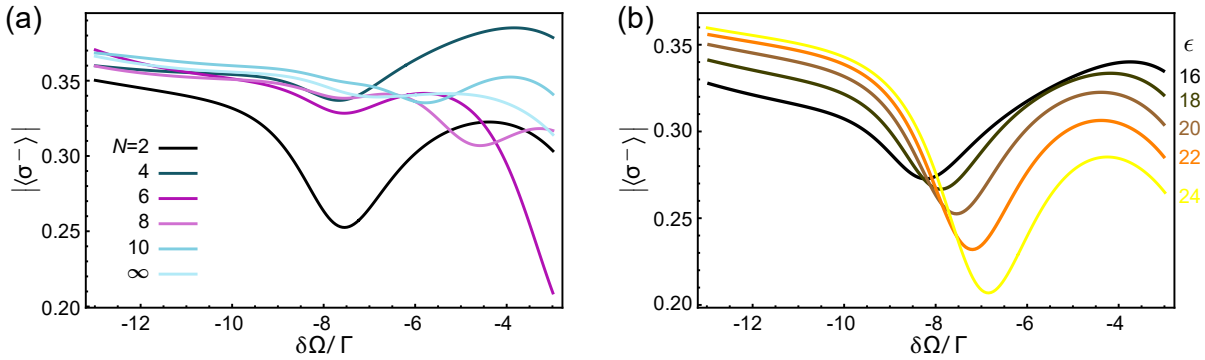

Figure 4.11. **Dependence of the anomalous resonance C on site number N and drive strength ϵ.** (a) The anomalous dip becomes less prominent with increasing N (even) and nearly vanishes for the infinite chain. (The same trend applies to odd site numbers.) (b) For the dimer case, $N = 2$, the position of the anomalous resonance shifts monotonically with increasing drive strength ϵ. The same trend is observed for longer chains. [Parameters are chosen the same as in fig. 4.8.]

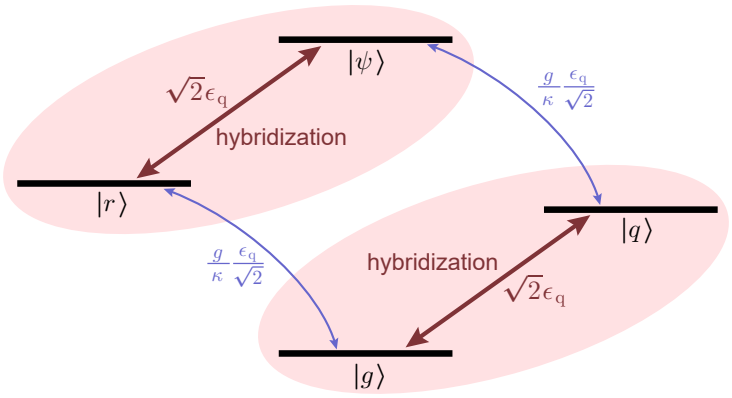

Figure 4.12. **Effective four-level model explaining the anomalous resonance**. The transitions $|g\rangle \leftrightarrow |q\rangle$ and $|r\rangle \leftrightarrow |\psi\rangle$ strongly hybridize two pairs of states. The anomalous resonance results from transitions between the two hybridized doublets. Since the energy separation between hybridized doublets depends on drive strength ϵ, so does the position of the anomalous resonance.

investigate this anomaly for the $N = 2$ case, where a semi-quantitative reduced model can shed light on the origin and nature of this resonance.

For $N = 2$ we can confirm analytically that the anomalous resonance C is closely related to an eigenstate $|\psi\rangle$ of the displaced Hamiltonian H' [eq. (4.57)] without the effective drive. This eigenstate comprises two excitations distributed between the uniform mode and the qubits. Truncation to first order in g/κ (a small quantity for the chosen parameter set) yields

$$|\psi\rangle \approx \frac{1}{\sqrt{2}} |1_{\mathbf{0}}\rangle (|\uparrow\downarrow\rangle + |\downarrow\uparrow\rangle) - \frac{1}{\sqrt{2}} \frac{g}{\kappa} |2_{\mathbf{0}}\rangle |\downarrow\downarrow\rangle + \frac{1}{2} \frac{g}{\kappa} |0_{\mathbf{0}}\rangle |\uparrow\uparrow\rangle \tag{4.72}$$

with eigenenergy $2\Omega + 2\kappa - g^2/2\kappa$. Here, $|n_{\mathbf{0}}\rangle$ is the n-photon state of the uniform mode and $|\uparrow\uparrow\rangle$ etc. denote states of the qubits on the two sites. The effective drive Hamiltonian with strength ϵ_{eff} connects the ground state $|g\rangle = |0_{\mathbf{0}}\rangle |\downarrow\downarrow\rangle$ to the state $|\psi\rangle$ via two intermediate states $|r\rangle$ and $|q\rangle$, see fig. 4.12. These intermediate states belong to the one-excitation manifold and primarily consist either of a photon in the uniform mode or of a qubit excitation, respectively. Truncated again to first order in g/κ, $|r\rangle$ and $|q\rangle$ are given by

$$|r\rangle \approx |1_{\mathbf{0}}\rangle |\downarrow\downarrow\rangle + \frac{1}{2\sqrt{2}} \frac{g}{\kappa} |0_{\mathbf{0}}\rangle (|\uparrow\downarrow\rangle + |\downarrow\uparrow\rangle), \tag{4.73}$$

$$|q\rangle \approx \frac{1}{\sqrt{2}} |0_{\mathbf{0}}\rangle (|\uparrow\downarrow\rangle + |\downarrow\uparrow\rangle) - \frac{1}{2} \frac{g}{\kappa} |1_{\mathbf{0}}\rangle |\downarrow\downarrow\rangle . \tag{4.74}$$

Our description of the anomalous resonance in the following is based on the effective four-level model spanned by the states $|g\rangle$, $|r\rangle$, $|q\rangle$, and $|\psi\rangle$, see fig. 4.12.

Within this model, the effective drive Hamiltonian connects the ground state $|g\rangle$ to the two-excitation state $|\psi\rangle$ via $|r\rangle$ and $|q\rangle$. Since the effective drive creates (or annihilates) qubit excitations only, there is stronger hybridization of $|g\rangle$ with $|q\rangle$ (strength $\sim \epsilon_{\text{eff}}$) than with $|r\rangle$ (strength $\sim \epsilon_{\text{eff}}\, g/\kappa$). An analogous argument applies to explain hybridization of

$|r\rangle$ with $|\psi\rangle$ (again, strength $\sim \epsilon_{\text{eff}}$). We thus obtain the picture of two pairs of hybridized states, $|g\rangle \leftrightarrow |q\rangle$ and $|r\rangle \leftrightarrow |\psi\rangle$, with only small drive matrix elements connecting the pairs.

Due to the energy differences between states within each pair, hybridization is only partial. The two emerging hybridized states relevant to the anomalous resonance have significant overlap with the ground state $|g\rangle$ in one case, and the two-excitation state $|\psi\rangle$ in the other case. The resonance C can be approximately viewed as a resonance between these two hybridized states. Note that the degree of hybridization critically depends on the effective drive strength ϵ_{eff}, which is in turn proportional to the drive strength ϵ. As a consequence, the energy separation between the two relevant hybridized states depends on drive strength as observed in fig. 4.11(b).

The generalization of the effective four-level model to periodic chains with larger number of sites N is difficult due to the proliferation of degeneracies among eigenstates of H' in the absence of a drive. Based on our perturbative calculations, we find a clear trend of diminishing resonance strength with increasing number of sites [fig. 4.11(a)]. The anomalous resonance C hence provides an interesting example of an interaction-induced feature which is limited to a small number of sites N, which should be accessible in experiments with small Jaynes-Cummings chains.

CHAPTER 5

Imaging photon lattice states by scanning defect microscopy

Resonator lattices (section 2.5.1) are a vital building block for quantum information technology based on circuit-QED architecture. It forms the bare bones of the Jaynes-Cummings lattice (section 2.5.2), which is a fascinating platform for quantum simulation. It also mediates qubit-qubit interaction by resonator photons, namely the "quantum bus" [131, 132], for quantum computation. The fabrication and measurement of resonator lattices hence play an important role.

Resonator lattices with very low disorder in bare resonator frequencies and hopping rates between sties can be fabricated reliably [52]. However, measuring and probing lattice states remain a experimental challenge. In general, large two-dimensional resonator lattices can only be directly probed on predetermined lattice sites at the edge. Measurements at the lattice edge can only provide limited and indirect information about the bulk part of the lattice.

In collaboration with Andrew Houck's lab, scanning defect microscopy has been introduced for circuit-QED lattices to overcome these limitations. Scanning defect microscopy allows the measurement of the photon occupations in the bulk part of a lattice. The microscopy makes use of small piece of dielectric material (the probe) mounted on a cryogenic three-axis positioning stage similar to those used in the scanning tunneling microscopy, see fig. 5.1 for a schematic. This is used to put the probe above a target resonator in a well-controlled way. The proximity of the dielectric probe shifts the local

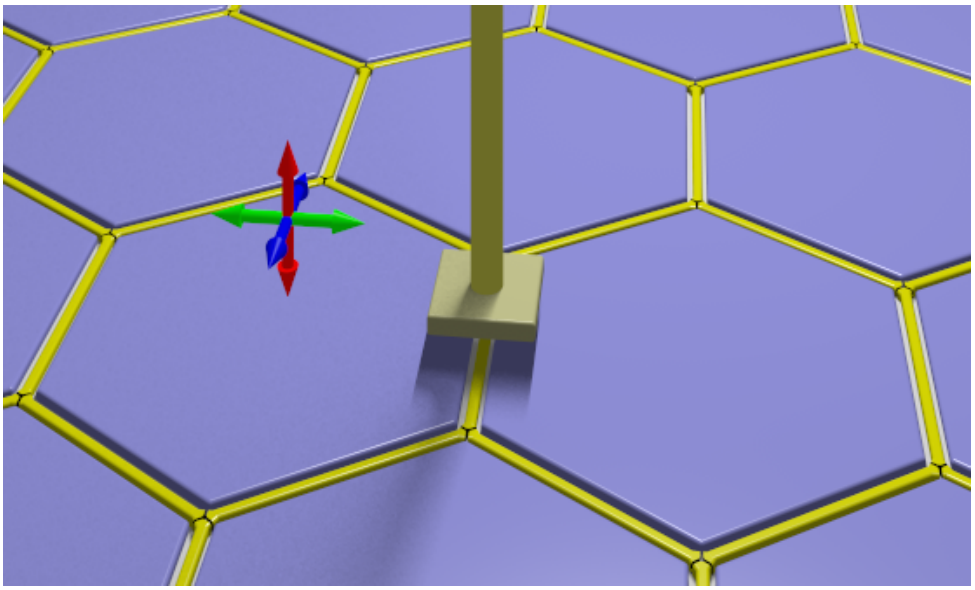

Figure 5.1. **Schematic diagram of scanning defect microscopy**. A dielectric probe is scanned across a lattice of transmission line resonators. The probe shifts the frequency of a target resonator and creates a local lattice defect. The transmission through the lattice systematically depends on the defect size and can be used to image the photon occupancies across the lattice.

resonator frequency. (I will discuss a crude model for this frequency shift in section 5.2.) The shift creates a local defect in the lattice with a size (magnitude of the frequency shift) controllable by tuning the vertical distance between the probe and the resonator. By analyzing the change of the transmission spectrum for different defect sizes, local information specific to the selected bulk resonator can be revealed as discussed in section 5.3. Scanning the probes through different lattice sites allows one to map the normal-mode photon occupations for the full resonator lattice. Experimental data of such a normal-mode image is shown in section 5.4. (We have reported these theoretical and experimental results in ref. 55.)

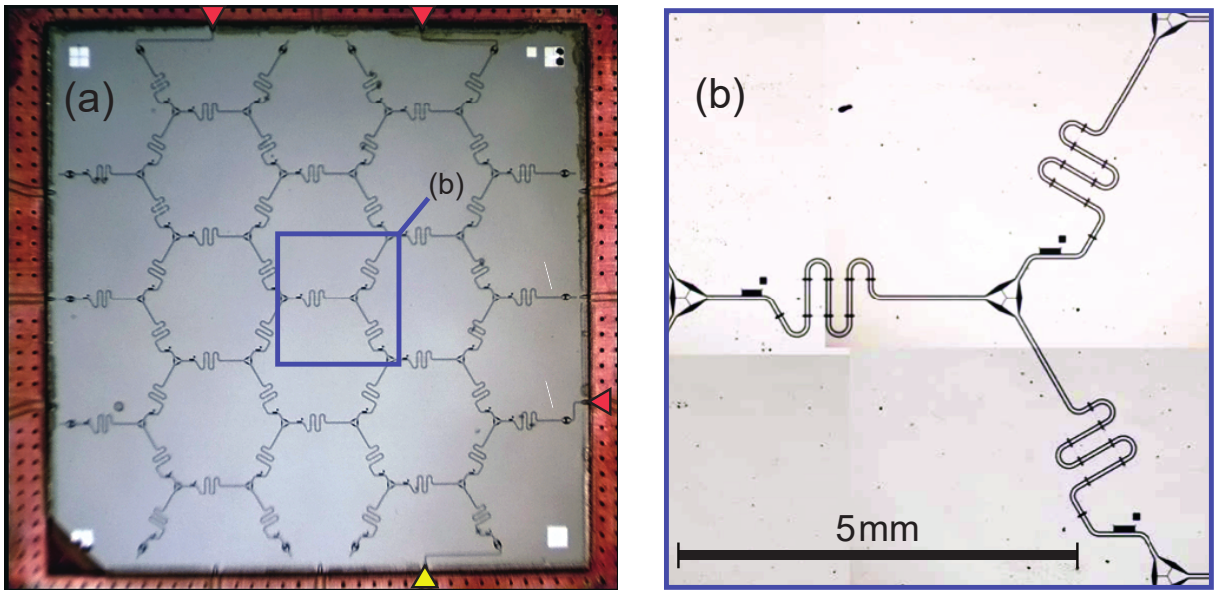

Figure 5.2. **Experimental device consisting of 49 coupled transmission line resonators**. (a) The resonators are fabricated to form a Kagome lattice. The lattice can be driven by a coherent microwave tone through the port marked by the yellow triangle. Any one of the three output ports (red triangles) can be used to detect the transmission signal. (b) Resonators are coupled by three-way capacitors. One section of each resonator meanders to save space on the chip. (This figure is identical to fig. 2.6.)

5.1. Resonator lattice and dielectric probe

The experimental setup consists of 49 transmission line resonators fabricated on a $32 \times 32\,\mathrm{mm}^2$ chip [fig. 5.2(a)]. Three-way capacitors ("nodes") couples the resonators (lines with a meandering section) [fig. 5.2(b)]. At the edge of the lattice, four resonators are capacitively coupled to the input or output ports. One input port [yellow triangle in fig. 5.2(a)] is used to feed a coherent drive tone with tunable drive frequency ω_d into the lattice. Three different output ports [red triangles in fig. 5.2(a)] are used to measure transmission signal. Note that the resonator array forms a Kagome lattice (the dual of the honeycomb lattice).

The dielectric probe consists of a $2.2 \times 2.2\,\mathrm{mm}^2$ piece of sapphire. It is mounted to a cryogenic three-axis positioning stage. This allows the probe to move across the lattice and to be brought close to a target resonator. The presence of the dielectric locally perturbs the bare frequency of the target resonator. This can be interpreted as creating a local defect at the target site. The defect size (magnitude of the frequency shift) is tuned by varying the height of the probe above the surface of the resonator.

To measure the local information on each site of the lattice, the probe is first centered above the resonator. The distance between the probe and target resonator is reduced until contact is made between the probe and the chip. The probe is then retracted stepwise and transmission measurements are performed at each step. The retract-measure cycle repeats until the probe is approximately 300 μm above the chip. (When the probe is more than 200 μm above the chip, the frequency shift is small and asymptotically approaches zero.) The three-axis positioning stage allows the probe to move from one site to another. However, the probe cannot access the whole chip within a single scan due to the limited range of the positioners. Several cooldowns were performed to scan the full lattice.

5.2. Modeling the impact of dielectric probe

The proximity of the dielectric probe increases the capacitance of the transmission line resonator through mutual capacitance. A crude model with position-dependent capacitance is employed to qualitatively study the effect due to the probe on the resonator frequency. An accurate quantitative prediction, however, has to rely on finite-element simulations for electromagnetic field using the HFSS package[1].

[1]Result of the HFSS simulations can be found in our publication [55].

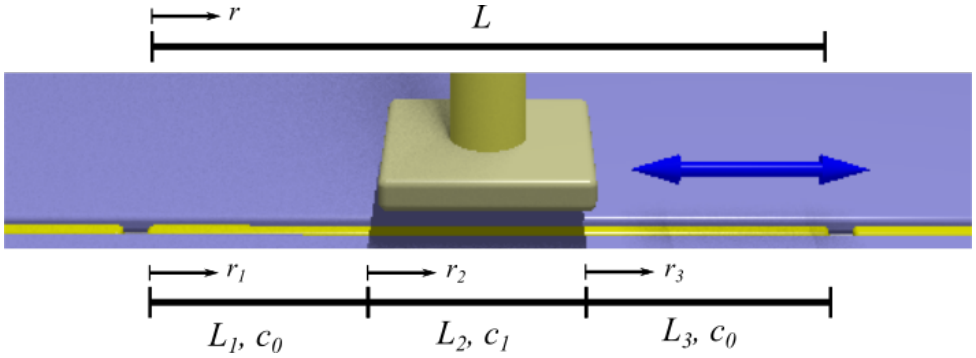

Figure 5.3. **Schematic diagram of the resonator perturbed by the probe**. The capacitance of the transmission line resonator with length L increases due to the proximity of the dielectric probe through mutual capacitance. This increase is modeled by a higher capacitance $c_1 > c_0$ per unit length in the middle part of the resonator. The lateral movement of the probe is incorporated into the model by adjusting the section lengths L_1, L_2 and L_3 (with $L_1 + L_2 + L_3 = L$).

The model is formulated in a way similar to the case of the standard transmission line resonator discussed in section 2.3: a transmission line with length L, uniform capacitance c and inductance ℓ per unit length, and capacitive coupling to the left and right with capacitances C_L and C_R, respectively. The presence of the probe breaks the uniformity of the capacitance and results in a position-dependent capacitance $c(r)$ per unit length. The capacitance $c(r)$ depends on the relative position between the probe and resonator, the probe geometry and the resonator geometry in a highly non-trivial way. However, a crude model with the resonator divided into three distinct sections (fig. 5.3) is sufficient to provide us with a qualitative understanding. The middle section of the resonator is modeled to have a larger capacitance $c_1 > c_0$ per unit length compared to the other two sections. The increased capacitance is intended to mimic the effect due to the probe. The capacitance c_1 per unit length attains its maximum if the probe touches the resonator and c_1 tends to c_0 when the probe moves vertically away from the resonator.

We express the capacitance per unit length as

$$c(r) = \begin{cases} c_1 > c_0 & \text{if } r \in [L_1, L_1 + L_2], \\ c_0 & \text{otherwise.} \end{cases} \tag{5.1}$$

Here, $[L_1, L_1 + L_2]$ is the region of the middle section with higher capacitance. Slightly modifying eqs. (2.13) and (2.14) in section 2.3, the eigenmodes $\varphi_\mu(r)$ and eigenfrequencies ω_μ of the transmission line resonator are determined by the second-order differential equation

$$\frac{\mathrm{d}^2\varphi_\mu(r)}{\mathrm{d}r^2} = -\ell\, c(r)\omega_\mu^2\varphi_\mu(r), \tag{5.2}$$

and the boundary conditions

$$\begin{cases} -\frac{\mathrm{d}\varphi_\mu(r)}{\mathrm{d}r}\Big|_{r=0} = \ell\, C_L\omega_\mu^2\varphi_\mu(r=0), \\ \frac{\mathrm{d}\varphi_\mu(r)}{\mathrm{d}r}\Big|_{r=L} = \ell\, C_R\omega_\mu^2\varphi_\mu(r=L), \\ \varphi_\mu(r) \text{ and } \frac{\mathrm{d}\varphi_\mu(r)}{\mathrm{d}r} \text{ are continuous at } r = L_1 \text{ and } r = L_1 + L_2. \end{cases} \tag{5.3}$$

We introduce the coordinates r_1, r_2 and r_3 as shown in fig. 5.3. The solution of the differential equations has this form:

$$\begin{cases} \varphi_\mu(r_1) = A_1 \sin\left(\omega_\mu r_1/v_0\right) + B_1 \cos\left(\omega_\mu r_1/v_0\right), \\ \varphi_\mu(r_2) = A_2 \sin\left(\omega_\mu r_2/v_1\right) + B_2 \cos\left(\omega_\mu r_2/v_1\right), \\ \varphi_\mu(r_3) = A_3 \sin\left(\omega_\mu r_3/v_0\right) + B_3 \cos\left(\omega_\mu r_3/v_0\right), \end{cases} \tag{5.4}$$

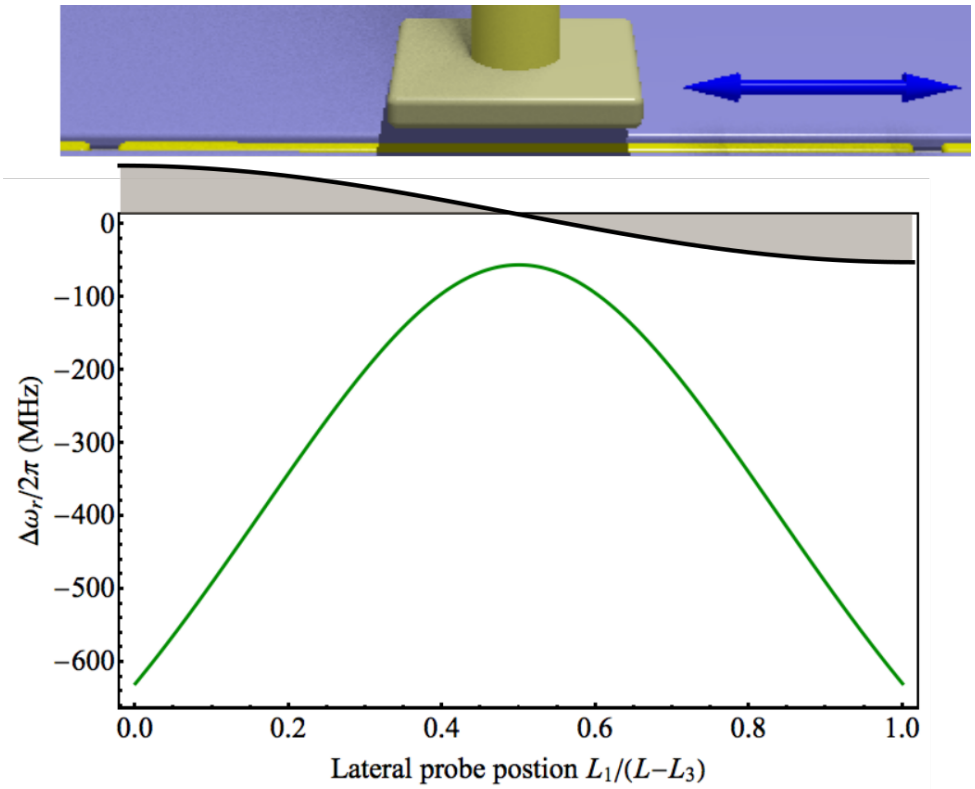

Figure 5.4. **Frequency shift $\Delta\omega$ vs. the lateral probe position**. The frequency shift $\Delta\omega$ due to the dielectric probe is simulated according to eq. (5.4) using a set of parameters motivated by the experimental setup. The lateral probe position is modeled by shifting the middle section of the transmission line resonator with higher capacitance. The frequency shift $\Delta\omega$ follows the field distribution of the $\lambda/2$ mode, exhibiting maxima close to the resonator ends where the field is strongest, and a minimum at the resonator midpoint.

where $v_0 = (\ell c_0)^{-1/2}$ and $v_1 = (\ell c_1)^{-1/2}$ are the phase velocities in the corresponding sections, and A_j and B_j $(j = 1, 2, 3)$ are constants determined by the boundary conditions and normalization. Substituting eq. (5.4) into the boundary conditions (5.3) results in a homogeneous system of linear equations, which determines the eigenfrequencies ω_μ.

We focus on the $\lambda/2$-mode frequency ω_0, which is close to the drive frequency ω_d. If the probe moves vertically away from the resonator, ω_0 approaches the unshifted frequency

ω. The frequency shift $\Delta\omega$ is given by the difference between ω_0 and ω, i.e. $\Delta\omega = \omega_0 - \omega$, which is a function of the probe position. The simulation result using a set of parameters motivated by the experimental setup is shown in fig. 5.4. The frequency shift $\Delta\omega$ is always negative, meaning that the proximity of the probe decreases the mode frequency (which is the direct consequence of the increased capacitance c_1 per unit length). The shift also follows the field distribution of the $\lambda/2$ mode. The strongest shifts occur when the probe is near the edge, where the field has the highest amplitude. On the other hand, the weakest shift is realized at the resonator midpoint where the field amplitude is zero. These features qualitatively match with the experimental observation (fig. 2 of ref. 55).

5.3. Normal-mode imaging: model

To explain the underpinning for imaging of normal modes with scanning defect microscopy, we consider the heterodyne transmission through a driven-damped resonator lattice as described by the Lindblad master equation or input-output theory formalism [133, sec. 7.2]. The lattice is coherently driven through one input port, attached to a particular edge site $n_{\rm in}$ of the lattice. The transmission amplitude is measured through an output port, and is directly proportional to the coherent-state amplitude $|\langle \mathsf{a}_{\rm out}\rangle|$ at the corresponding edge site $n_{\rm out}$. The equation relating the coherent-state amplitude $\alpha_n = \langle \mathsf{a}_n\rangle$ at any lattice site n to the drive amplitude ϵ is [93]

$$\left(\omega - \omega_d - i\frac{\gamma}{2}\right)\alpha_n + \kappa \sum_{\langle n,m\rangle} \alpha_m = -\epsilon\,\delta_{nn_{\rm in}}, \tag{5.5}$$

where ω and ω_d denote the bare resonator and drive frequency, κ the photon hopping strength between neighboring resonators, and γ the uniform photon decay rate. (The bare resonator frequency corresponds to the unshifted $\lambda/2$-mode frequency of the resonator.)

The above equation has a matrix representation by introducing the set of basis vectors $\{|n)\}_{n=1,2,\cdots,N}$ with each vector corresponding to a particular site and N the total number of sites. For mere convenience, we use vector notation where $|\alpha)$ collects the coherent-state amplitudes on each lattice site, $(n|\alpha) = \alpha_n$, and $|\epsilon)$ encodes the drive on each site – here acting only on the input port, $(n|\epsilon) = \epsilon\,\delta_{nn_{\rm in}}$. Note that although the vector notation looks the same as the bra-ket notation introduced in eq. (3.11), they are not related to each other. We will use this vector notation (instead of the bra-ket notation) throughout this chapter. Using the vector notation, eq. (5.5) is represented by

$$\left[(\omega - \omega_d - i\frac{\gamma}{2})\mathbf{1} + \kappa\,\mathbf{K}\right]|\alpha) = |\epsilon)\,, \tag{5.6}$$

where $\mathbf{1}$ is the identity matrix and the real-symmetric matrix $\mathbf{K}$ is the adjacency matrix of the lattice. Transmission resonances naturally occur at the normal-mode frequencies ω_μ of the lattice, obtained from the usual normal-mode eigenvalue equation $(\omega\mathbb{1} + \kappa\,\mathbf{K})\,|\mu) = \omega_\mu\,|\mu)$. As a result, the coherent-state amplitude at the output site takes the simple form

$$\alpha_{\rm out} = -\sum_\mu (n_{\rm out}|\mu)\frac{1}{(\omega_\mu - \omega_d) + i\frac{\gamma}{2}}(\mu|n_{\rm in})\,\epsilon. \tag{5.7}$$

Accordingly, each normal mode with nonzero mode amplitude at both input and output port will produce a transmission peak when the drive frequency coincides with the normal-mode frequency. (This assumes frequency spacing between modes to be larger than γ, which is appropriate for the lattice investigated here.)

Once a certain normal mode μ is on resonance, its normal-mode weight $W_{\mu n} = |(n|\mu)|^2$ on each lattice site n can be extracted by the dielectric probe. The proximity of the probe to lattice site n introduces a small shift of the bare cavity frequency $\Delta\omega_n$ as shown in section 5.2. This lattice defect induces a frequency shift $\Delta\omega_{\mu|n}$ in the normal-mode frequency. The connection between the small normal-mode frequency shifts and the mode weights is established by simple perturbation theory. We write the new normal-mode matrix including the defect as $\mathbf{H}_n = \omega\mathbf{1} + \Delta\omega_n\mathbf{D}_n + \kappa\,\mathbf{K}$, where $\mathbf{D}_n = |n)\,(n|$ selects the site of the defect. Applying perturbation theory with respect to the defect $\Delta\omega_n\mathbf{D}_n$, we immediately obtain the leading-order frequency shift for normal mode μ caused by a defect on site n:

$$\Delta\omega_{\mu|n} = \Delta\omega_n\,(\mu|\,\mathbf{D}_n\,|\mu) = \Delta\omega_n\,W_{\mu n}. \tag{5.8}$$

The magnitude of the defect is easily tuned by varying the height of the probe above the surface of the resonator. The weight of the (undisturbed) normal mode μ on site n is thus obtained as the ratio of mode frequency shift and defect size in the limit of small shifts,

$$W_{\mu n} = \frac{\Delta\omega_{\mu|n}}{\Delta\omega_n} \;\rightarrow\; \left.\frac{d\omega_{\mu|n}}{d\omega_n}\right|_{\omega_n=\omega}. \tag{5.9}$$

5.4. Normal-mode images

The weights $W_{\mu n}$ of normal mode μ at site n can be determined using scanning defect microscopy. To map the mode weights $W_{\mu n}$ for the whole lattice, the mode frequency shifts $\Delta\omega_{\mu|n}$ induced by the probe are measured at all sites. As described in section 5.1, measurement at a single site consists of centering the probe above the target resonator, followed by a series of transmission measurements for various probe heights z above the chip. To obtain the frequency shift $\Delta\omega_{\mu|n}$ of normal mode μ due to the probe above site n, the resonance frequency is traced by fitting Lorentzians to the relevant part of the transmission spectra. Moreover, the probe heights z is converted into the corresponding defect size $\Delta\omega_n$ using the prediction from HFSS simulations. (The simulations are challenging since one have to simulate the case with small defect size. This means that simulating a large spatial region is necessary such that the probe is far away from the resonator. This poses a computational challenge to the finite-element simulations and limits the range of probe heights which can be simulated.) Hence, one can experimentally determines mode frequency shift $\Delta\omega_{\mu|n}$ as a function of defect size $\Delta\omega_n$. This gives the normal-mode weights $W_{\mu n}$ according to eq. (5.9).

Three well-separated modes are selected, namely the modes $\mu = 35$ and 36, and the highest-frequency mode mode $\mu = 49$. The normal-mode weights of the selected modes and the theory predictions[2] are shown in fig. 5.5. Overall, the mode images show good qualitative agreement with the theoretical predictions (fig. 5.5, top panels). To good approximation, the mode images show the mirror symmetry predicted by theory along the vertical and horizontal axes crossing through the center site. Deviations of the measured

[2]The theory calculation of mode weights accounts for a small amount of systematic disorder in frequencies among the different categories of resonators (bulk resonators vs. edge resonators).

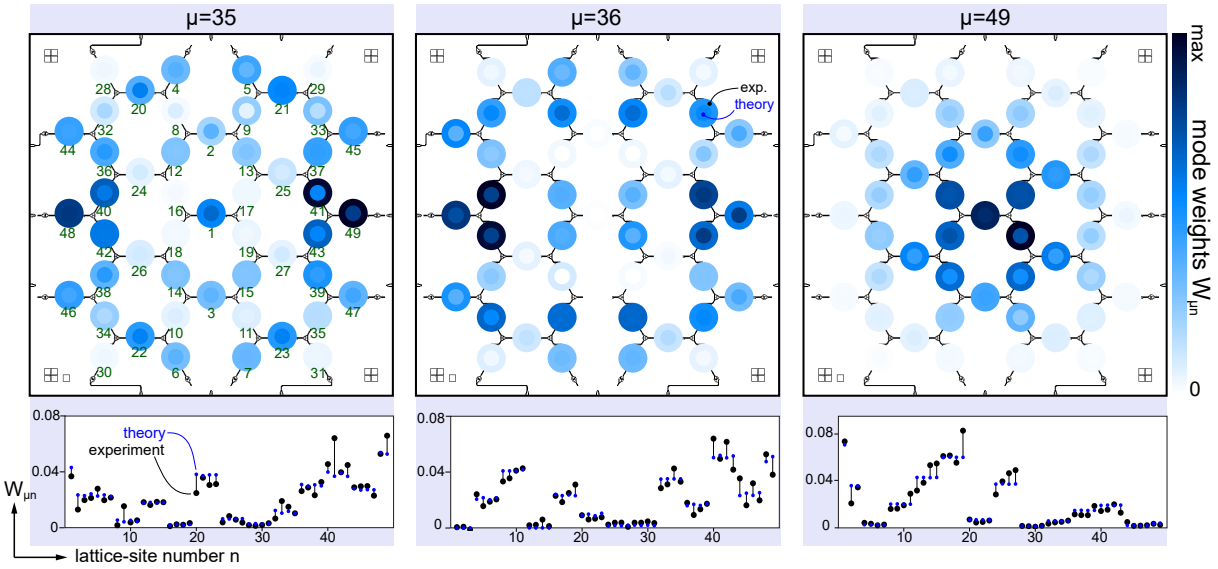

Figure 5.5. **Normal-mode weights for three selected modes, μ = 35, 36 and 49**. For each lattice site n, the mode weight $W_{\mu n} = |(n|\mu)|^2$ is depicted an overlay of two color-coded disks. Inner disks represent the theory prediction for the weights, the outer disks the weights determined experimentally by scanning defect microscopy. The bottom panels show deviations in normal-mode weights as lines connecting experimental data (black dots) and theory prediction (blue dots). Comparison shows good agreement with noticeable deviations in only a few sites in each case.

mode weights from the theory predictions are quantitatively displayed in the bottom panels of fig. 5.5. Even though some lattice sites show larger deviation compared to other, the sites with larger deviation are mostly different for each selected mode. This suggests that larger deviations are not specific to particular lattice sites. While one cannot rule out lattice disorder as the source of the deviations, the lattice disorder may be expected to be small [52]. It is more likely that the deviations are primarily due to the difficulty of precise calibration of defect sizes induced by the probe, a procedure which relies on HFSS simulations within a restricted range of probe heights as mentioned before.

Table 5.1. Quantitative comparison between theoretical predictions and experimental results for normal-mode weights as obtained from scanning probe microscopy.

Mode μ	Fidelity $\mathcal{F}_\mu$	Normalized rms n-rms$_\mu$
35	0.990	12%
36	0.989	10%
49	0.993	9%

To make an overall quantitative comparison between theory predictions and experimental results, we consider the fidelity,

$$\mathcal{F}_\mu = \sum_n (W_{\mu n}^{\mathrm{exp}}\, W_{\mu n}^{\mathrm{th}})^{1/2}, \tag{5.10}$$

and the normalized root-mean-square deviation (n-rms),

$$\text{n-rms}_\mu = \frac{(\frac{1}{N}\sum_n \Delta W_{\mu n}^2)^{1/2}}{\max_n(W_{\mu n}^{\mathrm{th}}) - \min_n(W_{\mu n}^{\mathrm{th}})}. \tag{5.11}$$

Table 5.1 shows the fidelities and n-rms values achieved in the experiment. The fidelities are close to 1 for all three modes, confirming good overall agreement. The n-rms values indicate that the averaged deviations are of the order of 10%. While not a high-precision measurement, scanning defect microscopy thus provides us a with a detailed and quantitative image of normal-mode weights of the resonator lattice.

CHAPTER 6

Dissipative phase transition in a circuit-QED chain

As discussed in section 3.6, the analytical and numerical techniques for investigating open quantum lattices are relatively less developed compared to their closed-system counterparts. Hence, the theoretical study of open quantum lattices tends to be challenging. This makes the development of nonequilibrium quantum simulators for open lattice models particularly intriguing.

Interacting photonic systems based on superconducting circuits represent a useful toolbox to study open quantum lattices. Collaborating with Andrew Houck's lab, we have developed one of the first circuit-QED lattices – a circuit-QED chain with 72 sites suitable for investigating nonequilibrium many-body physics. I have analyzed the result by employing appropriate models and theoretical methods. We have reported the observation of a dissipative phase transition in ref. [25].

In this chapter, I will first briefly review the general features of dissipative phase transitions. This is followed by a simple discussion of the experimental device realizing the circuit-QED chain. Two different models will then be employed to theoretically investigate the qualitative behavior of the device. The experimental observation and evidence of a dissipative phase transition will be explained subsequently.

6.1. Dissipative phase transitions

A phase transition occurs when a system exhibits a non-analytic change upon tuning a system parameter. Quantum phase transitions are one example – a quantum phase transition takes place when the ground state $|\psi_0\rangle$ undergoes a sudden change. The criterion for such a transition is easily specified when considering the eigenenergies E_μ of the Hamiltonian H: a quantum phase transition takes place when the energy gap $\Delta E = E_1 - E_0$ between the ground and first excited states closes[1]. (In other words, the first excited state $|\psi_1\rangle$ becomes degenerate with the ground state $|\psi_0\rangle$ at the phase boundary.) This renders the energy gap ΔE a useful quantity characterizing quantum phase transitions.

Markovian open quantum systems, governed by the Lindblad master equation (3.8), can also exhibit phase transitions – a dissipative phase transition is characterized by the non-analytic change of the nonequilibrium steady state $|\mathsf{\rho}_s)$.[2] Analogous to the ground state $|\psi_0\rangle$ being the lowest-energy eigenstate of H, the steady state $|\mathsf{\rho}_s) = |\mathsf{u}_0)$ is a eigenstate of the Liouville superoperator $\mathbb{L}$ associated with the smallest eigenvalue $\lambda_0 = 0$ in magnitude. (See section 3.3 for a discussion of the nonequilibrium steady state.) Hence, to specify a dissipative phase transition, the relevant quantities are the complex eigenvalues λ_μ of $\mathbb{L}$. (As explained in section 3.2, the real parts of λ_μ encode the relaxation timescales, while the imaginary parts encode the oscillatory timescales.) Let us recall the discussion of the asymptotic decay rate (ADR) from section 3.3 that λ_{ADR} is the eigenvalue with its real part closest to zero. One can then define the indicator of dissipative phase transitions to

[1]Roughly speaking, the ground and first excited states switch their roles when going across the phase boundary.

[2]Other than dissipative phase transition, dynamical phase transitions are another type of phase transitions dealing with the dynamical instead of the steady-state behavior.

Table 6.1. Comparison between quantum phase transitions and dissipative phase transitions. (This table is a modified version of Table I in ref. 29.)

	Quantum phase transitions	Dissipative phase transitions
System (super)operator	Hamiltonian H	Liouville superoperator $\mathbb{L}$
Relevant quantities	Eigenenergies E_μ of H	Eigenvalues λ_μ of $\mathbb{L}$
Relevant state	Ground state$\|E_0\rangle$: $(\mathsf{H} - E_0)\,\|E_0\rangle = 0$	Steady state ρ_s: $\mathbb{L}\,\|\rho_s) = 0$
Phase transition	Energy gap ΔE vanishes $\Delta E = E_1 - E_0$	ADR vanishes ADR $= -\mathrm{Re}\,\lambda_{\mathrm{ADR}}$

be the eigenvalue gap $\mathrm{Re}(\lambda_0 - \lambda_{\mathrm{ADR}}) = -\mathrm{Re}\,\lambda_{\mathrm{ADR}} = \mathrm{ADR}$. This means that a dissipative phase transition is characterized by the vanishing of the ADR. As explained in section 3.3, the inverse of the ADR corresponds to the longest timescale for the system to relax to the unique steady state $|\rho_s)$. The vanishing of the ADR, or $1/\mathrm{ADR} \to \infty$, makes it possible that the system never relaxes to $|\rho_s)$. In other words, the steady state $|\rho_s)$ loses uniqueness when a dissipative phase transition occurs. The comparison between quantum phase transitions and dissipative phase transitions is summarized in section 6.1.

As discussed in section 3.3, a unique steady state is guaranteed if the jump operators and Hamiltonian "connect" the full Hilbert space and the Hilbert space is finite-dimensional. In most of the models relevant to circuit-QED devices, the Hilbert space is fully connected by photon decay and/or qubit relaxation. Dissipative phase transitions are possible only when the condition of finite dimensionality of Hilbert space is violated. This means that on the phase boundary, the number of excitations in the system is unbounded[3]. This condition is also referred to as "thermodynamic limit", which can be achieved in two different ways:

[3]Note that the number of excitations being unbound is necessary but not sufficient for a dissipative phase transition to take place.

(i) The system may consist of just a few degrees of freedom such as a driven-damped harmonic oscillator discussed in section 3.4. In that case, the excitation number is unbounded if the resonator is driven on resonance in the limit of zero dissipation ($\gamma \to 0$). This means that the excitations in principle grow in number indefinitely[4] with the coherent drive being the source. In general, a system may approach the thermodynamic limit if its characteristic decay rate goes to zero. Note that even though a driven-damped harmonic oscillator can achieve the thermodynamic limit, one cannot observe a dissipative phase transition due to the absence of nonlinearity. One simple way to incorporate nonlinearity is by considering the open Jaynes-Cummings model consisting of a qubit coupled to a driven-damped harmonic oscillator. There, a dissipative phase transition is predicted by H. J. Carmichael [134], and the thermodynamic limit is reached when $\frac{g}{\gamma} \to \infty$ with γ the photon decay rate and g the coupling rate between the resonator and qubit.

(ii) The system consists of an infinite number of degrees of freedom, e.g. a lattice with an infinite number of sites. (This is what is usually referred to as the thermodynamic limit in condensed-matter physics.) In this case, even with a small number of excitations per degree of freedom, it is possible for the total number of excitations to be unbounded. This is the case of dissipative phase transitions predicted for the driven-damped spin chains/lattices [28, 112, 135].

In the next section, I will discuss the experimental device – a circuit-QED chain with 72 sites and small but finite dissipation rates. Strictly speaking, although a corresponding theoretical model in the thermodynamics limit may serve as a good approximation of

[4]In practice, one has to be careful whether the harmonic oscillator remains a valid model if the system is highly occupied.

the device, the device is not in the thermodynamics limit. This means that the ADR never exactly vanishes and there is always a unique steady state. Instead, at and near the proposed phase boundary for a corresponding infinite chain, the ADR is much smaller than all other system rates[136]. In other words, the inverse of the ADR is much longer than all characteristic timescales of the system. One thus expects a rapid crossover instead of a phase transition.

6.2. Device: resonator chain coupled to transmon qubits

The device is a chain with 72 sites [fig. 6.1(a)]. Each site consists of a transmission line resonator with frequency $\omega/2\pi \approx 7.6$ GHz. The terminating resonator at one end of the chain is coupled to an input port where a coherent drive tone can be fed into the chain. At the other end of the chain, the terminating resonator is coupled to an output port where the transmission signal is measured. Each resonator is capacitively coupled to a transmon qubit [fig. 6.1(b)] with coupling strength g, which is measured to be $g/2\pi \approx 460 \pm 50$ MHz when the qubit is on resonance with the resonator[5]. Between sites, the resonators are capacitively coupled to its nearest neighbors [fig. 6.1(c)], resulting in a photon hopping rate of $\kappa/2\pi \approx 80 \pm 10$ MHz.

An asymmetric SQUID-loop design (section 2.4.4) is used for the transmon qubits. The qubit frequencies are hence tunable in a finite frequency range via an applied magnetic flux. Since it is not feasible in this device to individually control the magnetic flux passing through each SQUID loop, a global magnetic flux is used to simultaneously tune all qubit frequencies. To ensure that the features observed in the experiment are not the artifacts of

[5]The coupling strength g depends on the qubit frequency Ω. The dependence is approximately given by $g(\Omega) = g(\Omega_0)\sqrt{\Omega/\Omega_0}$.

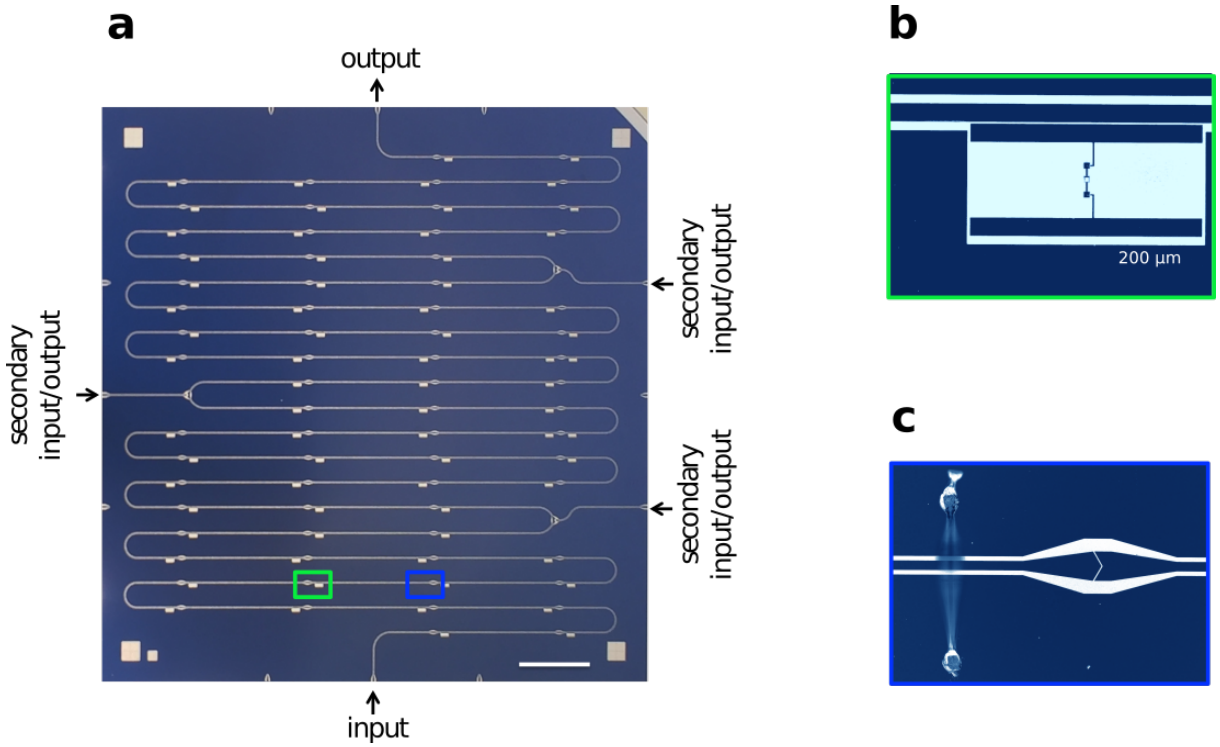

Figure 6.1. **Experimental device consisting of 72 coupled transmission line resonators each coupled to a transmon qubit**. (a) Transmission line resonators, each with a bare resonator frequency of $\omega/2\pi = 7.6$ GHz, are capacitively coupled to form a linear chain on a 2.5 cm $\times$ 2.5 cm chip. On average, each resonator has a photon decay rate of $\gamma/2\pi \approx 1.6 \pm 0.5$ MHz. The two resonators at the ends of the chain are coupled to either the input or output port (arrows on the top and bottom). (b) A transmon qubit is capacitively coupled to each resonator. The coupled resonator-transmon system forms the unit cell of the chain. (c) Each resonator is capacitively coupled to its neighbors to yield a photon hopping rate $\kappa/2\pi = 80 \pm 10$ MHz.

a particular instance of disorder in qubit frequencies, each qubit is intentionally fabricated with a randomized SQUID loop area such that the qubit frequencies are also randomized.

After the conclusion of the experiment, it was discovered that approximately 20% of the qubits were single-junction qubits instead of double-junction qubits consisting of a SQUID loop. (To distinguish these two types of qubits, I call them full qubits and single-junction

qubits, respectively.) The single-junction qubit frequency Ω_{SJ} is independent of the applied magnetic flux.

6.3. Low-power transmission

At low drive power, the number density of excitations in the chain is so low that interaction between excitations is negligible. This means that transmon qubits can be approximated by oscillators. In other words, the circuit is equivalent to a resonator array at low power. The low-power transmission can thus be determined by using an equation similar to eq. (5.5).

The experimental result and theoretical prediction are shown in figs. 6.2(a) and (b). The resonance peaks correspond to resonator modes dispersively shifted by the qubits. The amounts of the dispersive shift depend on the qubit frequencies, which change under varying applied magnetic field. This results in the dependence of the resonance peak frequencies on the applied magnetic field as shown in the figures.

The full qubit and the single-junction qubit frequencies are not known with high certainty due to the challenges in fabrication, see the gray shaded region in fig. 6.2(c). Moreover, the spatial distribution of the single-junction qubits within the chain is not known. Hence, in order to simulate the transmission, we must make assumptions regarding the qubit frequencies and the spatial distribution of the single-junction qubits. The theoretical and experimental results qualitatively agree when *assuming* that the full qubit frequencies $\Omega_j/2\pi$ are between 12.7 GHz and 13.9 GHz, the single-junction qubit frequency $\Omega_{\mathrm{SJ}}/2\pi$ is at 9.5 GHz, and all single-junction qubits are located near the input port[6].

[6]This spatial configuration is motivated by the expectation that the single-junction qubits are due to imperfections during the fabrication process. The single-junction qubits are thus likely to be spatially correlated.

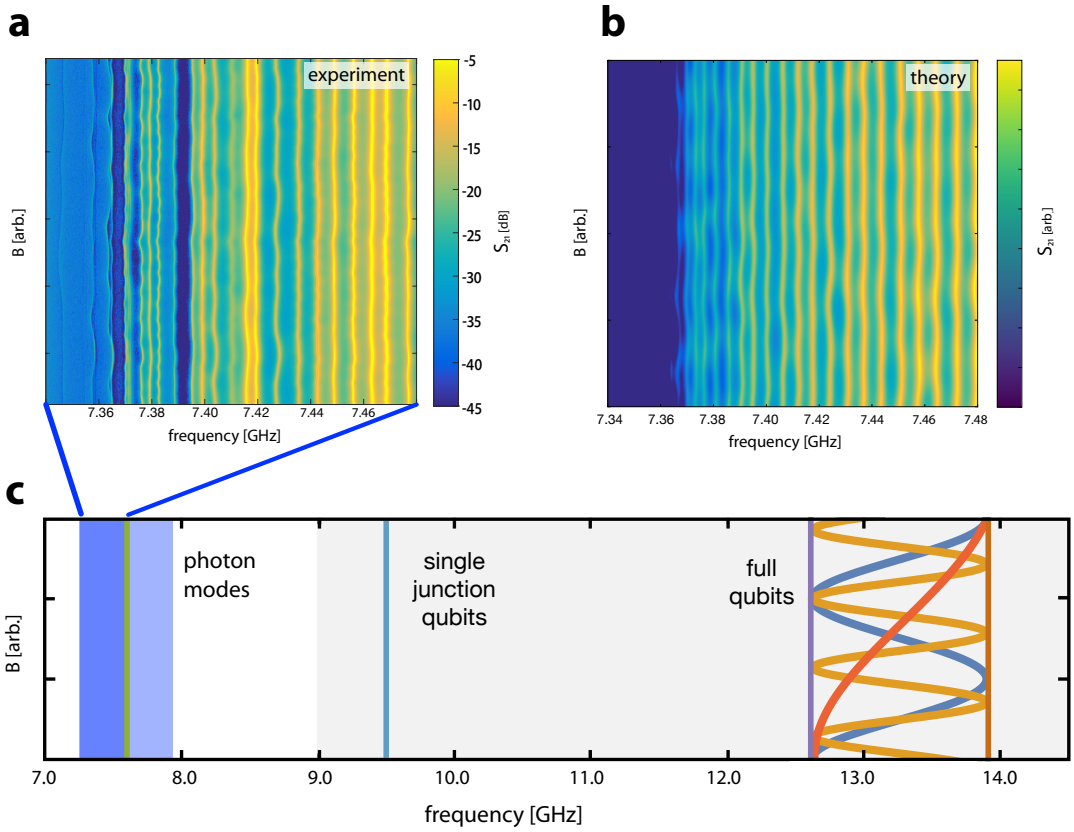

Figure 6.2. **Low-power transmission.** Transmission as a function of applied magnetic field as (a) measured experimentally, and (b) predicted theoretically. The resonance peaks are dispersively shifted by the qubits. Since the qubit frequencies change under varying applied magnetic field, the frequencies of the resonance peaks also change accordingly. The theory and experiment qualitatively agree using the following set of parameters: $\omega/2\pi = 7.6$ GHz, $\Omega_j/2\pi \in [12.7, 13.9]$ GHz, $\Omega_{\mathrm{SJ}}/2\pi = 9.5$ GHz, $g/2\pi = 410\,\mathrm{MHz}$ and $t/2\pi = 90$ MHz. (c) The blue rectangles indicate the frequency range of the photon modes, with the dark blue rectangle indicating the range of frequencies shown in (a) and (b). The gray shaded region reflects the predicted uncertainty range of the qubit frequencies. The curves represent the qubit frequencies used in the theoretical prediction.

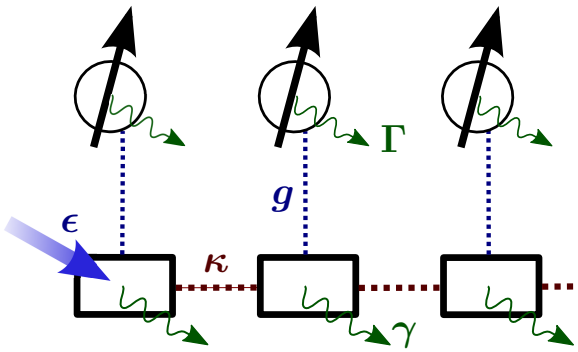

Figure 6.3. **Schematic of the open Jaynes-Cummings chain**. The chain consists of N sites. On each site, a resonator is coupled to a two-level system with Jaynes-Cummings interaction strength g. The resonators are coupled to their nearest neighbors through photon hopping with rate κ. Excitations can leave the chain through photon decay and qubit relaxation with rates γ and Γ, respectively. At one end of the chain, the resonator is coherently driven with frequency ω_d and strength ϵ.

6.4. Driven-damped Dicke model

In this section, in order to study the many-body phenomena due to the qubit-resonator coupling, I consider a toy model – the single-mode Dicke model [137] with drive and dissipation. This toy model[7] is one of the simplest models which allows us to explore the qubit-resonator coupling. Later on in this section, a mean-field treatment will be employed to investigate the steady state of this toy model.

We first approximate the transmon qubits by two-level systems (section 2.4.3). This leads to an open Jaynes-Cummings chain, see fig. 6.3. Its Hamiltonian H is given by

(6.1)
$$\mathsf{H} = \sum_{j=1}^{N} \left[\delta\omega\, \mathsf{a}_j^\dagger \mathsf{a}_j + \frac{\delta\Omega_j}{2} \sigma_j^z + g\left(\mathsf{a}_j^\dagger \sigma_j^- + \mathsf{a}\sigma_j^+ \right) \right] + \sum_{j=1}^{N-1} \kappa \left(\mathsf{a}_j^\dagger \mathsf{a}_{j+1} + \mathsf{a}_j \mathsf{a}_{j+1}^\dagger \right) + \epsilon \left(\mathsf{a}_1^\dagger + \mathsf{a}_1 \right),$$

[7]Using the toy model, we neglect some details, e.g. the non-uniform qubit frequencies, presence of multiple resonator modes, etc.

with site number $N = 72$ and drive strength ϵ. As usual, the time dependence has been eliminated by working in a frame co-rotating with the drive, and $\delta\omega = \omega - \omega_d$ ($\delta\Omega_j = \Omega_j - \omega_d$) is the detuning between the resonator (qubit) frequency and the drive frequency. In our model, we also include dissipation due to photon decay and qubit relaxation with uniform rates γ and Γ across all sites[8]. Using the corresponding jump operators a_j and σ_j^-, the Lindblad master equation is given by

$$\frac{\mathrm{d}\rho}{\mathrm{d}t} = \mathbb{L}\rho = -i\left[\mathsf{H}, \rho\right] + \gamma \sum_{j=1}^{N} \mathbb{D}\left[\mathsf{a}_j\right]\rho + \Gamma \sum_{j=1}^{N} \mathbb{D}\left[\sigma_j^-\right]\rho. \tag{6.2}$$

We determine the eigenmodes of the resonator lattice by diagonalizing the $N \times N$ hopping matrix. This is achieved by the transformation,

$$\mathsf{a}_j = \sum_{\mu=1}^{N} W_{j\mu}\tilde{\mathsf{a}}_\mu, \tag{6.3}$$

where $W_{j\mu}$ is the μ-mode amplitude at at site j, and $\tilde{\mathsf{a}}_\mu$ ($\tilde{\mathsf{a}}_\mu^\dagger$) is the annihilation (creation) operator of the eigenmode μ associated with the eigenfrequency ω_μ. Switching to this eigenmode representation, the Lindblad master equation is rewritten as

$$\frac{\mathrm{d}\rho}{\mathrm{d}t} = -i\left[\mathsf{H}, \rho\right] + \gamma \sum_{\mu=1}^{N} \mathbb{D}\left[\tilde{\mathsf{a}}_\mu\right]\rho + \Gamma \sum_{j=1}^{N} \mathbb{D}\left[\sigma_j^-\right]\rho, \tag{6.4}$$

where

$$\mathsf{H} = \sum_{\mu=1}^{N}\left[\delta\omega_\mu \tilde{\mathsf{a}}_\mu^\dagger\tilde{\mathsf{a}}_\mu + \epsilon\left(W_{1\mu}\tilde{\mathsf{a}}_\mu + \mathrm{h.c.}\right)\right] + \sum_{j=1}^{N}\frac{\delta\Omega_j}{2}\sigma_j^z + g\sum_{j,\mu=1}^{N}\left(W_{j\mu}\tilde{\mathsf{a}}_\mu\sigma_j^+ + \mathrm{h.c.}\right). \tag{6.5}$$

[8]The resonators connected to the input/output port usually have a larger decay rate due to photon leakage. As long as the differences in decay rates are small compared to other relevant physical parameters, in particular g and t, this will not qualitatively change the system behavior.

Here, $\delta\omega_\mu$ is the detuning between the eigenfrequency ω_μ and drive frequency ω_d.

Solving for the steady state of the open Jaynes-Cummings chain is extremely challenging due to the large system size[9]. This motivates us to employ the toy model[10] – the driven-damped Dicke model,

$$\frac{\mathrm{d}\rho}{\mathrm{d}t} = -i\,[\mathsf{H},\rho] + \gamma\ \mathbb{D}\,[\tilde{\mathsf{a}}]\,\rho, \tag{6.6}$$

$$\mathsf{H} = \delta\omega\,\tilde{\mathsf{a}}^\dagger\tilde{\mathsf{a}} + \ \frac{\epsilon}{\sqrt{N}}\left(\tilde{\mathsf{a}}^\dagger + \tilde{\mathsf{a}}\right) + \sum_{j=1}^{N}\frac{\delta\Omega}{2}\sigma_j^z + \frac{g}{\sqrt{N}}\sum_{j}^{N}\left(\tilde{\mathsf{a}}^\dagger\sigma_j^- + \tilde{\mathsf{a}}\,\sigma_j^+\right). \tag{6.7}$$

Note that this Dicke model is different from the open-system Dicke model [26]. For the open-system Dicke model, the system is not driven and its many-body physics is explored by varying the qubit-resonator coupling strength g.

For convenience, we employ the collective spin notations,

$$\mathsf{S}^z = \frac{1}{2}\sum_{j=1}^{N}\sigma_j^z \ \text{ and } \ \mathsf{S}^- = \sum_{j=1}^{N}\sigma_j^-. \tag{6.8}$$

The Lindblad master equation is then rewritten as

$$\frac{\mathrm{d}\rho}{\mathrm{d}t} = \mathbb{L}\rho = -i\,[\mathsf{H},\rho] + \gamma\ \mathbb{D}\,[\tilde{\mathsf{a}}]\,\rho, \tag{6.9}$$

[9]Just keeping two photons per resonator, the dimension of the Hilbert space is $3^{72}\times 2^{72}\approx 10^{56}$.

[10]To arrive at the toy model from the open Jaynes-Cummings chain, it formally involves four assumptions. First, one eigenmode of the resonator lattice dominates over all other eigenmodes. Second, the qubit frequencies are uniform, i.e. $\delta\Omega_j = \delta\Omega$ for all j. Third, the coupling between the resonator modes and two-level systems has a uniform strength i.e. $W_{j\mu}\approx 1/\sqrt{N}$. (The factor $1/\sqrt{N}$ comes from the fact that the mode amplitudes $W_{j\mu}$ approximately scale with $1/\sqrt{N}$ for a resonator chain.) Fourth, the only dissipation channel is photon decay, i.e. $\Gamma = 0$.

where

$$\mathsf{H} = \delta\omega\, \tilde{\mathsf{a}}^\dagger \tilde{\mathsf{a}} + \frac{\epsilon}{\sqrt{N}} \left(\tilde{\mathsf{a}}^\dagger + \tilde{\mathsf{a}}\right) + \delta\Omega \mathsf{S}^z + \frac{g}{\sqrt{N}} \left(\tilde{\mathsf{a}}^\dagger \mathsf{S}^- + \tilde{\mathsf{a}} \mathsf{S}^+\right). \tag{6.10}$$

Note that the total angular momentum S is a conserved quantum number under time evolution. We now make the final assumption for the toy model: the system is restricted to the subspace with maximum total angular momentum, i.e. $S = N/2$. This is justified if all of the qubits are initialized in the ground state. In that case, the system is initially in the $S = N/2$ subspace and will never leave the subspace under the time evolution governed by eq. (6.9).

It is convenient to employ the Holstein-Primakoff transformation [138], $\mathsf{S}^z = \mathsf{b}^\dagger \mathsf{b} - S$ and $\mathsf{S}^- = \sqrt{N - \mathsf{b}^\dagger \mathsf{b}}\mathsf{b}$, where b and $\mathsf{b}^\dagger$ are the annihilation and creation operators of a bosonic mode. This leads to

$$\frac{\mathrm{d}\rho}{\mathrm{d}t} = -\, i\, [\mathsf{H}, \rho] + \Gamma\ \mathbb{D}\, [\tilde{\mathsf{a}}]\, \rho, \tag{6.11}$$

$$\mathsf{H} = \delta\omega\, \tilde{\mathsf{a}}^\dagger \tilde{\mathsf{a}} + \frac{\epsilon}{\sqrt{N}} \left(\tilde{\mathsf{a}}^\dagger + \tilde{\mathsf{a}}\right) + \delta\Omega \left(\mathsf{b}^\dagger \mathsf{b} - \frac{N}{2}\right) + \frac{g}{\sqrt{N}} \left(\tilde{\mathsf{a}} \mathsf{b}^\dagger \sqrt{N - \mathsf{b}^\dagger \mathsf{b}} + \text{h.c.}\right). \tag{6.12}$$

After this transformation, the model describes two bosonic modes $\tilde{\mathsf{a}}$ and b which are coupled nonlinearly.

6.4.1. Mean-field approximation

The mean-field approximation is introduced by the following two coherent displacements,

$$\tilde{\mathsf{a}} = \sqrt{N}\alpha + \mathsf{c} \quad \text{and} \quad \mathsf{b} = \sqrt{N}\beta + \mathsf{d}. \tag{6.13}$$

The two displacement amplitudes $\sqrt{N}\alpha$ and $\sqrt{N}\beta$ are the mean fields with the mean-field parameters α and β. As part of the mean-field approximation, the displacement amplitudes are assumed to dominate over the small fluctuations represented by the mode operators c and d.

We now consider a series expansion with $1/\sqrt{N}$ representing the order-counting parameter. The Liouville superoperator can be decomposed as

$$\mathbb{L} = \sqrt{N}\,\mathbb{L}_0 + \mathbb{L}_1 + \frac{1}{\sqrt{N}}\mathbb{L}_2 + \cdots . \tag{6.14}$$

The leading-order term $\mathbb{L}_0$ is given by[11]

$$\mathbb{L}_0\rho = -i\sqrt{N}\left[\mathsf{H}_0 - i\frac{\gamma}{2}\left(\alpha\mathsf{c}^\dagger - \alpha^*\mathsf{c}\right), \rho\right], \tag{6.15}$$

$$\mathsf{H}_0 = \left(\delta\omega\alpha + g\sqrt{k}\beta + \frac{\epsilon}{N}\right)\mathsf{c}^\dagger + \left[\delta\Omega\beta + \frac{g\left(2k\alpha - \alpha\left|\beta\right|^2 - \alpha^*\beta^2\right)}{2\sqrt{k}}\right]\mathsf{d}^\dagger + \text{h.c.}, \tag{6.16}$$

with $k = 1 - |\beta|^2$. This $\mathbb{L}_0$ describes a lossless system with drive on resonance, meaning that the number of excitations remains bounded in the long-time limit if and only if the drive strength vanishes. Together with eqs. (6.15) and (6.16), this implies that the mean-field parameters α and β must satisfy the following set of nonlinear equations,

$$\left(\delta\omega - i\frac{\gamma}{2}\right)\alpha + g\sqrt{k}\beta + \frac{\epsilon}{N} = 0 \quad \text{and} \quad \delta\Omega\beta + \frac{g\left(2k\alpha - \alpha\left|\beta\right|^2 - \alpha^*\beta^2\right)}{2\sqrt{k}} = 0. \tag{6.17}$$

We find that eq. (6.17) can have a single or multiple solutions, depending on the parameters, i.e. $\delta\omega$, γ, etc. We denote these solution(s) by $\{\alpha_1, \beta_1\}$, $\{\alpha_2, \beta_2\}$, etc.

[11] One needs larger drive power to feed the same number of excitations per site into a longer chain. Hence, we consider ϵ is on the order of N.

For each solution $\{\alpha_j, \beta_j\}$, the corresponding mean-field steady state $\rho_{s;j}^{\mathrm{MF}}$ is determined by the next-order term $\mathbb{L}_{1;j}$, namely $\mathbb{L}_{1;j}\rho_{s;j}^{\mathrm{MF}} = 0$. Here, $\mathbb{L}_{1;j}$ is given by

$$\mathbb{L}_{1;j}\bullet = -i\,[\mathsf{H}_{1;j}, \bullet] + \gamma\,\mathbb{D}\,[\mathsf{c}]\,\bullet, \tag{6.18}$$

where

(6.19)

$$\begin{aligned}\mathsf{H}_{1;j} =& \delta\omega\,\mathsf{c}^\dagger\mathsf{c} + \left[\delta\Omega - \tfrac{g}{\sqrt{k_j}}(\alpha_j^*\beta_j + \alpha_j\beta_j^*)(1 + \tfrac{|\beta_j|^2}{4k_j})\right]\mathsf{d}^\dagger\mathsf{d} \\ &+ \frac{g}{2\sqrt{k_j}}\left[\left(2k_j - |\beta_j|^2\right)\mathsf{c}^\dagger\mathsf{d} - \beta_j^2\mathsf{c}^\dagger\mathsf{d}^\dagger - \left(\alpha_j\beta_j + \frac{\alpha_j\beta_j\,|\beta_j|^2 + \alpha_j^*\beta_j^3}{4k_j}\right)\left(\mathsf{d}^\dagger\right)^2 - \text{h.c.}\right],\end{aligned}$$

and $k_j = 1 - |\beta_j|^2$. Although $\mathbb{L}_{1;j}$ is in a form similar to a Liouville superoperator, it does not necessarily fulfill the spectral properties required by a proper Liouville superoperator. In particular, the system may run away from the mean-field steady state $\rho_{s;j}^{\mathrm{MF}}$ given an infinitesimal perturbation, meaning that the corresponding mean-field solution $\{\alpha_j, \beta_j\}$ is unstable. In the parameter regime relevant to the experiment, we find numerically that there are at most two stable mean-field solutions.

6.4.2. Mean-field bistability

The mean-field solutions are numerically determined from the set of nonlinear equations (6.17). In part of the parameter space, there are two stable mean-field solutions, see fig. 6.4. To understand this mean-field bistability, we recall the decomposition of the Liouville superoperator in eq. (6.14). The mean-field steady states $\rho_{s;j}^{\mathrm{MF}}$ $(j = 1, 2)$ are the exact solution of $\mathbb{L}\rho = 0$ only in the limit of $N \to \infty$, i.e. $(\sqrt{N}\mathbb{L}_0 + \mathbb{L}_{1;j})\rho_{s;j}^{\mathrm{MF}} = 0$. Now, for any

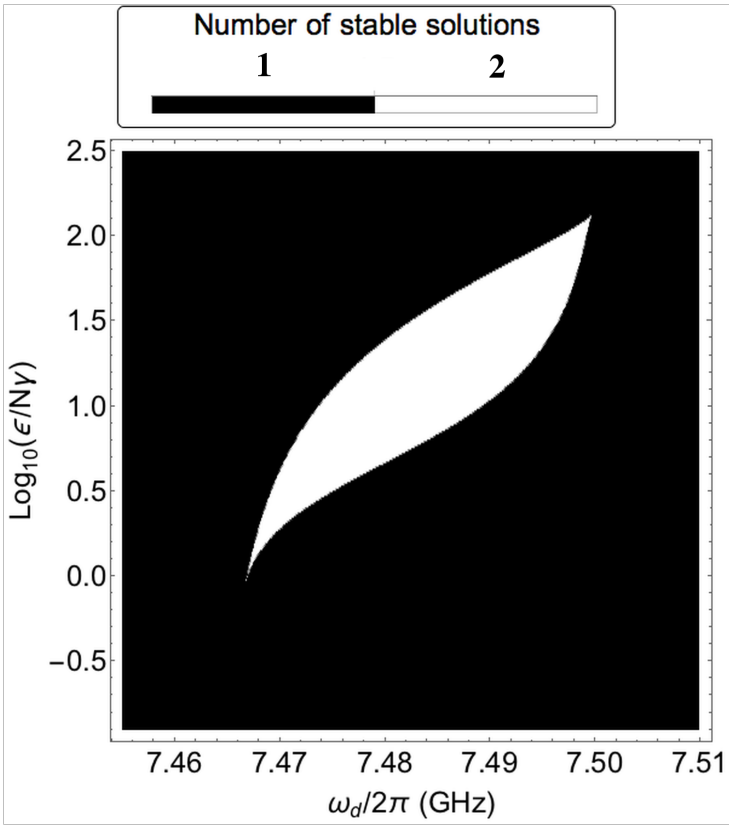

Figure 6.4. **Number of stable mean-field solutions as a function of drive strength ϵ and drive frequency $\delta\omega$.** The white region marks the bistable region with two stable mean-field solutions. (A set of parameters motivated by the experiment setup is used, namely $\omega/2\pi = 7.5$ GHz, $\Omega/2\pi = 13.3$ GHz, $g/2\pi = 450$ MHz and $\gamma/2\pi = 1.6$ MHz.)

finite site number N, one has to consider the corrections from higher-order terms, i.e.

$$\frac{\mathrm{d}\rho^{\mathrm{MF}}_{s;j}}{\mathrm{d}t} = \frac{1}{\sqrt{N}}\mathbb{L}_{2;j}\rho^{\mathrm{MF}}_{s;j} + \mathcal{O}(\frac{1}{N}). \tag{6.20}$$

This suggests that both mean-field steady states correspond to metastable states. The decay rates of the two metastable states are determined by the higher-order terms, which are of leading order $\frac{1}{\sqrt{N}}$.

The mean-field bistability can thus be understood as a dynamical effect [118]. For a driven-damped spin chain [28], the switching between mean-field steady states has been predicted using a quantum trajectories simulation. There, the switching timescale τ_s is long compared to other system timescales. Moreover, for a driven-damped quantum Duffing oscillator, M. I. Dykman and V. N. Smelyanskiy [139] have throughly analyzed the switching between mean-field solutions.

A closely related phenomenon is hysteresis. To observe hysteresis, one tunes a system parameter such that the system moves in the parameter space from a region without bistability to the bistable region. The tuning is in real time with the timescale τ_{tune}. Depending on the tuning path, the system will end up in one of the metastable states as long as the tuning timescale τ_{tune} is much less than the switching timescale τ_s. This path dependence of the final state is usually referred to as hysteresis. The correspondence between the mean-field bistability and hysteresis has been discussed by W. Casteels, *et al.* [140] for a Bose-Hubbard dimer.

The mean-field transmission at a fixed drive frequency is shown in fig. 6.5. At intermediate drive power, there are two mean-field solutions corresponding to the mean-field bistability. We recognize that this bistability falls into the class of optical bistability [141, Sec. 1.1].

6.5. Open circuit-QED chain

In this section, we include multiple modes and higher transmon levels into account. The model under consideration is similar to the open Jaynes-Cummings chain (fig. 6.3) except that the transmon qubits are now approximated by weakly nonlinear resonators

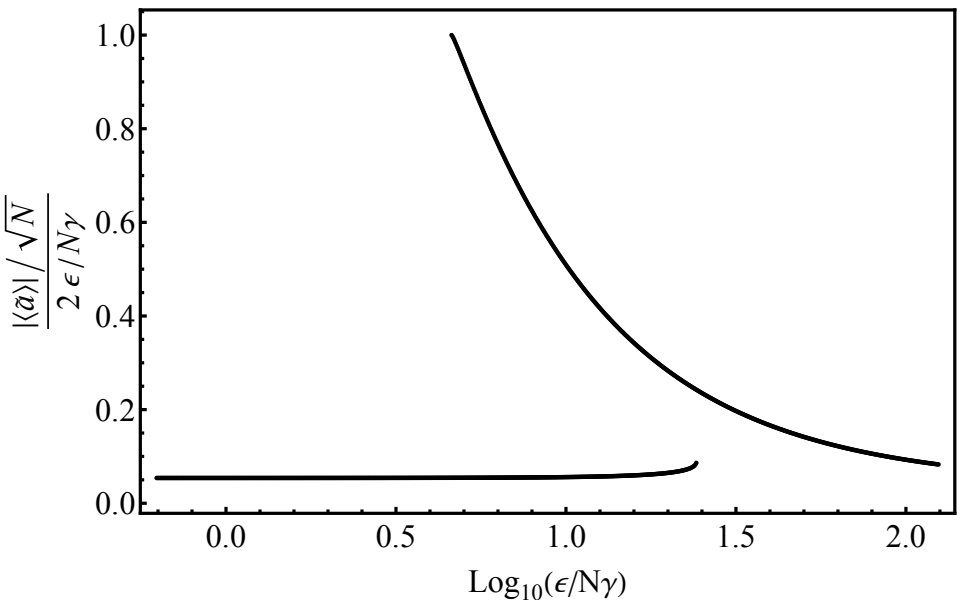

Figure 6.5. **Optically bistability shown at $\omega_d/2\pi = 7.48$ GHz**. In the bistable region, the low-transmission solution is continued to lower drive power; and the high-transmission solution is continued to higher drive power. (All system parameters are identical to those in fig. 6.4.)

instead of two-level systems. For transmon qubits, as long as excitations are restricted to levels inside the cosine potential well, the nonlinearity can be qualitatively modeled by a Bose-Hubbard interaction. We thus consider an open circuit-QED chain (fig. 6.6). In the frame co-rotating with the drive, the chain is govern by the Lindblad master equation

$$\frac{\mathrm{d}\rho}{\mathrm{d}t} = \mathbb{L}\rho - i\,[\mathsf{H}, \rho] + \gamma \sum_{j=1}^{N} \mathbb{D}\,[\mathsf{a}_j]\,\rho + \Gamma \sum_{j=1}^{N} \mathbb{D}\,[\mathsf{b}_j]\,\rho, \tag{6.21}$$

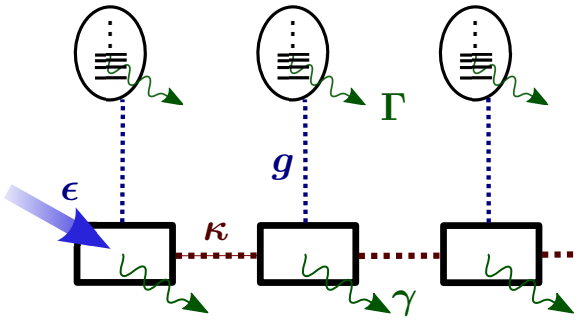

Figure 6.6. **Schematic of the open circuit-QED chain**. The chain is identical to the open Jaynes-Cummings chain except the two-level systems are replaced by weakly nonlinear resonators. The nonlinearity is modeled by a Bose-Hubbard interaction.

where

$$\mathsf{H} = \sum_{j=1}^{N} \left[\delta\omega\, \mathsf{a}_j^\dagger \mathsf{a}_j + \delta\Omega_j\, \mathsf{b}_j^\dagger \mathsf{b}_j + U \mathsf{b}_j^\dagger \mathsf{b}_j^\dagger \mathsf{b}_j \mathsf{b}_j + g \left(\mathsf{a}_j^\dagger \mathsf{b}_j + \mathsf{a}_j \mathsf{b}_j^\dagger \right) \right] + \sum_{j=1}^{N-1} \kappa \left(\mathsf{a}_j^\dagger \mathsf{a}_{j+1} + \mathsf{a}_j \mathsf{a}_{j+1}^\dagger \right) + \epsilon \left(\mathsf{a}_1^\dagger + \mathsf{a}_1 \right). \tag{6.22}$$

Here, transmon qubits are represented by the nonlinear bosonic modes b_j, with Bose-Hubbard interaction strength $U \approx -E_C/2$, where E_C is the charging energy. In the present device, E_C is measured to be 350 ± 40 MHz. (Once again, we ignore disorder effects in our model.)

6.5.1. Quasi-classical mean-field treatment

One can readily show that the equations governing the time evolution of expectation values $\langle a_j \rangle (t)$ and $\langle \mathsf{b}_j \rangle (t)$ are given by

$$i\frac{\mathrm{d}\langle \mathsf{a}_j \rangle}{\mathrm{d}t} = \left(\delta\omega - i\frac{\gamma}{2}\right)\langle \mathsf{a}_j \rangle + g\langle \mathsf{b}_j \rangle + \kappa\left(\langle \mathsf{a}_{j-1} \rangle + \langle \mathsf{a}_{j+1} \rangle\right) + \epsilon\delta_{j1}, \tag{6.23}$$

$$i\frac{\mathrm{d}\langle \mathsf{b}_j \rangle}{\mathrm{d}t} = \left(\delta\Omega_j - i\frac{\Gamma}{2}\right)\langle \mathsf{b}_j \rangle + g\langle \mathsf{a}_j \rangle + 2U\left\langle \mathsf{b}_j^\dagger \mathsf{b}_j \mathsf{b}_j \right\rangle. \tag{6.24}$$

To incorporate the boundary condition, we take $\langle \mathsf{a}_0 \rangle = \langle \mathsf{a}_{N+1} \rangle = 0$. These equations are not closed due to the presence of the term $2U\langle \mathsf{b}_j^\dagger \mathsf{b}_j \mathsf{b}_j \rangle$. Analogous to eq. (6.13), we employ the mean-field approximation by the coherent displacement,

$$\mathsf{a}_j = \alpha_j + \mathsf{c}_j \quad \text{and} \quad \mathsf{b}_j = \beta_j + \mathsf{d}_j, \tag{6.25}$$

where the mean fields α_j and β_j are assumed to dominate over the fluctuations c_j and d_j. The time evolution equations for the mean fields follow from eqs. (6.23) and (6.24),

$$i\frac{\mathrm{d}\alpha_j}{\mathrm{d}t} = \left(\delta\omega - i\frac{\gamma}{2}\right)\alpha_j + g\beta_j + \kappa\left(\alpha_{j-1} + \alpha_{j+1}\right) + \epsilon\delta_{j1}, \tag{6.26}$$

$$i\frac{\mathrm{d}\beta_j}{\mathrm{d}t} = \left(\delta\Omega_j - i\frac{\Gamma}{2}\right)\beta_j + g\alpha_j + 2U\left|\beta_j\right|^2\beta_j. \tag{6.27}$$

For the steady state, the mean fields are stationary, i.e. $\frac{\mathrm{d}\alpha_j}{\mathrm{d}t} = \frac{\mathrm{d}\beta_j}{\mathrm{d}t} = 0$. This results in a large system of coupled nonlinear equations, in which root-finding algorithms are inefficient [37]. Here, we solve for the steady state of the mean-field equations [eqs. (6.26) and (6.27)] by time evolution and extracting the long-time limit.

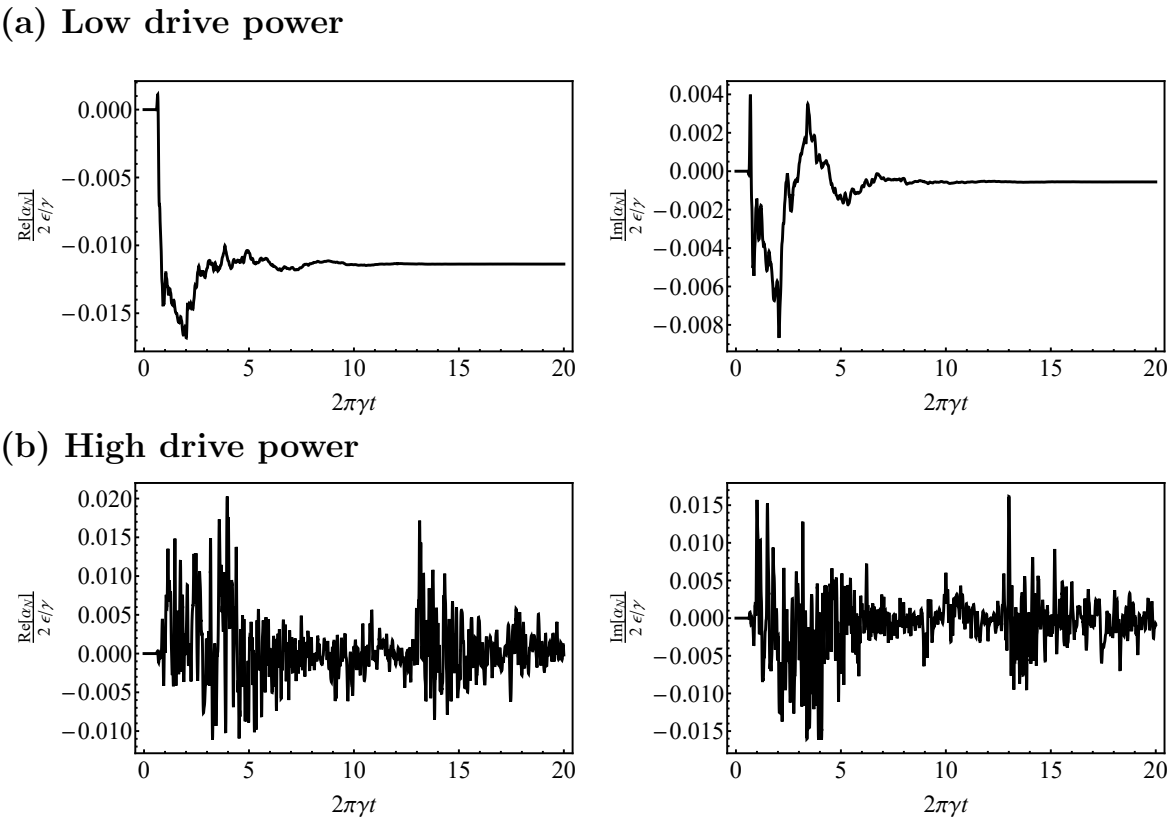

Figure 6.7. **Quasi-classical time evolution**. The time evolution of the mean field α_N is determined at (a) low drive power, and (b) high drive power. At low drive power, α_N approaches its long-time limit at $2\pi\gamma t \approx 10$. At high drive power, α_N is chaotic and exhibits an oscillatory behavior without any dominant period. Note that time averaging α_N yields a value close to zero, which leads to suppressed transmission at high drive power.

6.5.2. Quasi-classical chaotic state

For high drive power, the quasi-classical dynamics becomes chaotic, see fig. 6.7. This is one of the key differences between the current model and the driven-damped Dicke model discussed previously: the driven-damped Dicke model does not exhibit chaotic dynamics even at high power. This difference suggests that the higher transmon levels may play an

important role for the system to exhibit chaotic dynamics[12]. Moreover, once the system is in the chaotic state, the mean-field solution shows that higher transmon levels ($n \approx 5$) are occupied[13]. Due to the negative interaction strength U, the transition frequency between levels n and $n+1$ becomes nearly resonant with the drive frequency ω_d. This allows for significant interaction between the photons and the higher transmon levels. Note that similar (quasi-classical) chaotic dynamics has been predicted for a driven-dissipative Bose-Hubbard chain [37].

In the chaotic state, the mean fields α_j and β_j are not stationary in the long-time limit as shown in fig. 6.7(b). In this case, we take additional time averaging over a time interval that excludes any initial transient behavior.

6.5.3. Bistability

When varying the drive strength ϵ, the mean-field solution of the circuit-QED chain also exhibits bistability[14], see fig. 6.8. By increasing the drive strength beyond a critical value, an additional solution associated with the high-power chaotic state appears. When the system is in this high-power state, the transmission is strongly suppressed. This is exactly opposite to the optical bistability (fig. 6.5) shown for the driven-damped Dicke model, in which the higher-power state is associated with higher transmission. A look ahead at fig. 6.9 shows that the suppressed transmission agrees with the experimental result.

[12]A similar system is simulated using a much larger interaction strength U (hard-core boson limit) to mimic the two-level approximation. No chaotic dynamics is seen in that case.
[13]Nonetheless, the occupied levels remain within the cosine potential well.
[14]The interpretation of the mean-field bistability is discussed in section 6.4.2.

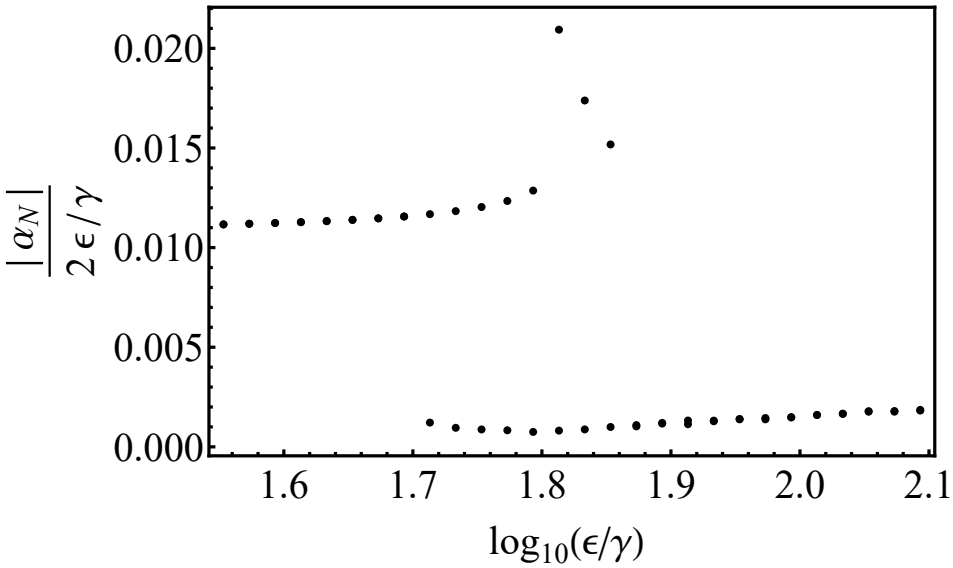

Figure 6.8. **Mean-field transmission as a function of the drive strength**. When the drive strength increases beyond a certain threshold, an additional solution appears as a result of the mean-field bistability. This additional solution is associated with strongly suppressed transmission.

6.6. Experimental observation

In the following, I will present the experimental result from Andrew Houck's lab. This includes the transmission and the estimated ADR in the bistable region. The result shows a rapid crossover between two metastable states.

6.6.1. Transmission

To observe physics beyond the low-power linear regime, the transmission is measured while the drive power varies over more than five orders of magnitude, see fig. 6.9(a). When the drive power reaches a certain threshold, a sudden change in transmission is observed. The transmission resonance peaks split, and abruptly give way to a region of strongly suppressed

transmission. In this high-power region, all resonance peaks disappear. These features – the dramatic suppression of transmission and the disappearance of all resonance peaks – are also qualitatively consistent with the theoretical prediction [fig. 6.9(b)] discussed in section 6.5. This sharp change in transmission beyond a certain drive power threshold indicates a dissipative phase transition.

The transition between the low- and high-power phases is thoroughly explored by measuring the transmission at a single drive frequency while sweeping the drive power either from low to high [fig. 6.9(c)] or from high to low [fig. 6.9(d)]. This reveals a significant region exhibiting hysteresis as shown in fig. 6.9(e).

6.6.2. Switching and ADR estimation

As explained in section 6.1, the relevant quantity to identify a dissipative phase transition is the ADR. An approximation for the ADR can be extracted by single-shot measurements of the dynamics in the bistable/hysteresis region as follows. Single-shot time traces of the homodyne signal are recorded with constant drive frequency and power. The measurements show that the system undergoes switching between two metastable states on timescales large compared to system-intrinsic timescales [fig. 6.10(a)]. Along a single-shot trajectory, the system state is labeled as either ρ_1 (①) or ρ_2 (②) and the characteristic switching times can be extracted. The statistics acquired from many single-shot trajectories allow us to obtain average rates $\gamma_{1\to2}$, $\gamma_{2\to1}$ for the switching between the two metastable states ρ_1 and ρ_2, respectively.

The extracted switching rates let us estimate the asymptotic decay rate by adopting a simplified rate-equation model [142] describing the probabilities p_1 and p_2 for the system

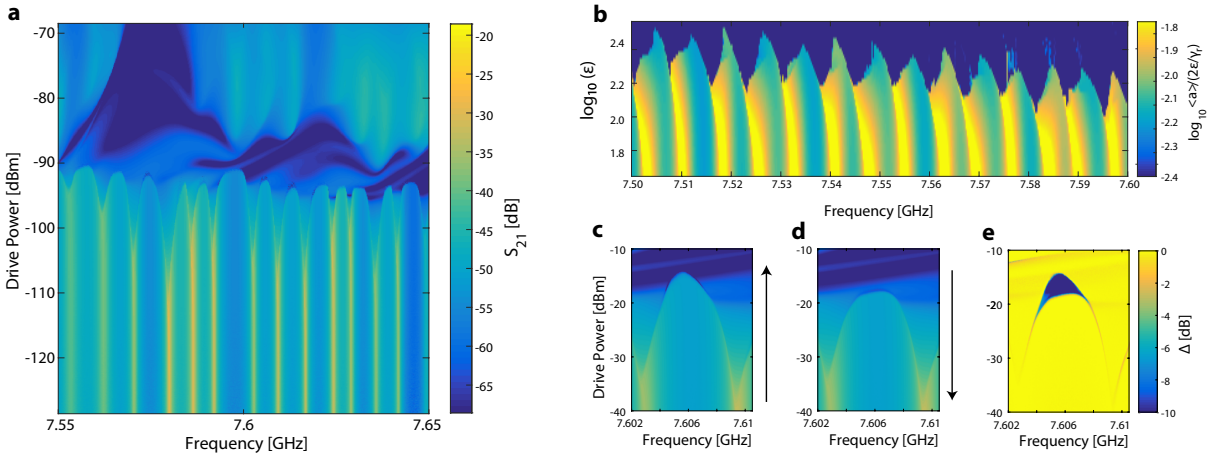

Figure 6.9. **Transmission exhibiting an abrupt transition to a suppressed transmission regime and a region of hysteresis**. (a) Dispersively shifted transmission peaks show nonlinear splitting at increased power and give rise to a region of strongly suppressed transmission without resonance peaks. Here, the data is acquired using constant power, frequency sweeps. (b) Corresponding quasi-classical mean-field prediction showing features qualitatively consistent with the experiment. (c) Zoom into one lobe, showing the sharp transition to a state of suppressed transmission as the drive power is swept from low to high power at constant frequency. (d) Same region as in (c), but now sweeping power in the opposite direction (high to low) over the same time period as (c). The transition now occurs along a down-shifted curve. (e) Subtraction of the data shown in (c) and (d) uncovers the large region of hysteresis.

to be in metastable state ρ_1 or ρ_2 (see appendix A.7 for details):

$$\frac{\mathrm{d}}{\mathrm{d}t}\begin{pmatrix} p_1 \\ p_2 \end{pmatrix} = \begin{pmatrix} -\gamma_{1\to 2} & \gamma_{2\to 1} \\ \gamma_{1\to 2} & -\gamma_{2\to 1} \end{pmatrix}\begin{pmatrix} p_1 \\ p_2 \end{pmatrix}. \tag{6.28}$$

Diagonalization of this system yields the eigenstates $\rho_s = (\gamma_{2\to 1}\rho_1 + \gamma_{1\to 2}\rho_2)/(\gamma_{1\to 2} + \gamma_{2\to 1})$ and $\rho_{\mathrm{ADR}} = \gamma_{2\to 1}\rho_1 - \gamma_{1\to 2}\rho_2$ with corresponding eigenvalues zero and $\lambda_{\mathrm{ADR}} = -(\gamma_{1\to 2} + \gamma_{2\to 1})$. The ADR can thus be approximated by the sum of the two switching rates, i.e. $\mathrm{ADR} = \gamma_{1\to 2} + \gamma_{2\to 1}$.

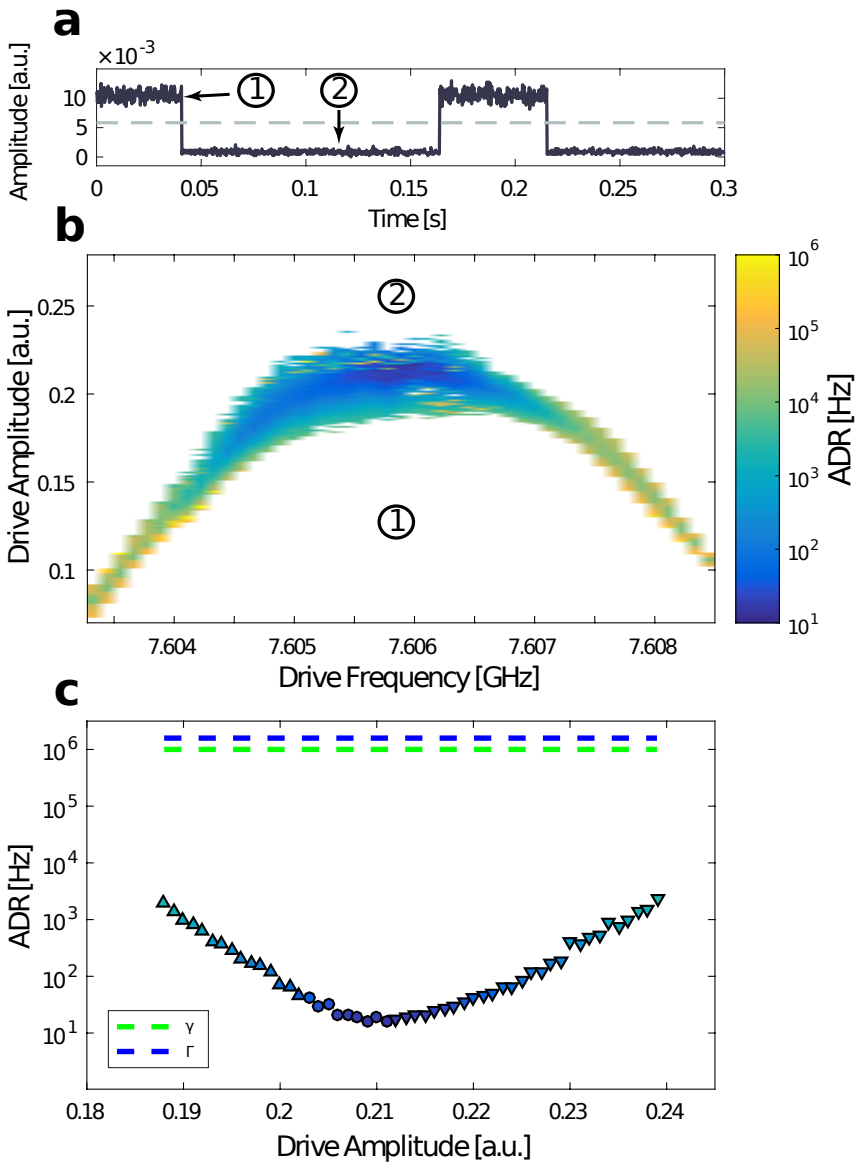

Figure 6.10. **Asymptotic decay rate in the bistable region**. (a) Single-shot time trace of the homodyne phase in the hysteretic region. Data show stochastic switching between two distinct metastable states ① and ② on timescales vastly exceeding those intrinsic to the system. (b) The ADR obtained from the sum of the characteristic switching times, $\gamma_{1\to2} + \gamma_{2\to1}$, as a function of drive frequency and power. (c) The ADR for a drive frequency of 7.5059 GHz is plotted as a function of power. The photon decay rate γ and qubit relaxation rate Γ are included for reference.

6.6.3. Observation of dissipative phase transition

The ADR shown in fig. 6.10(b) and (c) reaches a minimum value as low as $\sim 10\,\mathrm{Hz}$, which corresponds to the metastable-state lifetimes on the order of $0.1\,\mathrm{s}$. This is remarkable given that the timescales set by the photon decay and the qubit relaxation are on the order of μs. This vast timescale discrepancy of five orders of magnitudes shows strong evidence for the onset of a dissipative phase transition. As explained in section 6.1, it is only in the thermodynamic limit that the ADR vanishes and the crossover between the two metastable states turns into a discontinuous dissipative phase transition.

CHAPTER 7

Conclusions and outlook

I have studied nonequilibrium many-body physics with circuit-QED lattices from multiple aspects, ranging from developing a resummation scheme suitable for these lattices to analyzing the many-body physics observed in an experimental realization. These work have demonstrated the promising potential of using circuit-QED lattices to advance our understanding of nonequilibrium many-body physics. In the following, I will summarize the important results presented and propose some directions to extend the current work.

7.1. Conclusions

In chapter 4, I demonstrated a perturbation theory with resummation scheme suitable for nonequilibrium quantum systems. I first developed a non-degenerate perturbation theory based on the quantum master equation. I then extended this theory to include resummation of an infinite subset of perturbative corrections. I have formulated the scheme at a general level, emphasizing that is not limited to a particular open quantum system, but benefits a variety of questions arising in Markovian quantum systems amenable to perturbative treatment. For the examples I have investigated, I find that the series resummation can significantly improve the accuracy of the perturbative treatment.

I have applied perturbation theory including resummation to the open Jaynes-Cummings lattice, and introduced a diagrammatic representation systematically organizing the contributing terms. There is a good agreement with exact results obtained by extensive

quantum trajectory simulations. The perturbative treatment is capable of predicting steady-state observables for finite and infinite Jaynes-Cummings lattices with different lattice geometries, thus including settings not be easily accessible by other methods. The capability of obtaining reliable results beyond exactly solvable limits of open quantum lattices is particularly promising as a method for validating experimental data obtained with driven and damped circuit-QED lattices.

In chapter 5, we discussed Scanning Defect Microscopy as a new tool probing resonator lattices. The idea of this technique is to use a movable dielectric probe that can reveal local photon occupations via frequency shifting. For a resonator array, I have developed a theoretical model to predict the change in transmission spectrum as a function of the probe's position. This theoretical model motivates our collaborative development of scanning defect microscopy with Andrew Houck's group. This technique will provide key insight into local properties of these lattices with interaction, and serve as an important tool for the study of nonequilibrium phase transitions in the future.

In chapter 6, I presented the theoretical analysis of a one-dimensional circuit-QED chain built in Andrew Houck's lab. Using a suitable model together with the quasi-classical mean-field treatment, I predicted the chain to exhibit critical behavior with increasing drive power and undergo chaotic dynamics at high power. This theoretical prediction is consistent with the experimental measurement, and reveals novel many-body phenomena which are not known in previous studies of circuit-QED lattices. These theoretical and experimental results show a rapid crossover between two metastable states, which is a strong evidence for the onset of a dissipative phase transition. This work also demonstrates the

potential for circuit-QED lattices as a controllable platform gaining a deeper understanding of nonequilibrium many-body physics.

7.2. Further studies

7.2.1. Further studies based on resummation

The resummation scheme demonstrated in chapter 4 is useful in future studies of nonequilibrium many-body physics. For instance, the driven-damped Dicke model (section 6.4) is an ideal candidate to apply the resummation scheme. I have predicted a critical behavior when increasing the drive power beyond a certain threshold (section 6.4.2). As usual, the critical behavior cannot be captured by standard perturbative treatment. It is an interesting question whether the proposed resummation scheme sheds light on the critical behavior. In particular, it would be extremely useful if one could identify a correspondence between certain resummation diagrams and the critical behavior.

Another important and related project will be to apply the resummation scheme to systems with known mean-field solutions. One popular type of mean-field treatment for lattice models is to decouple interaction terms between lattice sites. This type of mean-field treatment preserves the on-site "quantumness" while largely reducing the computational cost. It is expected that the mean-field treatment becomes exact when the coordination number N_C goes to infinity[1]. For a specific system, it would be particularly helpful if re-summing all leading order corrections of $1/N_C$ was possible. This resummation, for example, will further our understanding on whether mean-field features are preserved in lattices with finite N_C.

[1]For open quantum systems, the general proof of this statement is not known to the best of my knowledge.

7.2.2. Scanning defect microscopy for interacting photons

For scanning defect microscopy, an important next step is to extend the technique to circuits involving interacting photons. This requires theory prediction of how the transmission signal will be affected by the dielectric probe in the interacting case. As in the non-interacting case, we may be able to follow a strategy to investigate perturbatively how a small shift in resonator frequency modifies the resonance frequencies.

I anticipate two major challenges. First of all, a perturbative study usually requires a comprehensive understanding of the unperturbed system. This, however, is exactly what we want to explore by using the scanning defect microscopy. Thus theoretical predictions for the "unperturbed" circuit behavior are already rather limited. Moreover, for the resonator array, there is a fortunate one-to-one correspondence between array eigenmodes and transmission resonance peaks. Such a simple relation is not available to the best of my knowledge for systems with interacting photons. It is thus much harder to relate the change in transmission to the expectation values or state properties of the unperturbed system.

Given these challenges, one approach is to first study simple systems in the hope that the result will provide insight into more complicated circuits. One ideal candidate is the open Jaynes-Cummings model. This model allows relatively easy access to its steady state through numerics. Experimentalists also have excellent control over the circuit realizing this model, meaning that theoretical predictions can be tested rather easily. Moreover, this model is the unit cell of the driven-damped Jaynes-Cummings lattice. Hence, findings for this simple model may be applicable (with appropriate modification) to the lattice.

7.2.3. Further studies of the one-dimensional circuit-QED chain

The one-dimensional circuit-QED chain discussed in chapter 6 exhibits a dissipative phase transition. This inspires further theoretical studies. For instance, it is important to better understand the quantum nature (including the switching mechanism) of the system since the mean-field result can be exactly reproduced by a classical model. Moreover, the high-power state demonstrates chaotic behavior in the mean-field prediction. The origin of this behavior is not yet well understood. Furthermore, an extension to other realistic parameter regimes may reveal phenomena that are not seen in the current setup. For example, in the weak-hopping limit (single-site limit), the system does not exhibit chaotic dynamics even for high drive power. Investigating the effect of the hopping rate κ is thus fascinating. One interesting equation is whether there is a critical hopping rate to observe the chaotic behavior.

References

[1] M. C. Gutzwiller, *Effect of correlation on the ferromagnetism of transition metals,* Phys. Rev. Lett. **10**, 159 (1963).

[2] J. Hubbard, *Electron correlations in narrow energy bands,* Proc. R. Soc. A Math. Phys. Eng. Sci. **276**, 238 (1963).

[3] J. Hubbard, *Electron correlations in narrow energy bands. II. the degenerate band case,* Proc. R. Soc. A Math. Phys. Eng. Sci. **277**, 237 (1964).

[4] M. P. A. Fisher, P. B. Weichman, G. Grinstein, and D. S. Fisher, *Boson localization and the superfluid-insulator transition,* Phys. Rev. B **40**, 546 (1989).

[5] W. Krauth, M. Caffarel, and J.-P. Bouchaud, *Gutzwiller wave function for a model of strongly interacting bosons,* Phys. Rev. B **45**, 3137 (1992).

[6] R. Orbach, *Linear antiferromagnetic chain with anisotropic coupling,* Phys. Rev. **112**, 309 (1958).

[7] P. Anderson, *Resonating valence bonds: A new kind of insulator?* Mater. Res. Bull. **8**, 153 (1973).

[8] S. Takei and Y. B. Kim, *Nonequilibrium-induced metal-superconductor quantum phase transition in graphene,* Phys. Rev. B **78**, 165401 (2008).

[9] N. Sedlmayr, J. Ren, F. Gebhard, and J. Sirker, *Closed and open system dynamics in a fermionic chain with a microscopically specified bath: Relaxation and thermalization,* Phys. Rev. Lett. **110**, 100406 (2013).

[10] W.-R. Lee and K. Park, *Dielectric breakdown via emergent nonequilibrium steady states of the electric-field-driven Mott insulator,* Phys. Rev. B **89**, 205126 (2014).

[11] I. Carusotto, D. Gerace, H. E. Tureci, S. De Liberato, C. Ciuti, and A. Imamoğlu, *Fermionized photons in an array of driven dissipative nonlinear cavities,* Phys. Rev. Lett. **103**, 033601 (2009).

[12] T. Ozawa and I. Carusotto, *Anomalous and quantum Hall effects in lossy photonic lattices,* Phys. Rev. Lett. **112**, 133902 (2014).

[13] M. Hafezi, *Measuring topological invariants in photonic systems,* Phys. Rev. Lett. **112**, 210405 (2014).

[14] J. Raftery, D. Sadri, S. Schmidt, H. E. Türeci, and A. A. Houck, *Observation of a dissipation-induced classical to quantum transition,* Phys. Rev. X **4**, 031043 (2014).

[15] E. Kapit, M. Hafezi, and S. H. Simon, *Induced self-stabilization in fractional quantum Hall states of light,* Phys. Rev. X **4**, 031039 (2014).

[16] V. Peano, C. Brendel, M. Schmidt, and F. Marquardt, *Topological phases of sound and light,* Phys. Rev. X **5**, 031011 (2015).

[17] T. Gao, E. Estrecho, K. Bliokh, T. Liew, M. Fraser, S. Brodbeck, M. Kamp, C. Schneider, S. Höfling, Y. Yamamoto, *et al.*, *Observation of non-Hermitian degeneracies in a chaotic exciton-polariton billiard,* Nature **526**, 554 (2015).

[18] M. H. Devoret and R. J. Schoelkopf, *Superconducting circuits for quantum information: an outlook,* Science **339**, 1169 (2013).

[19] S. Boixo, T. F. Rønnow, S. V. Isakov, Z. Wang, D. Wecker, D. A. Lidar, J. M. Martinis, and M. Troyer, *Evidence for quantum annealing with more than one hundred qubits,* Nature Phys. **10**, 218 (2014).

[20] M. Schuld, I. Sinayskiy, and F. Petruccione, *The quest for a quantum neural network,* Quantum Inf. Process. **13**, 2567 (2014).

[21] D. S. Pavlichin and H. Mabuchi, *Photonic circuits for iterative decoding of a class of low-density parity-check codes,* New J. Phys. **16**, 105017 (2014).

[22] N. H. Nickerson, J. F. Fitzsimons, and S. C. Benjamin, *Freely scalable quantum technologies using cells of 5-to-50 qubits with very lossy and noisy photonic links,* Phys. Rev. X **4**, 041041 (2014).

[23] C. Aron, M. Kulkarni, and H. E. Türeci, *Steady-state entanglement of spatially separated qubits via quantum bath engineering,* Phys. Rev. A **90**, 062305 (2014).

[24] K. Baumann, C. Guerlin, F. Brennecke, and T. Esslinger, *Dicke quantum phase transition with a superfluid gas in an optical cavity,* Nature **464**, 1301 (2010).

[25] M. Fitzpatrick, N. M. Sundaresan, A. C. Y. Li, J. Koch, and A. A. Houck, *Observation of a dissipative phase transition in a one-dimensional circuit QED lattice,* arXiv:1607.06895 .

[26] D. Nagy, G. Szirmai, and P. Domokos, *Critical exponent of a quantum-noise-driven phase transition: The open-system dicke model,* Phys. Rev. A **84**, 043637 (2011).

[27] T. Grujic, S. Clark, D. Jaksch, and D. Angelakis, *Non-equilibrium many-body effects in driven nonlinear resonator arrays,* New J. Phys. **14**, 103025 (2012).

[28] T. E. Lee, H. Häffner, and M. C. Cross, *Collective quantum jumps of Rydberg atoms,* Phys. Rev. Lett. **108**, 023602 (2012).

[29] E. M. Kessler, G. Giedke, A. Imamoglu, S. F. Yelin, M. D. Lukin, and J. I. Cirac, *Dissipative phase transition in a central spin system,* Phys. Rev. A **86**, 012116 (2012).

[30] F. Nissen, S. , M. Biondi, G. Blatter, H. E. Türeci, and J. Keeling, *Nonequilibrium dynamics of coupled qubit-cavity arrays,* Phys. Rev. Lett. **108**, 233603 (2012).

[31] G. Kulaitis, F. Krüger, F. Nissen, and J. Keeling, *Disordered driven coupled cavity arrays: Nonequilibrium stochastic mean-field theory,* Phys. Rev. A **87**, 013840 (2013).

[32] L. M. Sieberer, S. D. Huber, E. Altman, and S. Diehl, *Dynamical critical phenomena in driven-dissipative systems,* Phys. Rev. Lett. **110**, 195301 (2013).

[33] L. M. Sieberer, S. D. Huber, E. Altman, and S. Diehl, *Nonequilibrium functional renormalization for driven-dissipative Bose-Einstein condensation,* Phys. Rev. B **89**, 134310 (2014).

[34] J. Jin, D. Rossini, M. Leib, M. J. Hartmann, and R. Fazio, *Steady-state phase diagram of a driven QED-cavity array with cross-Kerr nonlinearities,* Phys. Rev. A **90**, 023827 (2014).

[35] A. Le Boité, G. Orso, and C. Ciuti, *Bose-Hubbard model: Relation between driven-dissipative steady states and equilibrium quantum phases,* Phys. Rev. A **90**, 063821 (2014).

[36] J. Klinder, H. Keßler, M. Wolke, L. Mathey, and A. Hemmerich, *Dynamical phase transition in the open Dicke model,* Proc. Natl. Acad. Sci. U.S.A. **112**, 3290 (2015).

[37] U. Naether, F. Quijandría, J. J. García-Ripoll, and D. Zueco, *Stationary discrete solitons in a driven dissipative Bose-Hubbard chain,* Phys. Rev. A **91**, 033823 (2015).

[38] J. Marino and S. Diehl, *Driven Markovian quantum criticality,* Phys. Rev. Lett. **116**, 070407 (2016).

[39] J. M. Zeuner, M. C. Rechtsman, Y. Plotnik, Y. Lumer, S. Nolte, M. S. Rudner, M. Segev, and A. Szameit, *Observation of a topological transition in the bulk of a*

non-Hermitian system, Phys. Rev. Lett. **115**, 040402 (2015).

[40] V. Fernández-Hurtado, J. Mur-Petit, J. J. García-Ripoll, and R. A. Molina, *Lattice scars: surviving in an open discrete billiard,* New J. Phys. **16**, 035005 (2014).

[41] H. Breuer and F. Petruccione, *The Theory Of Open Quantum Systems* (Oxford University Press, 2002).

[42] R. Alicki, General theory and applications to unstable particles, in *Quantum dynamical semigroups and applications* (Springer, 2007).

[43] H.-J. Briegel and B.-G. Englert, *Quantum optical master equations: The use of damping bases,* Phys. Rev. A **47**, 3311 (1993).

[44] J. M. Torres, *Closed-form solution of Lindblad master equations without gain,* Phys. Rev. A **89**, 052133 (2014).

[45] M. B. Plenio and P. L. Knight, *The quantum-jump approach to dissipative dynamics in quantum optics,* Rev. Mod. Phys. **70**, 101 (1998).

[46] F. Verstraete, J. J. García-Ripoll, and J. I. Cirac, *Matrix product density operators: Simulation of finite-temperature and dissipative systems,* Phys. Rev. Lett. **93**, 207204 (2004).

[47] M. Zwolak and G. Vidal, *Mixed-state dynamics in one-dimensional quantum lattice systems: A time-dependent superoperator renormalization algorithm,* Phys. Rev. Lett. **93**, 207205 (2004).

[48] P. Degenfeld-Schonburg and M. J. Hartmann, *Self-consistent projection operator theory for quantum many-body systems,* Phys. Rev. B **89**, 245108 (2014).

[49] H. Weimer, *Variational principle for steady states of dissipative quantum many-body systems,* Phys. Rev. Lett. **114**, 040402 (2015).

[50] J. Cui, J. I. Cirac, and M. C. Bañuls, *Variational matrix product operators for the steady state of dissipative quantum systems,* Phys. Rev. Lett. **114**, 220601 (2015).

[51] M. Hafezi, P. Adhikari, and J. M. Taylor, *Chemical potential for light by parametric coupling,* Phys. Rev. B **92**, 174305 (2015).

[52] D. L. Underwood, W. E. Shanks, J. Koch, and A. A. Houck, *Low-disorder microwave cavity lattices for quantum simulation with photons,* Phys. Rev. A **86**, 023837 (2012).

[53] A. A. Houck, H. E. Türeci, and J. Koch, *On-chip quantum simulation with superconducting circuits,* Nature Phys. **8**, 292 (2012).

[54] S. Schmidt and J. Koch, *Circuit QED lattices: towards quantum simulation with superconducting circuits,* Ann. Phys. (Berlin) **525**, 395 (2013).

[55] D. L. Underwood, W. E. Shanks, A. C. Y. Li, L. Ateshian, J. Koch, and A. A. Houck, *Imaging photon lattice states by scanning defect microscopy,* Phys. Rev. X **6**, 021044 (2016).

[56] I. Chiorescu, P. Bertet, K. Semba, Y. Nakamura, C. Harmans, and J. Mooij, *Coherent dynamics of a flux qubit coupled to a harmonic oscillator,* Nature **431**, 159 (2004).

[57] J. Johansson, S. Saito, T. Meno, H. Nakano, M. Ueda, K. Semba, and H. Takayanagi, *Vacuum Rabi oscillations in a macroscopic superconducting qubit LC oscillator system,* Phys. Rev. Lett. **96**, 127006 (2006).

[58] A. Wallraff, D. I. Schuster, A. Blais, L. Frunzio, R.-S. Huang, J. Majer, S. Kumar, S. M. Girvin, and R. J. Schoelkopf, *Strong coupling of a single photon to a superconducting qubit using circuit quantum electrodynamics,* Nature **431**, 162 (2004).

[59] T. Niemczyk, F. Deppe, H. Huebl, E. Menzel, F. Hocke, M. Schwarz, J. Garcia-Ripoll, D. Zueco, T. Hümmer, E. Solano, *et al.*, *Circuit quantum electrodynamics in the ultrastrong-coupling regime,* Nature Phys. **6**, 772 (2010).

[60] D. I. Schuster, *Circuit Quantum Electrodynamics*, Ph.D. thesis, Yale University (2007).

[61] S. M. Girvin, Circuit QED: superconducting qubits coupled to microwave photons, in *Quantum Machines: Measurement and Control of Engineered Quantum Systems*, edited by M. Devoret, B. Huard, R. Schoelkopf, and L. F. Cugliandolo (Oxford University Press, 2014).

[62] M. H. Devoret, *Quantum fluctuations in electrical circuits,* Les Houches, Session LXIII **7** (1995).

[63] J. Koch, A. A. Houck, K. L. Hur, and S. M. Girvin, *Time-reversal-symmetry breaking in circuit-QED-based photon lattices,* Phys. Rev. A **82**, 043811 (2010).

[64] V. Bouchiat, D. Vion, P. Joyez, D. Esteve, and M. H. Devoret, *Quantum coherence with a single Cooper pair,* Phys. Scripta **1998**, 165 (1998).

[65] Y. Nakamura, Y. A. Pashkin, and J. S. Tsai, *Coherent control of macroscopic quantum states in a single-Cooper-pair box,* Nature **398**, 786 (1999).

[66] J. R. Friedman, V. Patel, W. Chen, S. Tolpygo, and J. E. Lukens, *Quantum superposition of distinct macroscopic states,* Nature **406**, 43 (2000).

[67] C. H. Van der Wal, A. Ter Haar, F. Wilhelm, R. Schouten, C. Harmans, T. Orlando, S. Lloyd, and J. Mooij, *Quantum superposition of macroscopic persistent-current states,* Science **290**, 773 (2000).

[68] J. M. Martinis, S. Nam, J. Aumentado, and C. Urbina, *Rabi oscillations in a large Josephson-junction qubit,* Phys. Rev. Lett. **89**, 117901 (2002).

[69] J. Koch, T. M. Yu, J. Gambetta, A. A. Houck, D. I. Schuster, J. Majer, A. Blais, M. H. Devoret, S. M. Girvin, and R. J. Schoelkopf, *Charge-insensitive qubit design derived from the Cooper pair box,* Phys. Rev. A **76**, 042319 (2007).

[70] J. A. Schreier, A. A. Houck, J. Koch, D. I. Schuster, B. R. Johnson, J. M. Chow, J. M. Gambetta, J. Majer, L. Frunzio, M. H. Devoret, S. M. Girvin, and R. J. Schoelkopf, *Suppressing charge noise decoherence in superconducting charge qubits,* Phys. Rev. B **77**, 180502 (2008).

[71] V. E. Manucharyan, J. Koch, L. I. Glazman, and M. H. Devoret, *Fluxonium: Single Cooper-pair circuit free of charge offsets,* Science **326**, 113 (2009).

[72] J. Koch, V. Manucharyan, M. H. Devoret, and L. I. Glazman, *Charging effects in the inductively shunted Josephson junction,* Phys. Rev. Lett. **103**, 217004 (2009).

[73] E. T. Jaynes and F. W. Cummings, *Comparison of quantum and semiclassical radiation theories with application to the beam maser,* Proceedings of the IEEE **51**, 89 (1963).

[74] A. D. Greentree, C. Tahan, J. H. Cole, and L. C. Hollenberg, *Quantum phase transitions of light,* Nature Phys. **2**, 856 (2006).

[75] J. Koch and K. Le Hur, *Superfluid-mott-insulator transition of light in the Jaynes-Cummings lattice,* Phys. Rev. A **80**, 023811 (2009).

[76] L. S. Bishop, *Circuit Quantum Electrodynamics*, Ph.D. thesis, Yale University (2010).

[77] A. J. Leggett, S. Chakravarty, A. T. Dorsey, M. P. A. Fisher, A. Garg, and W. Zwerger, *Dynamics of the dissipative two-state system,* Rev. Mod. Phys. **59**, 1

(1987).

[78] G. Lindblad, *Completely positive maps and entropy inequalities,* Comm. Math. Phys. **40**, 147 (1975).

[79] V. Gorini, A. Kossakowski, and E. C. G. Sudarshan, *Completely positive dynamical semigroups of N-level systems,* J. Math. Phys. **17**, 821 (1976).

[80] D. Petz, *Monotone metrics on matrix spaces,* Linear Algebra Appl. **244**, 81 (1996).

[81] D. S. Bernstein, *Matrix Mathematics: Theory, Facts, and Formulas* (Princeton University Press, 2009).

[82] J. M. Fink, A. Dombi, A. Vukics, A. Wallraff, and P. Domokos, *Observation of the photon-blockade breakdown phase transition,* arXiv:1607.04892 .

[83] B. Kraus, H. P. Büchler, S. Diehl, A. Kantian, A. Micheli, and P. Zoller, *Preparation of entangled states by quantum Markov processes,* Phys. Rev. A **78**, 042307 (2008).

[84] E. B. Davies, *Quantum stochastic processes II,* Commun. Math. Phys. **19**, 83 (1970).

[85] H. Spohn, *Approach to equilibrium for completely positive dynamical semigroups of n-level systems,* Rep. Math. Phys **10**, 189 (1976).

[86] T. Prosen, *Third quantization: a general method to solve master equations for quadratic open fermi systems,* New J. Phys. **10**, 043026 (2008).

[87] T. Prosen and T. H. Seligman, *Quantization over boson operator spaces,* J. Phys. A: Math. Theor. **43**, 392004 (2010).

[88] A. A. Dzhioev and D. S. Kosov, *Super-fermion representation of quantum kinetic equations for the electron transport problem,* J. Chem. Phys. **134**, 044121 (2011).

[89] K. Lendi, N-level systems and applications to spectroscopy, in *Quantum dynamical semigroups and applications* (Springer, 2007).

[90] C. Ates, B. Olmos, J. P. Garrahan, and I. Lesanovsky, *Dynamical phases and intermittency of the dissipative quantum Ising model,* Phys. Rev. A **85**, 043620 (2012).

[91] C. Joshi, F. Nissen, and J. Keeling, *Quantum correlations in the one-dimensional driven dissipative XY model,* Phys. Rev. A **88**, 063835 (2013).

[92] M. Knap, E. Arrigoni, W. von der Linden, and J. H. Cole, *Emission characteristics of laser-driven dissipative coupled-cavity systems,* Phys. Rev. A **83**, 023821 (2011).

[93] A. Nunnenkamp, J. Koch, and S. M. Girvin, *Synthetic gauge fields and homodyne transmission in Jaynes-Cummings lattices,* New J. Phys. **13**, 095008 (2011).

[94] R. M. Noack and S. R. Manmana, *Diagonalization- and numerical renormalization-group-based methods for interacting quantum systems,* AIP Conf. Proc. **789**, 93 (2005).

[95] S. Yamada, T. Kano, M. Machida, T. Imamura, Y. Ohashi, and H. Matsumoto, *Ultra large-scale exact-diagonalization for confined fermion-Hubbard model on the earth simulator exploration of superfluidity in confined strongly-correlated systems,* Journal of the Earth Simulator **7**, 23 (2007).

[96] J. Dalibard, Y. Castin, and K. Mølmer, *Wave-function approach to dissipative processes in quantum optics,* Phys. Rev. Lett. **68**, 580 (1992).

[97] C. W. Gardiner, A. S. Parkins, and P. Zoller, *Wave-function quantum stochastic differential equations and quantum-jump simulation methods,* Phys. Rev. A **46**, 4363 (1992).

[98] M. J. Hartmann, J. Prior, S. R. Clark, and M. B. Plenio, *Density matrix renormalization group in the Heisenberg picture,* Phys. Rev. Lett. **102**, 057202 (2009).

[99] T. Prosen and M. Znidari, *Matrix product simulations of non-equilibrium steady states of quantum spin chains,* J. Stat. Mech. Theor. Exp. **2009**, P02035 (2009).

[100] C. J. Wood, J. D. Biamonte, and D. G. Cory, *Tensor networks and graphical calculus for open quantum systems,* Quant. Inf. Comp. **15**, 0812 (2015).

[101] C. Flindt, T. Novotny, A. Braggio, M. Sassetti, and A.-P. Jauho, *Counting statistics of non-Markovian quantum stochastic processes,* Phys. Rev. Lett. **100**, 150601 (2008).

[102] C. Flindt, T. Novotny, A. Braggio, and A.-P. Jauho, *Counting statistics of transport through Coulomb blockade nanostructures: High-order cumulants and non-Markovian effects,* Phys. Rev. B **82**, 155407 (2010).

[103] X. X. Yi, C. Li, and J. C. Su, *Perturbative expansion for the master equation and its applications,* Phys. Rev. A **62**, 013819 (2000).

[104] C. H. Fleming and N. I. Cummings, *Accuracy of perturbative master equations,* Phys. Rev. E **83**, 031117 (2011).

[105] J. I. Cirac, R. Blatt, P. Zoller, and W. D. Phillips, *Laser cooling of trapped ions in a standing wave,* Phys. Rev. A **46**, 2668 (1992).

[106] F. Reiter and A. S. Sørensen, *Effective operator formalism for open quantum systems,* Phys. Rev. A **85**, 032111 (2012).

[107] E. M. Kessler, *Generalized Schrieffer-Wolff formalism for dissipative systems,* Phys. Rev. A **86**, 012126 (2012).

[108] Z. Cai and T. Barthel, *Algebraic versus exponential decoherence in dissipative many-particle systems,* Phys. Rev. Lett. **111**, 150403 (2013).

[109] A. C. Y. Li, F. Petruccione, and J. Koch, *Perturbative approach to Markovian open quantum systems,* Sci. Rep. **4**, 4887 (2014).

[110] A. C. Y. Li, F. Petruccione, and J. Koch, *Resummation for nonequilibrium perturbation theory and application to open quantum lattices,* Phys. Rev. X **6**, 021037 (2016).

[111] H. Spohn, *Kinetic equations from Hamiltonian dynamics: Markovian limits,* Rev. Mod. Phys. **52**, 569 (1980).

[112] T. E. Lee, H. Häffner, and M. C. Cross, *Antiferromagnetic phase transition in a nonequilibrium lattice of Rydberg atoms,* Phys. Rev. A **84**, 031402 (2011).

[113] F. Quijandra, U. Naether, D. Porras, J. J. Garca-Ripoll, and D. Zueco, *The Bose-Hubbard model with squeezed dissipation,* J. Phys. B **48**, 055302 (2015).

[114] T. Mori, *Exactness of the mean-field dynamics in optical cavity systems,* J. Stat. Mech. Theor. Exp. **2013**, P06005 (2013).

[115] A. Le Boité, G. Orso, and C. Ciuti, *Steady-state phases and tunneling-induced instabilities in the driven dissipative Bose-Hubbard model,* Phys. Rev. Lett. **110**, 233601 (2013).

[116] A. Hu, T. E. Lee, and C. W. Clark, *Spatial correlations of one-dimensional driven-dissipative systems of Rydberg atoms,* Phys. Rev. A **88**, 053627 (2013).

[117] A. Le Boité, G. Orso, and C. Ciuti, *Bose-Hubbard model: Relation between driven-dissipative steady states and equilibrium quantum phases,* Phys. Rev. A **90**, 063821 (2014).

[118] P. D. Drummond and D. F. Walls, *Quantum theory of optical bistability. I. Nonlinear polarisability model,* J. Phys. A **13**, 725 (1980).

[119] M. Biondi, G. Blatter, H. E. Türeci, and S. Schmidt, *Nonequilibrium phase diagram of the driven-dissipative photonic lattice,* arXiv:1611.00697 .

[120] F. Benatti, A. Nagy, and H. Narnhofer, *Asymptotic entanglement and Lindblad dynamics: a perturbative approach,* J. Phys. A **44**, 155303 (2011).

[121] E. del Valle and M. J. Hartmann, *Correlator expansion approach to stationary states of weakly coupled cavity arrays,* J. Phys. B: At. Mol. Opt. Phys. **46**, 224023 (2013).

[122] N. Moiseyev, *Non-Hermitian Quantum Mechanics* (Cambridge University Press, 2011).

[123] J. Řeháček, Z. Hradil, and M. Ježek, *Iterative algorithm for reconstruction of entangled states,* Phys. Rev. A **63**, 040303 (2001).

[124] A. Lvovsky, *Iterative maximum-likelihood reconstruction in quantum homodyne tomography,* J. Opt. B **6**, S556 (2004).

[125] R. Horn and C. Johnson, *Matrix Analysis* (Cambridge University Press, 1985).

[126] D. Chruściński and A. Kossakowski, *Feshbach projection formalism for open quantum systems,* Phys. Rev. Lett. **111**, 050402 (2013).

[127] P. Gill and W. Murray, *Newton-type methods for unconstrained and linearly constrained optimization,* Math. Prog. **7**, 311 (1974).

[128] H.-r. Fang and D. P. O'Leary, *Modified Cholesky algorithms: a catalog with new approaches,* Math. Prog. **115**, 319 (2008).

[129] L. S. Bishop, J. M. Chow, J. Koch, A. A. Houck, M. H. Devoret, E. Thuneberg, S. M. Girvin, and R. J. Schoelkopf, *Nonlinear response of the vacuum Rabi resonance,* Nature Phys. **5**, 105 (2009).

[130] G. Zhu, S. Schmidt, and J. Koch, *Dispersive regime of the JaynesCummings and Rabi lattice,* New J. Phys. **15**, 115002 (2013).

[131] J. Majer, J. Chow, J. Gambetta, J. Koch, B. Johnson, J. Schreier, L. Frunzio, D. Schuster, A. Houck, A. Wallraff, *et al.*, *Coupling superconducting qubits via a cavity bus,* Nature **449**, 443 (2007).

[132] A. F. Van Loo, A. Fedorov, K. Lalumière, B. C. Sanders, A. Blais, and A. Wallraff, *Photon-mediated interactions between distant artificial atoms,* Science **342**, 1494 (2013).

[133] D. Walls and G. J. Milburn, *Quantum Optics* (Springer, 2008).

[134] H. J. Carmichael, *Breakdown of photon blockade: A dissipative quantum phase transition in zero dimensions,* Phys. Rev. X **5**, 031028 (2015).

[135] J. Jin, A. Biella, O. Viyuela, L. Mazza, J. Keeling, R. Fazio, and D. Rossini, *Cluster mean-field approach to the steady-state phase diagram of dissipative spin systems,* Phys. Rev. X **6**, 031011 (2016).

[136] K. Macieszczak, M. Guţă, I. Lesanovsky, and J. P. Garrahan, *Towards a theory of metastability in open quantum dynamics,* Phys. Rev. Lett. **116**, 240404 (2016).

[137] R. H. Dicke, *Coherence in spontaneous radiation processes,* Phys. Rev. **93**, 99 (1954).

[138] T. Holstein and H. Primakoff, *Field dependence of the intrinsic domain magnetization of a ferromagnet,* Phys. Rev. **58**, 1098 (1940).

[139] M. Dykman and V. Smelyanskiy, *Quantum theory of transitions between stable states of a nonlinear oscillator interacting with a medium in a resonant field,* Zh. Eksp. Teor. Fiz **94**, 61 (1988).

[140] W. Casteels, F. Storme, A. Le Boité, and C. Ciuti, *Power laws in the dynamic hysteresis of quantum nonlinear photonic resonators,* Phys. Rev. A **93**, 033824 (2016).

[141] H. Gibbs, *Optical bistability: controlling light with light* (Academic Press, 1985).

[142] R. M. Wilson, K. W. Mahmud, A. Hu, A. V. Gorshkov, M. Hafezi, and M. Foss-Feig, *Collective phases of strongly interacting cavity photons,* Phys. Rev. A **94**, 033801 (2016).

[143] S. Campbell and C. Meyer, *Generalized Inverses Of Linear Transformations* (Dover Publications (New York), 1991) pp. 4–12.

[144] J. Barata and M. Hussein, *The Moore-Penrose pseudoinverse: A tutorial review of the theory,* Braz. J. Phys. **42**, 146 (2012).

[145] E. H. Moore, *On the reciprocal of the general algebraic matrix,* Bull. Amer. Math. Soc. **26**, 394 (1920).

[146] R. Penrose, *A generalized inverse for matrices,* Math. Proc. Cambridge Philos. Soc. **51**, 406 (1955).

APPENDIX A

Appendices

A.1. Review of the Moore-Penrose pseudoinverse

Here, a brief review of the definition and basic properties of the Moore-Penrose (MP) pseudoinverse are provided. The review closely follows refs. 143, 144. The notion of the MP pseudoinverse was introduced by E. H. Moore in 1920 [145] and then independently by R. Penrose in 1955 [146] to deal with matrices that have no inverse in the ordinary sense.

Before stating its formal definition, we motivate the MP pseudoinverse by the following simple consideration. The inverse A^{-1} of a matrix A is well-defined if and only if A is a non-singular square matrix. Even when a matrix is singular, however, we sometimes need to find a generalized inverse which resembles the normal inverse. (One such example, in fact, occurs in ordinary perturbation theory.) If A is a Hermitian square matrix, then there is a natural way for defining a pseudoinverse. First, factorize A in the form

$$A = U D U^{\dagger}, \tag{A.1}$$

where U is unitary and D is a diagonal matrix which consists of the eigenvalues of A. By inspection of D, a matrix D' is defined by taking the reciprocal of each non-zero diagonal element of D while leaving the zero elements unchanged. A generalized inverse A' can thus be defined as

$$A' = U D' U^{\dagger}. \tag{A.2}$$

If the square matrix A is not Hermitian, such as the superoperator $\mathbb{L}_0$, the procedure becomes more involved. Let us assume that A is diagonalizable such that

$$A = Y D Y^{-1}, \tag{A.3}$$

where Y is non-unitary and the diagonal matrix D holds the complex eigenvalues of A. It is tempting to define the generalized inverse A' in the same way as in eq. (A.2), i.e.,

$$A' = Y D' Y^{-1}. \tag{A.4}$$

However, this attempt to define a generalized inverse produces a major inconvenience. Recall that if A is invertible, we have $AA^{-1} = \mathbb{1} = A^{-1}A$ and, hence, both AA^{-1} and $a^{-1}A$ are Hermitian. Unfortunately, neither $A'A$ nor AA' are Hermitian when using eq. (A.4).

To establish a generalized inverse that does fulfill the mentioned Hermiticity property, recall that the singular value decomposition (SVD) provides an alternative to eq. (A.3) by relating a non-Hermitian matrix A to a diagonal matrix D in the following way:

$$A = U D V^{\dagger}, \tag{A.5}$$

where U and V are unitary matrices. [Note: the diagonal matrices in eqs. (A.3) and (A.5) are generally not the same.] Similar to the treatment of Hermitian singular matrices, the generalized inverse or pseudoinverse, $A^{\leftarrow 1}$, for a non-Hermitian matrix A is defined as

$$A^{\leftarrow 1} = V D^{\leftarrow 1} U^{\dagger}. \tag{A.6}$$

Here, $D^{\leftarrow 1}$ is again obtained by taking the inverse of the non-zero diagonal elements of D.

There are three advantages in using $A^{\leftarrow 1}$ [eq. (A.6)] instead of A' [eq. (A.4)]. First, $A^{\leftarrow 1}A$ and $AA^{\leftarrow 1}$ are now Hermitian projectors. Second, the SVD and thus also the pseudoinverse $A^{\leftarrow 1}$ can be computed efficiently. Third, we can easily generalize the pseudoinverse $A^{\leftarrow 1}$ to cases where A cannot be diagonalized or is not a square matrix

since the SVD is defined for any complex-valued matrix. The pseudoinverse defined in eq. (A.6) is called the MP pseudoinverse.

Finally, we prove one property of the MP pseudoinverse which we use in the Methods section of the main text. Our claim is that

$$AA^{\leftarrow 1} = P_A, \tag{A.7}$$

where P_A is the orthogonal projector onto the range of A. By using the definition of $A^{\leftarrow 1}$ in eq. (A.6), we obtain

$$AA^{\leftarrow 1}A = A. \tag{A.8}$$

This implies $(AA^{\leftarrow 1})^2 = AA^{\leftarrow 1}$, i.e. $AA^{\leftarrow 1}$ is a projector. Likewise, we infer from eq. (A.6) that

$$AA^{\leftarrow 1} = (AA^{\leftarrow 1})^\dagger \tag{A.9}$$

which means $AA^{\leftarrow 1}$ is Hermitian. Since a projector is Hermitian if and only if it is an orthogonal projector, $AA^{\leftarrow 1}$ is an orthogonal projector. Let us denote the range of A by $\mathrm{Ran}\,(A)$. Then, eq. (A.8) immediately yields $\mathrm{Ran}\,(A) = \mathrm{Ran}\,(AA^{\leftarrow 1}A)$. Using the fact that composite maps decrease the range according to $\mathrm{Ran}\,(AB) \subseteq \mathrm{Ran}\,(A)$, we infer that

$$\mathrm{Ran}\,(A) \subseteq \mathrm{Ran}\left(AA^{\leftarrow 1}\right) \subseteq \mathrm{Ran}\,(A) \tag{A.10}$$

The above relation holds if and only if $\mathrm{Ran}\,(A) = \mathrm{Ran}\,(AA^{\leftarrow 1})$. Thus we have proven that $AA^{\leftarrow 1}$ is an orthogonal projector with the same range as A, i.e. $AA^{\leftarrow 1} = P_A$.

A.2. Derivation of perturbative corrections

We wish to prove that the expression of $\mathsf{u}_\mu^{(j)}$ in eq. (4.10), rewritten as

$$\left|\mathsf{u}_\mu^{(j)}\right) = \left(\mathbb{L}_0 - \lambda_\mu^{(0)}\right)^{\leftarrow 1} |f_{j\mu}) \,, \tag{A.11}$$

is indeed a solution to eq. (4.6), i.e., it satisfies

$$\left(\mathbb{L}_0 - \lambda_\mu^{(0)}\right) \left|\mathsf{u}_\mu^{(j)}\right) = |f_{j\mu}) \,, \tag{A.12}$$

where the operators $|f_{j\mu})$ are defined as $|f_{j\mu}) = -\mathbb{L}_1 \left|\mathsf{u}_\mu^{(j-1)}\right) + |\Delta_\mu^{(j)})$. Solving eq. (A.12) for $|\mathsf{u}_\mu^{(j)})$ is a standard linear algebra problem. The necessity for working with a pseudoinverse lies in the fact that $(\mathbb{L}_0 - \lambda_\mu^{(0)})$ is singular and non-Hermitian. This prevents us from using the ordinary inverse to solve for $|\mathsf{u}_\mu^{(j)})$. Here, we employ the Moore-Penrose pseudoinverse denoted by $^{\leftarrow 1}$. (A brief review of the pseudoinverse is given in appendix A.1.) While this choice is not unique, it is convenient since the Moore-Penrose pseudoinverse can be computed efficiently via singular value decomposition.

After plugging $|\mathsf{u}_\mu^{(j)})$ from eq. (A.11) into eq. (A.12), it is clear that the proof amounts to verifying that

$$\left(\mathbb{L}_0 - \lambda_\mu^{(0)}\right) \left(\mathbb{L}_0 - \lambda_\mu^{(0)}\right)^{\leftarrow 1} |f_{j\mu}) = |f_{j\mu}) \,. \tag{A.13}$$

Employing the defining properties of the Moore-Penrose pseudoinverse, one finds that the claim of eq. (A.13) can be written in the equivalent form

$$\mathbb{P}_{\mathbb{L}_0 - \lambda_\mu^{(0)}} \, |f_{j\mu}) = |f_{j\mu}) \,. \tag{A.14}$$

where $\mathbb{P}_{\mathbb{L}_0-\lambda_\mu^{(0)}}$ is the orthogonal projector onto the range of $(\mathbb{L}_0 - \lambda_\mu^{(0)})$. Since every projector acts as the identity on vectors from its range, eq. (A.14) holds if $|f_{j\mu})$ belongs to the range $\mathfrak{R}_\mu$ of $\mathbb{P}_{\mathbb{L}_0-\lambda_\mu^{(0)}}$. Furthermore, since $\mathbb{P}_{\mathbb{L}_0-\lambda_\mu^{(0)}}$ is an orthogonal projector, the range $\mathfrak{R}_\mu$ and the null space $\mathfrak{N}_\mu$ of $\mathbb{P}_{\mathbb{L}_0-\lambda_\mu^{(0)}}$ are orthogonal subspaces. This implies that $|f_{j\mu})$ belongs to $\mathfrak{R}_\mu$ if and only if $|f_{j\mu})$ is orthogonal to $\mathfrak{N}_\mu$. To see that $|f_{j\mu}) \perp \mathfrak{N}_\mu$, note that $(\breve{\mathsf{u}}_\mu^{(0)}|f_{j\mu}) = 0$ as a direct consequence of eq. (4.6). To prove that $|f_{j\mu}) \perp \mathfrak{N}_\mu$ we now simply make use of the fact that $\mathfrak{N}_\mu$ is spanned by the left eigenstate $(\breve{\mathsf{u}}_\mu^{(0)}| \leftrightarrow (\breve{\mathsf{u}}_\mu^{(0)})^\dagger$, i.e., $\mathfrak{N}_\mu = \mathrm{span}\{(\breve{\mathsf{u}}_\mu^{(0)}|\}$.

We verify the last statement as follows. Since $(\breve{\mathsf{u}}_\mu^{(0)}|$ is the left eigenstate of $\mathbb{L}_0$ with eigenvalue $\lambda_\mu^{(0)}$, it is clear that $(\breve{\mathsf{u}}_\mu^{(0)}|(\mathbb{L}_0 - \lambda_\mu^{(0)})\mathsf{A}) = 0$ for any operator A. Thus, $(\breve{\mathsf{u}}_\mu^{(0)}|$ is orthogonal to the range of $(\mathbb{L}_0 - \lambda_\mu^{(0)})$. Since $(\mathbb{L}_0 - \lambda_\mu^{(0)})$ and $\mathbb{P}_{\mathbb{L}_0-\lambda_\mu^{(0)}}$ share the same range, $(\breve{\mathsf{u}}_\mu^{(0)}|$ is also orthogonal to the range $\mathfrak{R}_\mu$ of $\mathbb{P}_{\mathbb{L}_0-\lambda_\mu^{(0)}}$. Thus, $(\breve{\mathsf{u}}_\mu^{(0)}|$ is an element of the null space $\mathfrak{N}_\mu$ of $\mathbb{P}_{\mathbb{L}_0-\lambda_\mu^{(0)}}$. Assuming that $\lambda_\mu^{(0)}$ is a non-degenerate eigenvalue of $\mathbb{L}_0$, we thus find that $\mathfrak{N}_\mu$ is spanned by $(\breve{\mathsf{u}}_\mu^{(0)}|$, as stated.

A.3. Derivation of steady-state corrections

For the steady state $|\rho_s)$ defined by $\mathbb{L}|\rho_s) = 0$, i.e. $|\rho_s) \equiv |\mathsf{u}_0)$, the recursion relations (4.9) and (4.10) can be simplified significantly. To see this, recall that $\mathbb{L}$ and $\mathbb{L}_0$ are proper generators of the quantum dynamical semigroup (section 3.1). In order to be trace preserving (a necessary condition for a proper generator), the identity operator $\mathsf{1}$ must be the left eigenstate of $\mathbb{L}$ and $\mathbb{L}_0$ with eigenvalue zero, i.e. $(\breve{\mathsf{u}}_0| = (\breve{\mathsf{u}}_0^{(0)}| = \mathsf{1}$. It follows that $\mathsf{1}$ is also the left eigenstate of $\mathbb{L}_1$ with eigenvalue zero since $\mathbb{L}_1 = \mathbb{L} - \mathbb{L}_0$ and thus $\mathrm{Tr}\left[\mathbb{1}\mathbb{L}_1\mathsf{A}\right] = 0$ for any operator A. It is straightforward to show from $\mathrm{Tr}\left[\mathbb{1}\mathbb{L}_1\mathsf{A}\right] = 0$ and eqs. (4.9) and (4.10) that $\forall j \in \mathbb{N}$,

$$\lambda_0^{(j)} = 0, \tag{A.15}$$

$$\left|\rho_s^{(j)}\right) = -\mathbb{L}_0^{\leftarrow 1}\mathbb{L}_1\left|\rho_s^{(j-1)}\right). \tag{A.16}$$

A.4. Series expansion of amplitude matrices

The series expansion of ζ_{s} is valid if all $\zeta_{\mathrm{s}}^{(j)}$ can be determined according to

$$\mathbb{Z}\zeta_{\mathrm{s}}^{(j)} = \rho_s^{(j)} - \sum_{k=1}^{j-1} \zeta_{\mathrm{s}}^{(k)} (\zeta_{\mathrm{s}}^{(j-k)})^\dagger, \tag{A.17}$$

which is eq. (4.19). Here $\mathbb{Z}$ was defined via $\mathbb{Z}\mathsf{A} = \zeta_{\mathrm{s}}^{(0)}\mathsf{A}^\dagger + \mathsf{A}\,(\zeta_{\mathrm{s}}^{(0)})^\dagger$ and $\zeta_{\mathrm{s}}^{(0)}$ is determined through Cholesky decomposition: $\rho_s^{(0)} = \zeta_{\mathrm{s}}^{(0)}(\zeta_{\mathrm{s}}^{(0)})^\dagger$. Equation (A.17) is a system of linear equations and thus has a unique solution if and only if $\mathbb{Z}$ is invertible.

Whether $\mathbb{Z}$ is invertible depends on the form of $\zeta_{\mathrm{s}}^{(0)}$, which in turn depends on the Hermitian and positive-semidefinite $\rho_s^{(0)}$. If one of the eigenvalues of $\rho_s^{(0)}$ is zero, there is a corresponding eigenvector $|\psi\rangle$ such that $\rho_s^{(0)}|\psi\rangle = 0$. Consider the decomposition: $\rho_s^{(0)} = \mathsf{hh}$ where h is a Hermitian matrix. The existence of this decomposition can be simply proven by writing $\rho_s^{(0)}$ in its eigen-decomposition form. Since $|\psi\rangle$ is the eigenvector of $\rho_s^{(0)}$ with eigenvalue zero, $|\psi\rangle$ is also the eigenvector of h with eigenvalue zero, i.e. $\mathsf{h}|\psi\rangle = 0$. Moreover, due to the fact that $\zeta_{\mathrm{s}}^{(0)}(\zeta_{\mathrm{s}}^{(0)})^\dagger = \rho_s^{(0)} = \mathsf{hh}$, $\zeta_{\mathrm{s}}^{(0)}$ and h are unitarily right equivalent [81, p. 348], i.e. $\zeta_{\mathrm{s}}^{(0)} = \mathsf{hS}$ where S is a unitary matrix. Thus, $|\psi\rangle$ is also the left eigenvector of $\zeta_{\mathrm{s}}^{(0)}$ with eigenvalue zero, i.e. $(\zeta_{\mathrm{s}}^{(0)})^\dagger|\psi\rangle = \mathsf{S}^\dagger\mathsf{h}|\psi\rangle = 0$. Now, there must be a right eigenvector of $\zeta_{\mathrm{s}}^{(0)}$, denoted by $|\phi\rangle$, that corresponds to the same eigenvalue (which is zero), i.e. $\zeta_{\mathrm{s}}^{(0)}|\phi\rangle = 0$. We can show by directly substitution that $\mathbb{Z}(\mathsf{T}|\phi\rangle\langle\phi|) = 0$ where T is the matrix corresponding to Gaussian elimination which transforms $(|\phi\rangle\langle\phi|)$ to a lower triangular matrix. Therefore, $\mathbb{Z}$ is not invertible if $\rho_s^{(0)}$ contains at least one eigenvalue zero.

If $\mathbb{Z}$ is not invertible, eq. (A.17) either has infinitely many solutions or no solution. The former case, in which there are infinitely many solutions, can be bypassed if we shift the eigenvalues of $\rho_s^{(0)}$ away from zero. To do so, we consider a shift by an identity-matrix component $\mathbf{1}$ according to

$$\rho_s^{(0)} \to \rho_s^{(0)} + c\mathbf{1}. \tag{A.18}$$

We choose the auxiliary parameter c as close to zero as possible while maintaining numerical stability. In this way, we obtain a procedure to obtain a unique solution to eq. (A.17). This method is similar to the correction matrix method [127, 128] for the Cholesky decomposition of matrices with eigenvalue(s) zero. There, a small diagonal correction matrix is also added to the original matrix to avoid the eigenvalue(s) zero.

If we encounter the case in which there is no solution, we cannot determine $\zeta_{\mathrm{s}}^{(j)}$. In fact, a two-level system coupled to finite temperature bath with $\mathbb{D}\left[\sigma^{+}\right]$ term treated as the perturbation belongs to this case. The failure to determine $\zeta_{\mathrm{s}}^{(j)}$ indicates that the series expansion of ζ_{s} is invalid. This originates from the fact that if $\rho_s^{(0)}$ contains any zero eigenvalues, the leading order term of some elements of ζ_{s} may be of the order of $\alpha^{1/2}$ (or $\alpha^{3/2}$, etc.) instead of α^0. For real functions, an analogy would be the case $y(\alpha) = x^2(\alpha)$ where y can be written as a power series in α. If the leading order term of y is of the order of α, x is a series that only contains half-integer orders of α and thus is not a proper Taylor series. Different expansion types would be needed in this case which we do not discuss further here.

A.5. Detail of resummation

This appendix provides the proof that powers of the $\mathbb{U}$-superoperator can be written as [eq. (4.50)],

$$\mathbb{U}^j = \sum_{k=0}^{j} \varpi_{j-k} \mathbb{T}_k, \tag{A.19}$$

where the prefactor ϖ_{j-k} consists of all possible combinations of $\mathbb{\Sigma}$-superoperators of total order $j-k$. The definitions of the involved $\mathbb{T}$-superoperator and $\mathbb{\Sigma}$-superoperator [eqs. (4.40) and (4.43)] are

$$\mathbb{\Sigma}_1 = 0, \qquad \mathbb{T}_1 = \mathbb{U}, \tag{A.20}$$

$$\mathbb{T}_{j-1}\mathbb{U} = \mathbb{\Sigma}_j + \mathbb{T}_j, \qquad \left(\mathbb{\Sigma}_j\right)_{\mu\nu} = \delta_{\mu\nu} \left(\mathbb{T}_{j-1}\mathbb{U}\right)_{\mu\nu}. \tag{A.21}$$

We further define $\varpi_0 = \mathbb{T}_0 = \mathbb{1}$.

We prove (A.19) by mathematical induction. The $\mathbb{U}^1$ case clearly satisfies (A.19),

$$\mathbb{U}^1 = \mathbb{T}_1 = \mathbb{\Sigma}_1\mathbb{1} + \mathbb{1}\mathbb{T}_1 = \varpi_1\mathbb{T}_0 + \varpi_0\mathbb{T}_1. \tag{A.22}$$

Assume that (A.19) holds up to power $j-1$, i.e.

$$\mathbb{U}^{j-1} = \sum_{k=0}^{j-1} \varpi_k \mathbb{T}_{j-1-k}. \tag{A.23}$$

Then, the decomposition rule (4.45) yields

$$\mathbb{U}^j = \mathbb{U}^{j-1}\mathbb{U} = \sum_{k=0}^{j-1} \varpi_k \mathbb{T}_{j-1-k}\mathbb{U}. \tag{A.24}$$

The product $\mathbb{T}_{j-1-k}\mathbb{U}$ is separated according to eq. (A.21), i.e. $\mathbb{T}_{j-1-k}\mathbb{U} = \mathbb{\Sigma}_{j-k} + \mathbb{T}_{j-k}$, so we obtain

$$\mathbb{U}^j = \sum_{k=0}^{j-1} \mathfrak{o}_k \mathbb{\Sigma}_{j-k} + \sum_{k=0}^{j-1} \mathfrak{o}_k \mathbb{T}_{j-k}. \tag{A.25}$$

The first sum, $\sum_{k=0}^{j-1} \mathfrak{o}_k \mathbb{\Sigma}_{j-k}$, consists of *all* products of $\mathbb{\Sigma}$-superoperators with combined order j, i.e. $\sum_{k=0}^{j-1} \mathfrak{o}_k \mathbb{\Sigma}_{j-k} = \mathfrak{o}_j$. As a result, it follows that

$$\mathbb{U}^j = \mathfrak{o}_j \mathbb{T}_0 + \sum_{k=0}^{j-1} \mathfrak{o}_k \mathbb{T}_{j-k} = \sum_{k=0}^{j} \mathfrak{o}_k \mathbb{T}_{j-k}, \tag{A.26}$$

which concludes the proof.

A.6. Computational cost for perturbative calculations with resummation

The computational cost in calculating perturbative results for the open Jaynes-Cummings lattice primarily stems from summation over matrix elements of the $\mathbb{U}^{\mathbf{kr}}$-superoperator. For each summation, the number of terms is given by N, which corresponds to either the number of qubits or photon modes. The number of necessary summations for rank-j corrections is given by $2j$, see eqs. (4.69) and (4.70). As a result, the overall cost scales algebraically with the number of sites, namely $\sim N^{2j}$. Results for infinite lattices hinge upon the possibility to carry out summations analytically for specific cases, such as for leading-rank corrections of infinite Jaynes-Cummings lattices with periodic-chain or global-coupling geometry.

A.7. Model underlying the ADR estimation

First, consider stochastic switching between two pure states $|1\rangle$ and $|2\rangle$. The simplest description is based on a two-level Hamiltonian $\mathsf{H} = E_{21}\,|2\rangle\,\langle 2|$ where E_{21} is the energy difference between the two states, and the Lindblad master equation

$$\dot{\rho} = -i\,[\mathsf{H}, \rho] + \gamma_{1\to 2}\mathbb{D}\,[|2\rangle\,\langle 1|]\,\rho + \gamma_{2\to 1}\mathbb{D}\,[|1\rangle\,\langle 2|]\,\rho, \tag{A.27}$$

with $\mathbb{D}[\mathsf{A}]$ denoting the usual Lindblad damping superoperator for jump operator A. The resulting 4×4 Liouvillian $\mathbb{L}$ is block-diagonal, where one of the two blocks fully captures the dynamics of density matrices of the form $\rho(t) = p_1(t)|1\rangle\langle 1| + p_2(t)|2\rangle\langle 2|$, where the probabilities $p_{1,2}$ obey the rate equation (6.28). This model can be extended and made more realistic by considering subsets of pure states that make up the two metastable states ρ_1 and ρ_2, which are likely to be mixed states rather than pure states.